



**SELECTED ASPECTS OF THE ARCTIC SEA ICE
MOTION AND ITS INFLUENCE ON THE
OCEAN**

by
Polona Itkin nee Rozman

A thesis submitted in partial fulfillment of the
requirements for the degree of

**Doctor of Philosophy
in Geosciences**

Approved, Thesis Committee

Prof. Dr. Rüdiger Gerdes
Prof. Dr. Laurenz Thomsen
Dr. Martin Losch

Date of Defense: 27th February 2014

School of Engineering and Science

Abstract

A faithful simulation of the sea ice drift in a coupled sea ice-ocean model is one of the key prerequisites for a reliable simulation of the sea ice, ocean and atmosphere interactions. To achieve this goal we should continue improving model physics and constructing parameterizations for relevant sub-grid processes. Also a validation of the simulations against the observational data is essential. The main aim of this work is to demonstrate the importance of the sea ice motion for the underlying ocean. In the scope of the ongoing and anticipated Arctic climate change it has been demonstrated that the changes in the atmosphere and ocean have large impacts on the sea ice cover. At present, it is still unclear if the changes in the sea ice motion itself can also have a feedback effect on the ocean. In this work we hypothesize that a change in the sea ice motion can cause significant changes in the ocean properties and circulation. To test the hypothesis we use two sensitivity studies that help to isolate sea ice motion processes and quantify the contribution of the process to the Arctic climate system. Our main results show that the immobile landfast ice in the model simulation shifts the flaw polynya, location of strong winter sea ice and brine production away from the coast in the more saline ocean waters and more brine reaches the Arctic halocline. This strengthens the halocline that shields cold surface waters and sea ice from the warm Atlantic Water layer underneath. In addition we find that a general change in the sea ice internal strength leads to substantial changes in the ocean properties and circulation. Under weaker and more mobile sea ice Atlantic Water layer temperatures are reduced by 0.2 K. The Eurasian basin circulation in the Atlantic Water layer is increased and this leads to the volume transports adjustments at the Arctic Straits. This effect shows that the Arctic sea ice properties and motion are not only important for the Arctic ocean, but may have consequences also for the global ocean circulation.

Contents

Abstract	i
1 Introduction	1
1.1 Arctic Ocean	1
1.2 Siberian Seas	5
1.3 Scope of this work	8
1.4 Overview of the Papers	13
2 Validating Satellite Derived and Modeled Sea Ice Drift in the Laptev Sea with In-Situ Measurements of Winter 2007/08	19
2.1 Introduction	20
2.2 Observational Data	22
2.3 Model Description	25
2.4 Data Analysis Methods	25
2.5 Observed Sea Ice Drift	28
2.6 Simulated Sea Ice Drift	28
2.7 Drift Vector Validation	35
2.8 Discussion	35
2.9 Conclusions	39
3 Is weaker Arctic sea ice changing the Atlantic water circulation?	41
3.1 Introduction	42
3.2 Model and sensitivity study setup	45
3.3 Comparison to observations	47
3.4 Sea ice and ocean surface	54
3.5 Mid-depth ocean	57
3.6 Connecting the sea ice and mid-depth ocean	63
3.7 Summary and conclusions	66
4 Landfast ice affects the stability of the Arctic halocline: evidence from a numerical model	69
4.1 Introduction	70
4.2 Model setup	73
4.2.1 Landfast ice Parameterization	74
4.3 Impact of the landfast parameterization on the sea ice	76
4.4 Impact of the landfast parameterization on the Arctic halocline	79

4.5	Discussion	82
4.6	Summary and conclusions	88
5	Summary and Concluding Remarks	89
5.1	Outlook	90
	Bibliography	93
	Acknowledgements	109

List of Figures

1.1	The Arctic Ocean and its marginal seas	2
1.2	Arctic Oscillation	3
1.3	Arctic ocean vertical stratification	4
1.4	Siberian Seas	6
1.5	Photos of leveled landfast ice and polynya in the Chukchi Sea . .	7
1.6	Model domain of NAOSIM and MITgcm and the bathymetry of the MITgcm.	12
1.7	Schematic view of two vertical coordinate options under thick sea ice	14
1.8	Mooring scheme	15
2.1	Laptev Sea bathymetry and ASAR satellite image	21
2.2	Scatter plots of sea ice drift speed and direction at the Anabar and Khatanga mooring locations	29
2.3	Scatter plots of sea ice drift speed and direction in the outer shelf	30
2.4	Simulated sea ice drift speed and direction without and with integrated fast ice at Khatanga mooring	31
2.5	Simulated sea ice drift speed and direction without and with integrated fast ice in the outer shelf	32
2.6	Scatter plots of sea ice drift speed and direction at the Anabar and Khatanga mooring locations	33
2.7	Scatter plots of sea ice drift speed and direction at in the outer shelf	34
3.1	The model domain and bathymetry	43
3.2	Sea ice concentration observations and the differences to the model	49
3.3	Sea ice thickness observations and the differences to the model .	50
3.4	Histograms sea ice drift speed	52
3.5	Vertical mean annual temperature at the Kola section	53
3.6	Sea ice and ocean surface properties, part 1	55
3.7	Sea ice and ocean surface properties, part 2	56
3.8	Temperature and velocity means in the AWL	58
3.9	Development of the AWL temperature differences, part 1	59
3.10	Development of the AWL temperature differences, part 2	60
3.11	Mean temperature sections at St. Anna Trough and Fram Strait	61
3.12	Time series of the net volume fluxes at the major Arctic Straits .	62

3.13	Time series of the annual mean sea ice and ocean variables for the Barents Sea	64
4.1	The Arctic Ocean and its marginal seas	71
4.2	Arctic Ocean vertical stratification and winter processes maintaining the Arctic halocline.	73
4.3	The effect of the landfast ice parametrization on the sea ice . . .	76
4.4	Mean winter sea ice thickness, thermodynamical growth and salt flux	78
4.5	Mean winter sea ice time series for the Laptev Sea and East Siberian Sea	80
4.6	Mean April buoyancy at the top halocline	81
4.7	Mean April (2000-2010) salinity, temperature, river water fraction and buoyancy frequency along the section across the Canadian Basin.	83
4.8	Hovmöller diagrams of monthly mean salinity and river water fraction	84
4.9	Mean April (2000-2010) salinity, temperature, river water fraction and buoyancy frequency along the section across the Makarov Basin	85
4.10	Mean April (2000-2010) salinity, temperature, river water fraction and buoyancy frequency along the section across the Eurasian Basin.	86

List of Tables

- 2.1 The overview of the datasets used in the validation 24
- 2.2 The validation results of the drift vector components of the satellite products and model simulations with the in-situ measurements for the Laptev Sea mid-shelf in winter 2007/2008 35

List of Acronyms

ADCP	Acoustic Doppler Current Profiler
AIW	Arctic Intermediate Water
AIW	Arctic Intermediate Water
AMOC	Atlantic Meridional Overturning Circulation
AMSR-E	Advanced Microwave Scanning Radiometer
AO	Arctic Oscillation
AOMIP	Arctic Ocean Model Intercomparison Project
ARP	Arctic Rapid change Pattern
ASAR	Advanced Synthetic Aperture Radar
AW	Atlantic Water
AWI	Alfred Wegener Institute
AWL	Atlantic Water Layer
Barents Sea Branch)
BG	Beaufort Gyre
CERSAT	Center for Satellite Exploitation and Research
CMCC	Continuous Cross Correlation Method
CORE	Coordinated Ocean Research Experiment
CTRL	control run
FSB	Fram Strait Branch
ICESat	Ice, Cloud, and land Elevation Satellite
IFREMER	French Research Institute for Exploitation of the Sea
LF	landfast ice run
MITgcm	Massachusetts Institute of Technology General Circulation Model

MIZ Marginal Ice Zone
MODIS Moderate Resolution Imaging Spectroradiometer
NAOSIM North Atlantic/Arctic Ocean - Sea Ice Model
NCAR/NCEP National Centers for Environmental Prediction/National Center
for Atmospheric Research
NSIDC National Snow and Ice Data Center
OSI-SAF EUMETSAT Ocean and Sea Ice Satellite Application Facility
P compressive sea ice strength
P* maximal compressive sea ice strength empirical constant
PIOMAS Pan-Arctic Ice-Ocean Modeling and Assimilation System
QuikSCAT Quick Scatterometer
SLP Sea Level Pressure
SSM/I Special Sensor Microwave/Imager
SST Sea Surface Temperature
T sea ice tensile strength
TD Transpolar Drift
WEAK weak sea ice run
WSC West Spitzbergen Current
z* rescaled vertical coordinate

Chapter 1

Introduction

This thesis is organized in the following way: in this Chapter Sections 1.1 and 1.2 give a brief introduction of the investigated research area, Section 1.3 outlines the aims and research hypothesis, Section 1.3 describes the applied methods, Section 1.4 introduces the papers that form the core of the thesis in Chapters 2, 3 and 4. Finally, Chapter 5 gives a summary of the findings.

1.1 Arctic Ocean

The Arctic Ocean or the Arctic Mediterranean is the world smallest ocean. On the southern rims it is connected to the Atlantic Ocean through the Fram Strait and through the Canadian Archipelago and to the Pacific Ocean through the Bering Strait. The Arctic Ocean has a perennial sea ice cover that reaches its maximal extent in winter when it covers most of the ocean's surface and its minimal extent in summer when the sea ice cover is confined only to the deep basins. Although the Arctic Ocean takes less than 4 % of the global ocean surface it gathers more than 10 % of the global continental river runoff (de Couet and Maurer, 2009).

The Arctic Ocean sea ice and ocean surface circulation is characterized by the anticyclonic Beaufort Gyre (BG) in the Amerasian Basin and the Transpolar Drift (TD) that carries the sea ice and surface water from the Siberian Seas towards Fram Strait (light blue arrows on Figure 1.1). The interannual variability in the strength and location of the ocean surface current system components depends on the Sea Level Pressure (SLP) over the Amerasian Basin and North Atlantic (Govorucha and Gerasimov, 1970; Proshutinsky and Johnson, 1997;

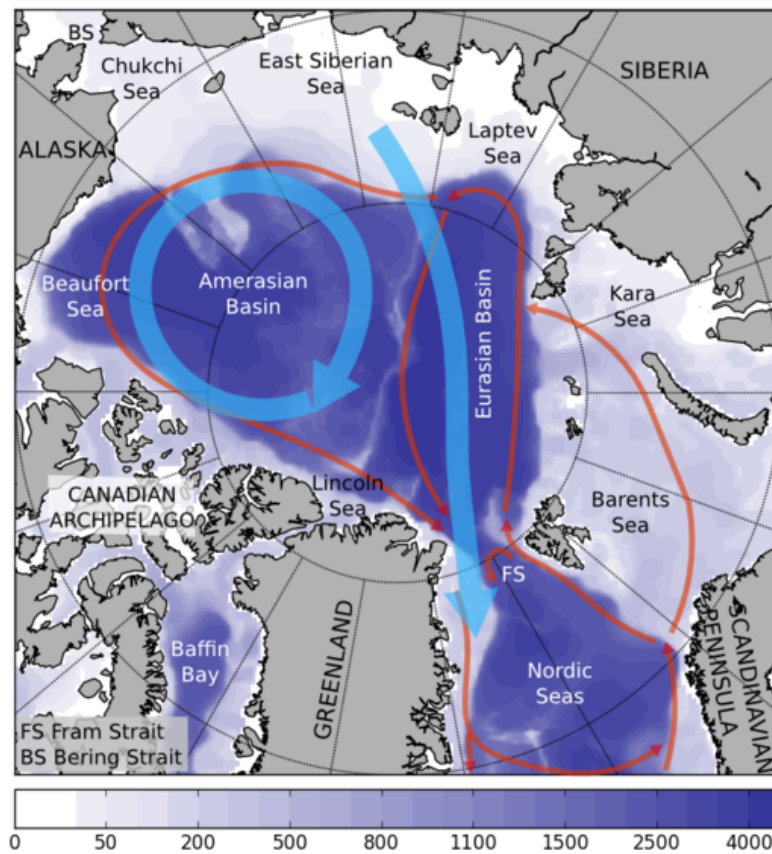


Figure 1.1

Figure 1.1: The Arctic Ocean and its marginal seas. The sea ice and surface circulation is schematically represented by light blue and mid-depth circulation by red arrows (simplified from Rudels et al (1994)).

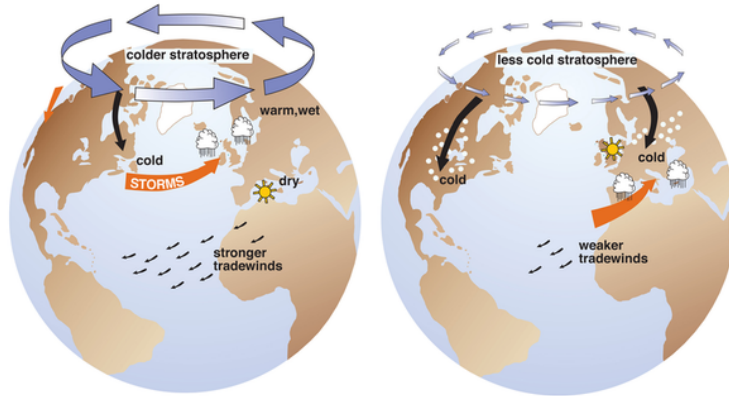


Figure 1.2: Arctic Ocean Oscillation: positive phase with a strong Arctic high (left) and negative phase with the weak Arctic high. Credit: J. Wallace, University of Washington.

Johnson et al, 1999). If the Icelandic Low expands further from the North Atlantic to the Barents and Kara seas, the anticyclonic circulation is weak and the TD widens and slows down. If the anticyclonic circulation over the Amerasian basin is strong, the TD is positioned closer to the Siberian shelfbreak and faster. The corresponding atmospheric circulation anomaly was characterized by Thompson and Wallace (1998) as the Arctic Oscillation (AO). The AO index is defined as the leading principal component of Northern Hemisphere SLP. A strong positive AO index from 1989 till 1995 with weaker Polar High over the Amerasian Basin and therefore weaker anticyclonic circulation and stronger westerlies in the subpolar latitudes was interpreted as the main cause for the steady decrease of the Arctic sea ice extent and sea ice thinning in the 1990s (Rigor et al, 2002). In addition to the local SLP changes in the Arctic, during the AO positive phase the stronger westerlies bring more warmth and moisture to Eurasian catchment areas and increase the continental runoff of the Arctic rivers that also influence the Arctic Ocean surface hydrography.

Since 1995 the AO has been predominantly near-neutral or negative, but the sea ice extent and thickness were still decreasing (Comiso et al, 2008; Haas et al, 2008; Kwok et al, 2009). This Arctic Paradox (Overland and Wang, 2005) was addressed by Zhang et al (2008) who pointed out another pattern in the atmospheric circulation, the third principal component of the Northern Hemisphere SLP: a dipole structure between the Eurasian Arctic coast and North Pacific named Arctic Rapid change Pattern (ARP). In recent years the ARP replaced the AO as the leading SPL pattern. The ARP is associated with the polar-ward winds that transfer more heat from subpolar latitudes into the

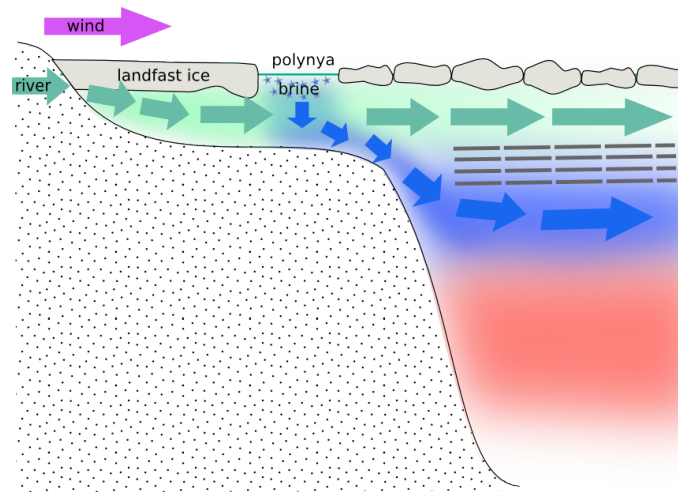


Figure 1.3: Arctic ocean vertical stratification and winter processes maintaining the Arctic halocline.

Arctic (Overland and Wang, 2010). The anomalous Eurasian Arctic coast high and North Pacific low occur during the ARP's negative phase, which strengthen meridional atmospheric heat transport and enhance Atlantic Water (AW) inflow into the Arctic Ocean (Zhang et al, 2008).

In the Arctic Ocean surface layer that is driven by these atmospheric circulation patterns the seasonal sea ice melt and freezing cycle maintains the fresh upper ocean waters at the freezing point. In contrast, the ocean temperature below the halocline (Figure 1.3) increases again and at mid-depth the Arctic Ocean has temperatures up to several degrees above zero. The bulk of this warm and salty water is composed of Atlantic Water (AW) that enters the Arctic Ocean through the Fram Strait and the Barents Sea. Also the anticyclonic surface circulation is contrasting the mid depth circulation of the Atlantic Water Layer (AWL) characterized by generally cyclonic motion, most of which occurs in boundary currents along the deep ridges and shelf breaks (red arrows on Figure 1.1, Rudels et al (1994)). Before entering the central Arctic Ocean basins via Fram Strait or the Barents Sea both AW branches experience heat loss and are modified by ice melt and freeze, as well as river runoff. Both branches feed the AWL and after passing through the basins leave the Arctic ocean proper on return through the Fram Strait as Arctic Intermediate Water (AIW). The AIW flows into the Nordic Seas and has an important role in the dense water formation that feed the Atlantic Meridional Overturning Circulation (AMOC) (Schmitz and McCartney, 1993; Swift, 1984).

The cold and fresh surface layers are decoupled from the mid-depth salty and

warm AWL by a strong halocline (Figure 1.3) which is maintained by the cold brines formed on the shelf seas (Aagaard et al, 1981; Martin and Cavalieri, 1989; Cavalieri and Martin, 1994a; Winsor and Björk, 2000) and by winter convection in the northern Barents Sea (Rudels et al, 1996). The cold and fresh waters flow off the shelves and sink along the shelf break, where they mix with the adjacent warm AW. Several authors report about the temperature fluctuations of the AW in the 20th century (Schauer et al, 2004; Polyakov et al, 2005a; Dmitrenko et al, 2008a). If the warming signal detected in the last decade would continue (Dmitrenko et al, 2008a) this could weaken the halocline and some heat could reach the surface layer and contribute to further fast reductions of the Arctic sea ice cover. Also an eastward redirection of the riverine water would result in the surface layer salinification in the Eurasian Basin and halocline weakening as already observed by Johnson and Polyakov (2001) during the positive AO phase in the 1990s. The mid-depth and to some extent also deep water mass modifications detected in the Arctic Ocean in the last decade can exit through the Fram Strait and the Nordic Seas, reach the deep convection areas in the North Atlantic (Karcher et al, 2011) and influence the AMOC.

The combination of the ongoing changes in atmospheric conditions, drifting and landfast ice, and continental runoff are driving the changes in the Arctic Ocean sea ice cover. The Arctic sea ice is getting thinner (Kwok and Rothrock, 2009), more mobile (Rampal et al, 2009; Spreen et al, 2011) and the sea ice extent is shrinking (Stroeve et al, 2012). The reasons for the changes have been under vigorous inspection in the scientific community in various observational and modeling studies (Shimada et al, 2006; Perovich et al, 2008; Kauker et al, 2009; Polyakov et al, 2010; Kattsov et al, 2010; Zhang et al, 2012).

1.2 Siberian Seas

The Eurasian shelf with its shallow seas is the largest shelf in the world and it occupies about 1/3 of the Arctic Ocean area. The eastern part of it, the Siberian shelf which is commonly divided into Kara, Laptev East Siberian and Chukchi Sea, is the shallowest (depth rarely exceeding 200 m) and freshest part of it, as it receives water from the great Siberian rivers: Ob, Yenisei and Lena. Together with smaller rivers they contribute approximately 2100 km³/year of freshwater (Prange, 2003). This large inflow of river water strongly affects temperature, salinity and other ocean parameters. Peterson et al (2002) analyzed the average annual discharge from the six largest Eurasian rivers and

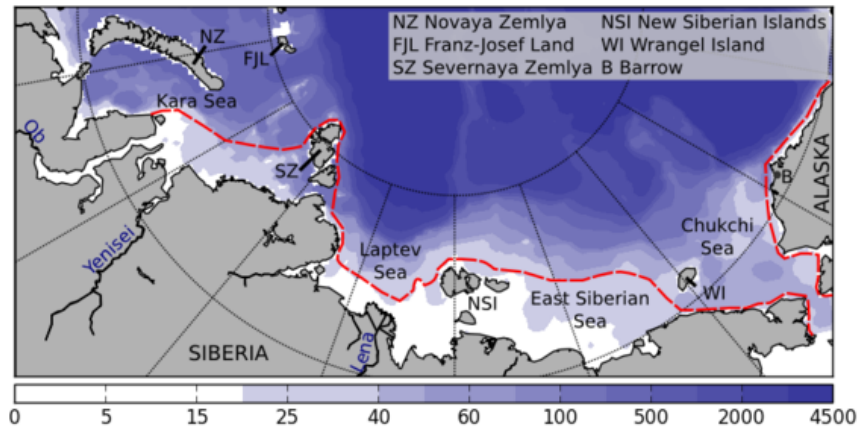


Figure 1.4: Siberian Seas and average position of the landfast ice edge (red dash line).

discovered an increase of 7% from 1936 to 1999. This agrees with the steady increase in the northern Eurasian precipitation over the 20th century (Kattsov and Walsh, 2000; McClelland et al, 2004).

Landfast ice (also fast, shore-fast ice) is a dominating feature in the Siberian Seas during winter as it can extend a few kilometers from the coast in the western part of the Laptev Sea or in the Chukchi Sea to several hundred kilometers in the southeastern Kara, Laptev and East Siberian Seas. This creates a vast hydrologically distinct inner shelf region outlined by the landfast ice edge and decoupled from the atmosphere with sea ice that is immobile and mechanically fastened to the coast or to the sea floor. Landfast ice consolidates in late November and remains fixed until early July break up (Rigor and Colony, 1997). For drifting sea ice, the landfast ice edge forms an advanced winter shore line and heavy ridging occurs along this edge during onshore wind events. During the prevailing offshore winds pack ice is advected seaward from the landfast ice edge and narrow stretches of open water and young ice - flaw polynyas, occur. Frequent polynya events, low winter temperatures and prevailing northward ice drift make the Siberian flaw polynya system a major source of the sea ice production for the TD (Eicken et al, 1997; Rigor and Colony, 1997; Alexandrov et al, 2000). The possible contribution of the Siberian flaw polynyas to the formation of dense saline shelf waters was addressed by Aagaard et al (1981); Martin and Cavalieri (1989); Cavalieri and Martin (1994b); Winsor and Björk (2000); Dmitrenko et al (2005b); Bauch et al (2009); Krumpen et al (2011). The role of this immobile ice cover for the riverine water redistribution was summed up by Proshutinsky et al (2007).



Figure 1.5: Left: Photo of leveled landfast ice, right: polynya in the Chukchi Sea during SIZONet sea ice campaign at Barrow, Alaska, May 2010.

The knowledge about the general circulation patterns in the Siberian Seas is based on the Russian historical datasets from predominantly summer expeditions. Its main characteristic is the eastward alongshore Siberian Coastal Current that is forced by winds, river runoff and ice melt (Govorucha and Gerasimov, 1970; Weingartner et al, 1999). The current direction is variable and it can revert westward (Münchow et al, 1999). Just north of the shelf break the much better studied TD system begins.

Local atmospheric circulation over the Siberian Seas is governed by the large scale atmospheric circulation over the Arctic Ocean. The Laptev Sea, in particular, is situated within the zero vorticity contour separating the SLP centers over the Amerasian Basin and North Atlantic (Johnson and Polyakov, 2001). This position renders its hydrography very sensitive to the shifts between predominant cyclonic and anticyclonic atmospheric circulation (Dmitrenko et al, 2005a) and several authors distinguish between periods with predominant cyclonic and predominant anticyclonic regimes (Dmitrenko et al, 2005a; Bauch et al, 2009; Abrahamsen et al, 2009). The winds are parallel to the isobars and the Coriolis force deflects the ocean and sea ice motion on the Northern hemisphere to the right. The mean surface current direction is usually perpendicular to the wind direction. On the shallow shelf, however, the current is essentially controlled by wind stress and bottom friction and the Coriolis force becomes insignificant. The surface current aligns almost completely with the wind direction. Thus, the cyclonic regime on the Laptev Sea shelf drives "onshore" surface currents that divert the riverine water eastward towards the East Siberian Sea. In the "offshore" anticyclonic regime the riverine water is advected northward.

The declining summer sea ice cover is opening large areas of open water in the

Siberian Seas (Comiso et al, 2008; Stroeve et al, 2012). The modified surface fluxes should lead to warmer and fresher surface layer. Analysis of the historical datasets show that during the negative AO phase from 1930-1965 the Siberian Seas surface waters have been cooled with a trend of over 0.5°C per decade while in turn in the 1965-1995 positive AO phase the trend has been similar, but opposite in sign (Steele et al, 2008). Timokhov and Tanis (1997, 1998) show decadal scale changes in the surface water temperatures of a degree or more. Dmitrenko et al (2010), however analyzed the historical dataset with addition of the data from Russian-German expeditions in the 1990s and 2000s and report no significant warming over the Laptev Sea shelf deeper than 10-15 m. In summer 2007, when a prominent minimum in sea ice extent was observed, the atmospheric circulation over the Siberian Seas was cyclonic (Abrahamsen et al (2009); Hölemann et al (2011) -"onshore"). Most of the seas were ice free and absorbed unusual amount of heat. Steele et al (2008) and Frolov et al (2009) report a $+2^{\circ}\text{C}$ to $+5^{\circ}\text{C}$ anomaly in the sea surface temperature (SST). The bottom water temperatures anomaly on the mid-shelf was more than $+3^{\circ}\text{C}$ (Hölemann et al, 2011). The possible reduction of landfast ice cover extent or duration in the future would result in flaw polynyas located in the fresher coastal waters and less brine would reach the Arctic halocline. The modifications of the shelf water masses that feed the Arctic Ocean surface and partly intermediate layers might lead to changes in the Arctic Ocean stratification (Figure 1.3).

1.3 Scope of this work

The main aim of this work is to demonstrate the importance of the sea ice motion for the underlying ocean. Sea ice motion is transporting sea ice from the area where the sea ice formed through the freezing processes to the area where it melts and releases freshwater and takes up latent heat from the ocean and atmosphere. The sea ice drift, and in particular the divergent sea ice motion causes opening of leads and polynyas, where more sea ice is formed and the ocean's freshwater is removed, stored in solid form in the sea ice and latent heat is released to the atmosphere. The remaining surface ocean water depleted in freshwater still contains the salt and thus has a higher density than the underlying water and therefore sinks to the depth where its buoyancy is neutral.

The sea ice is also a layer between the atmosphere and ocean and is transmitting and transforming the wind stress to the ocean surface. How much momentum

is transferred from the atmosphere to the ocean depends on the sea ice internal stress. The main tool for our investigations is a numerical sea ice-ocean coupled model described in Section 1.3 where processes outlined above are represented by equations.

A faithful simulation of the sea ice drift in a coupled sea ice-ocean model is one of the key prerequisites for a reliable simulation of the sea ice, ocean and atmosphere interactions. Apart from improving model physics and constructing parameterizations for relevant sub-grid processes also validation of the simulations against the observational data is essential. But the Arctic Ocean is a remote region, generally inaccessible during the severe winter weather conditions. Satellite remote sensing products (Ezraty et al, 2006; Lavergne et al, 2010) offer a large improvement in the spatial and temporal availability of observational ice drift data, but they also need to be validated with the in-situ data. For the remote coastal regions such as the Siberian Seas there are even fewer ice drift field observations available, as the manned stations and drifting buoys are usually positioned in the thicker sea ice of the Central Arctic. Alternatively a numerical model simulation offers a temporally and spatially holistic view on the processes in the Arctic Ocean. At this point the model simulations, satellite and in-situ observations should be seen as complimentary research approaches that benefit from each other and not as alternatives.

In the scope of the ongoing and anticipated Arctic climate change (Kwok and Rothrock, 2009; Spreen et al, 2011; Stroeve et al, 2012) it has been demonstrated that the changes in the atmosphere (Shimada et al, 2006; Perovich et al, 2008) and ocean (Polyakov et al, 2010) have a large impact on the sea ice cover. It has also been shown that the thinning of the sea ice is preconditioning further fast reductions in the sea ice (Haas et al, 2008; Zhang et al, 2012). The hypothesis of the sea ice positive feedback where the loss of the Arctic sea ice will lead to albedo increase and consequently to even faster warming of the Arctic has been widely accepted by the scientific community. At present, it is still unclear if the changes in the sea ice motion itself can also have a feedback effect on the ocean. In this work we hypothesize that a change in the sea ice motion will cause significant changes in the ocean properties and circulation. To test the hypothesis we use two sensitivity studies that help to isolate sea ice motion processes and quantify the contribution of the process to the Arctic climate system.

Data and Methods

The main tool for our investigations is a numerical sea ice-ocean coupled model. State-of-the-art sea ice models are all based on the same set of primitive equations that are simplified descriptions of the processes in nature. The sea ice is usually simulated by a dynamical-thermodynamical models such as Hibler (1979) or Hunke and Dukowicz (1997). The base of the thermodynamical model is the energy balance of the sea ice:

$$Q_a + Q_w + \rho_i L_i \frac{\partial h}{\partial t} = 0 \quad (1.1)$$

where Q_a is the heat exchange of the sea ice with the atmosphere and Q_w with the ocean. ρ_i is the sea ice density. L_i is the latent heat taken up or released during sea ice growth: $\frac{\partial h}{\partial t} > 0$ or sea ice melt: $\frac{\partial h}{\partial t} < 0$, where h is sea ice thickness and t is time.

The base of the sea ice dynamical model is the momentum balance (Hibler, 1979):

$$m_i \left(\frac{\partial \vec{u}}{\partial t} + \vec{u} \cdot \nabla \vec{u} \right) = \tau_a + \tau_w - m_i f \vec{k} \times \vec{u} - m_i g \nabla H_{tilt} + \nabla \cdot \sigma \quad (1.2)$$

where m_i is the sea ice mass per unit area and \vec{u} is the sea ice velocity. On the right-hand side of the equation the terms are τ_a - atmospheric stress, τ_w - oceanic stress, $m_i f \vec{k} \times \vec{u}$ - Coriolis term (f is the Coriolis parameter and \vec{k} is the unit vector normal to the surface), $m_i g \nabla H_{tilt}$ - horizontal tilt term (g is gravitational acceleration and H_{tilt} is the sea surface tilt) and finally the divergence of the ice stress tensor $\nabla \cdot \sigma$ that describes the internal sea ice forces stemming from ice interactions like rafting, ridging and fracturing. This is the only term in the equation which depends directly on the sea ice properties itself.

Hibler (1979) uses a rheology that connects σ with the strain rate tensor $\dot{\epsilon}$, a basic variable describing the sea ice behavior, and considers the sea ice as a viscous plastic fluid. This means that at small σ and $\dot{\epsilon}$ acting upon sea ice, sea ice behaves like a viscous fluid and undergoes no deformation. But when a certain threshold is reached sea ice behaves like a plastic material and is permanently deformed. σ is defined as:

$$\sigma_{ij} = 2\eta\dot{\epsilon}_{ij} + ((\eta - \zeta)(\dot{\epsilon}_{11} + \dot{\epsilon}_{22}) - \frac{P}{2})\delta_{ij}, \quad (1.3)$$

where σ_{ij} and $\dot{\epsilon}_{ij}$ are two-dimensional stress and strain rate tensors and δ_{ij} is the Kroeneker delta function. ζ - bulk viscosity, η - shear viscosity and P - maximal compressive sea ice strength are defined as:

$$\zeta = P/2\Delta, \quad (1.4)$$

$$\eta = \zeta/e^2, \quad (1.5)$$

and

$$P = P^*h \exp(-C^*(1 - A)), \quad (1.6)$$

where $\Delta = \sqrt{(\dot{\epsilon}_{11}^2 + \dot{\epsilon}_{22}^2)(1 + e^{-2}) + \frac{4}{e^2}\dot{\epsilon}_{12}^2 + 2\dot{\epsilon}_{11}\dot{\epsilon}_{22}(1 - e^{-2})}$ is a term introduced for brevity and e is the eccentricity constant. The maximal compressive sea ice strength P in this rheology varies with the sea ice thickness and concentration (A), whereas P^* and C^* - sea ice strength parameters are empirical constants.

To track the consequences of the perturbing the sea ice motion the sea ice model is coupled to a regional ocean model. In this study we use two models: The North Atlantic/Arctic Ocean - Sea Ice Model (NAOSIM) and the Massachusetts Institute of Technology general circulation model (MITgcm). Both models cover the same domain enclosing the northern North Atlantic, the Nordic Seas and the Arctic Ocean (Figure 1.6) on a rotated grid with the grid equator passing through the geographical North Pole. Both models have similar numerics, but differ in the spatial resolution.

NAOSIM is a coupled ocean-sea ice model developed at the AWI (Gerdes et al, 2003; Karcher et al, 2003; Fieg et al, 2010). Here we use the highest resolving version of NAOSIM (Fine Resolution Model), that has a horizontal grid spacing of $1/12^\circ$. In the vertical, the model has 60 levels. Near the surface, the vertical resolution is 10 m. There is a minimum number of three grid cells in the vertical, limiting the representation of shallow topography. The ocean component of the model is based on the Modular Ocean Model MOM-2 of the Geophysical Fluid Dynamics Laboratory (Pacanowski, 1995). It is coupled, following the scheme developed by Hibler and Bryan (1987), to a dynamic-thermodynamic sea ice model (Hibler, 1979) which employs a viscous-plastic rheology. River water discharge is incorporated as in Prange and Gerdes (2006). River water influx is

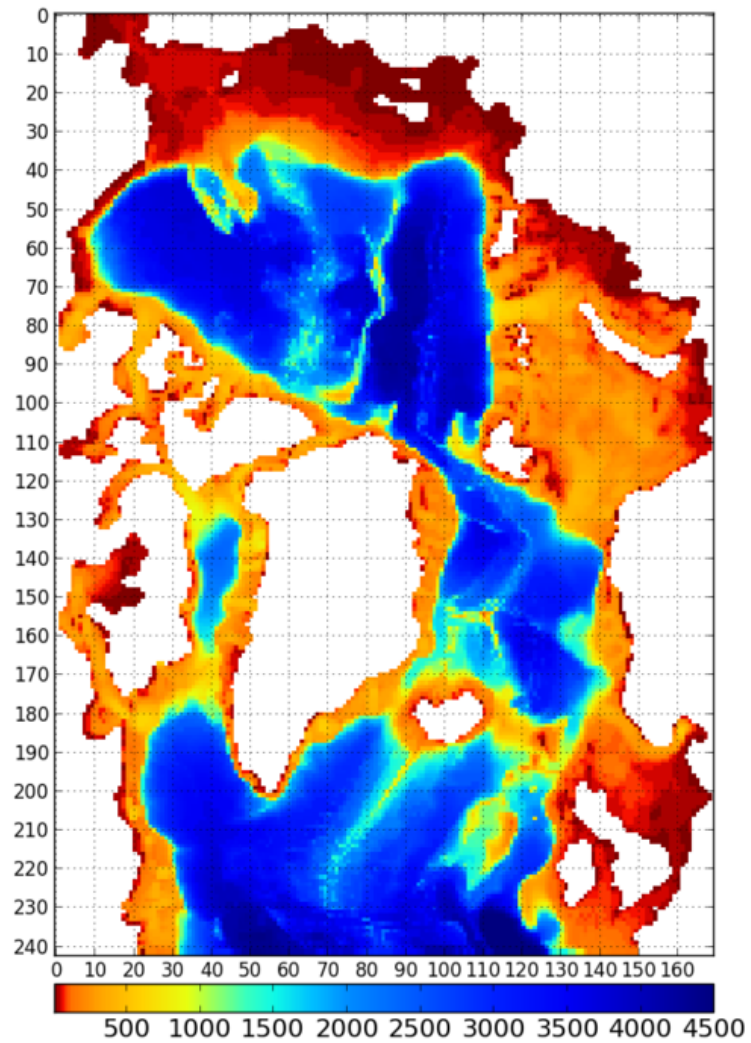


Figure 1.6: Model domain of NAOSIM and MITgcm and the bathymetry of the MITgcm.

distributed over the first three levels in the vertical to improve vertical mixing of the fresh water near the river mouths (Fieg et al, 2010). The model includes a passive salinity tracer to follow the spreading of the river water. NAOSIM is an established model in the Arctic community participating in the Arctic Ocean Model Intercomparison Project (AOMIP, <http://www.whoi.edu/projects/AOMIP/>).

Massachusetts Institute of Technology General Circulation Model - MITgcm (Marshall et al, 1997) is a community effort model available at <http://mitgcm.org/>. The numerous users of the code update, develop, maintain and document the model code on a regular basis. The model configuration we have used is similar to the NAOSIM, but it has a coarser horizontal resolution of $1/4^\circ$ (~ 28 km). The vertical resolution is adjusted to the surface and halocline studies and its 36 levels are unevenly distributed in a way that the top 500 m of the water column is divided into 20 levels and the depths below 2000 m have only 6. The very thin surface layer thickness under sea ice requires a non-linear free surface and the use of the rescaled vertical coordinate z^* (Figure 1.7, (Campin et al, 2008)). Non-linear free surface and z^* are an example of options that are not available at NAOSIM. The MITgcm sea ice model is based on a version of the viscous-plastic dynamic-thermodynamic sea ice model of Zhang and Hibler III (1997) with some adaptations and many further numerical options and parameterizations described by Losch et al (2010).

To validate our sea ice drift simulation in the Laptev Sea we have used a unique mooring (Figure 1.8) dataset from winter 2007/08 and a self produced sea motion product. Other data used for the validation in our research are publically available remote sensing sea ice products and sea ice and ocean databases.

1.4 Overview of the Papers

The main aim of this thesis is to investigate the effect of the sea ice motion on the underlying ocean.

In the first paper:

Polona Rozman¹, Jens Hölemann, Thomas Krumpen, Rüdiger Gerdes, Cornelia Köberle, Thomas Lavergne, Susanne Adams and Fanny Girard-Arduin, 2011: **Validating Satellite Derived and Modeled Sea Ice Drift in the Laptev Sea with In-Situ Measurements of Winter 2007/08**. Polar Re-

¹This paper has been published under Polona Itkin's maiden name Rozman.

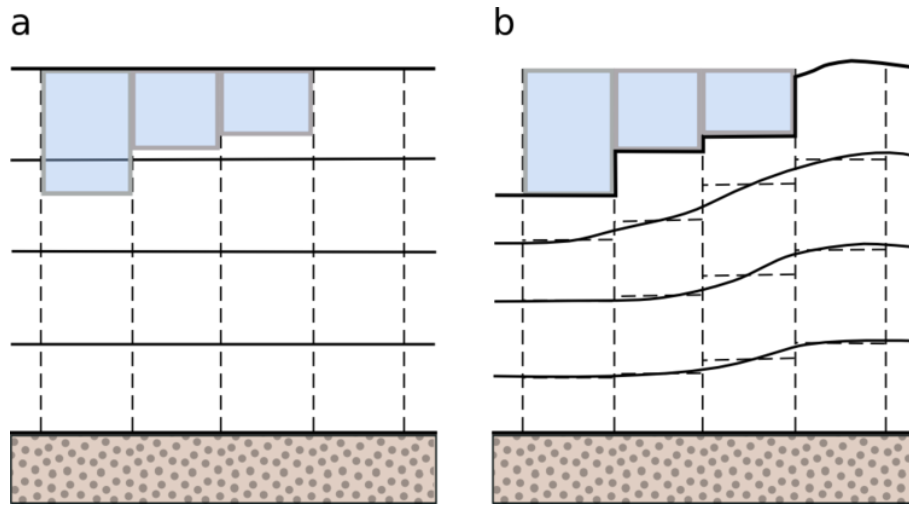


Figure 1.7: Schematic view of two vertical coordinate options under thick sea ice: a - z vertical coordinate with rigid lid, b - z^* vertical coordinate with non-linear free surface. In a the first layer is a mixture of sea ice and water with the first level empty, while in b the sea surface position is depressed by the weight of sea ice and the scaling of the coordinate to avoid the problem of disappearing level. The figure is adopted from Campin et al (2008).

search, 30, 7218, DOI: 10.3402/polar.v30i0.7218.

we address the challenge of cross-validating the point observations, remote sensing products and model simulations. Our research area is the Southeastern Laptev Sea, a coastal region that is especially difficult to simulate due to the partial cover with the immobile landfast sea ice. The land contamination of the satellite sea ice grid points close to the coast and a general lack of the in-situ data make this validation attempt especially difficult. To address the latter problem we present a unique dataset composed of two points with mooring measurements over the winter 2007/08. We use an approach novel in the sea ice research: circular statistics to compare the sea ice drift directions.

Our main findings are that correlations of sea ice direction between the in situ data and the remote sensing products are high, about 0.8. Similar correlations are achieved by the model simulations. The sea-ice drift speed is the more challenging variable as some of the satellite products and model have only moderate correlations of about 0.6 to the in situ records. The landfast ice parameterization implementation in the model was successfully tested for its influence on the sea-ice drift. In contrast to the satellite products, the model drift simulations have a full temporal and spatial coverage and results are reliable enough to be used as sea-ice drift estimates on the Laptev Sea Shelf.

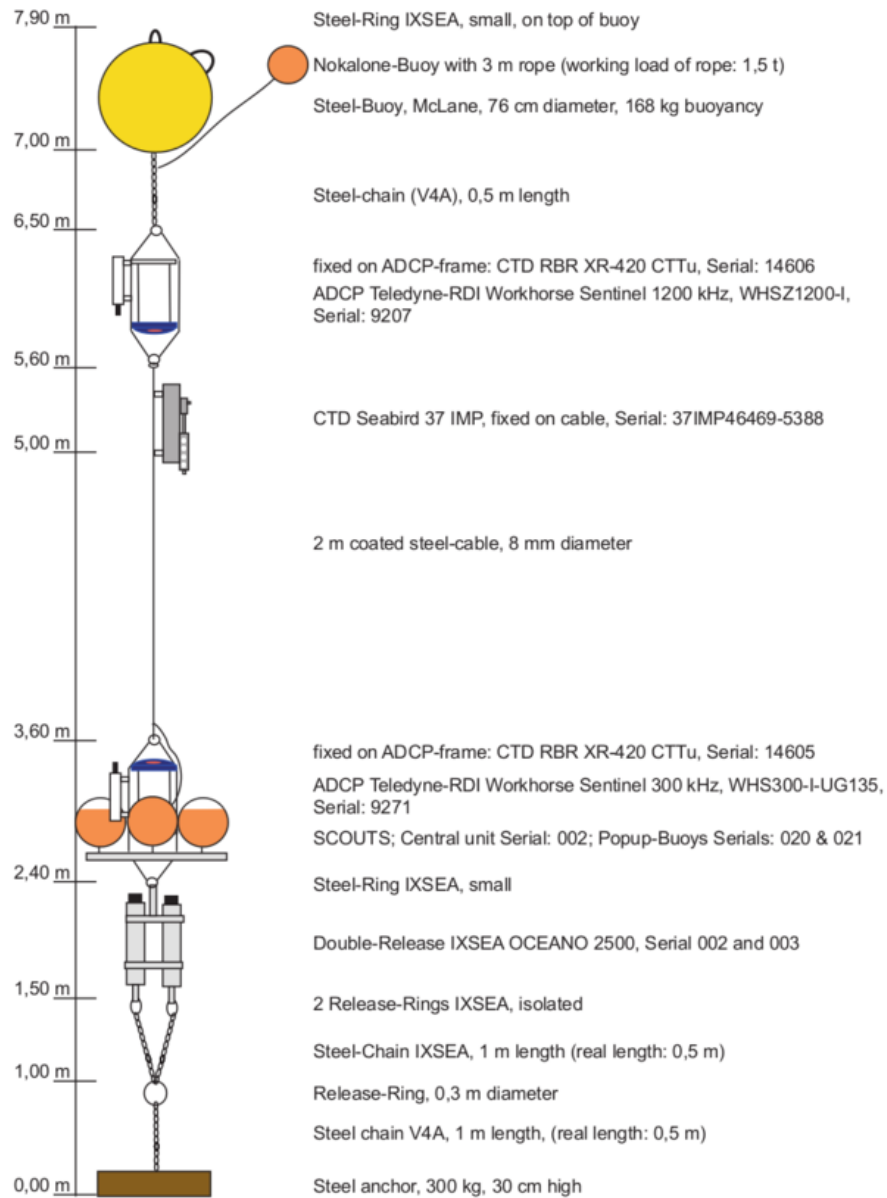


Figure 1.8: Mooring scheme of the two moorings which data forms the dataset. The instrument monitoring the sea ice drift is the ADCP (Acoustic Doppler Current Profiler) at 3 m above the bottom. Credit: Torben Klagge, IFM-Geomar, Kiel.

As our main aim remains to study the impact of the sea ice motion on the ocean we then attempted to develop a landfast ice parameterization that would be applicable for more than a single winter and dependent as well on the sea ice properties. Landfast ice is immobile level sea ice (Figure 1.5) and the most logical property to use was the compressive sea ice strength (P) that prevents the sea ice from deforming. To inspect a general impact of P on the sea ice and ocean we performed a sensitivity study that was motivated also by the observed changes of sea ice motion due to the climate change.

Our second paper is therefore:

Polona Itkin, Michael Karcher and Rüdiger Gerdes, 2014: **Is weaker Arctic sea ice changing the Atlantic water circulation?** In press for the Journal of Geophysical Research - Oceans.

In this paper we perform a sensitivity study by comparing two MITgcm model simulations that differ only in the P^* constant: 25700 N/m^2 (control run: CTRL) and 15000 N/m^2 (weak sea ice run: WEAK). In WEAK the sea ice velocities are generally higher than in CTRL. Through the momentum transfer to the ocean and difference in the sea ice cover distribution these differences are reflected not only in the surface layer, but also in the mid-depth AWL of the ocean. Differences in the sea ice extent in the marginal sea ice zone (MIZ) lead to a reduction of the AWL temperatures by 0.2 K in WEAK comparing to CTRL. The increased sea ice mobility in the central Arctic in WEAK results in faster and deeper ocean's anticyclonic BG which hampers the cyclonic AW circulation beyond the Lomonosov Ridge and enhances the loop of the AW in the Eurasian Basin. As a result of both mechanisms, the Fram Strait net outflow increases by 0.46 Sv whereas as a reaction the Davis Strait net outflow is weaker by 0.28 Sv .

The main lesson that we learn with this study for our landfast ice parameterization development is that the P^* parameter choosing (and P definition) should be done with care and that a uniform change of P^* to achieve the immobile landfast ice in the Siberian Seas would have Arctic wide consequences for the ocean properties. Therefore we decided for a parameterization that would only effect the local sea ice properties in the shallow and river runoff characterized Siberian Seas.

In our third paper:

Polona Itkin, Martin Losch and Rüdiger Gerdes, 2014: **Landfast ice affects the stability of the Arctic halocline: evidence from a numerical**

model. Submitted to the Journal of Geophysical Research - Oceans,

we return to the research problem of the sea ice drift and landfast ice in the Siberian Seas. We present a landfast parametrization depending on the bathymetry, where we double the P^* and introduce the sea ice tensile strength T (resistance to divergence) in the coastal regions shallower than 30 m. This creates an immobile sea ice cover that shields the river plume residing on the shelf from the wind stress and positions the polynyas further offshore in the more saline waters. A sensitivity study where we compare a control run (CTRL) to a run with the landfast ice parametrization (LF) shows that the landfast ice has local impact on the sea ice thickness and Arctic wide impact on the halocline stability. We recommend to include our simple landfast parametrization into the regional climate and biogeochemical models that study freshwater distribution, water column stability and nutrient availability.

Chapter 2

Validating Satellite Derived and Modeled Sea Ice Drift in the Laptev Sea with In-Situ Measurements of Winter 2007/08

Abstract

A correct representation of the ice movement in an Arctic sea ice - ocean coupled model is essential for a realistic sea ice and ocean simulation. The aim of this study is to validate the observational and simulated sea ice drift for the Laptev Sea shelf region with in-situ measurements of winter 2007/08. Several satellite remote sensing datasets are first compared to the mooring measurements and afterwards to the sea ice drift simulated by the coupled sea ice-ocean model. The different satellite products have a correlation to the in-situ data ranging from 0.56 to 0.86. The correlations of sea ice direction or individual drift vector components between the in-situ data and the observations are high, about 0.8. Similar correlations are achieved also by the model simulations. The sea ice drift speed of the model and of some satellite products have only moderate correlations of about 0.6 to the in-situ record. The standard errors for the satellite products and model simulations drift components are similar to the errors of the satellite products in the central Arctic and are in the range of 0.03 m/s. The fast ice parameterization implementation in the model was also successfully tested for its influence on the sea ice drift. The model drift simulation have contrary to the satellite products a full temporal and spatial coverage and results are reliable enough to use them as sea ice drift estimates on the Laptev Sea shelf.

2.1 Introduction

A faithful simulation of the sea ice velocities in a coupled sea ice-ocean model is one of the key prerequisites for a reliable simulation of the sea ice, ocean and atmosphere parameters. To achieve it, data gathered by manned stations, drifting bouys and lately satellite sensors have been used extensively in pan-Arctic sea ice model validations (Lemke et al, 1997; Kreyscher et al, 2000a; Martin and Gerdes, 2007) and data assimilations (Meier et al, 2000; Rollenhagen et al, 2009). For the remote coastal regions such as the Laptev Sea shelf there are very few ice drift field observations available. Satellite remote sensing products offer a large improvement in the spatial and temporal availability of observational data, but the retrieval algorithms give products with discontinuous temporal coverage at the grid points closest to the coast (Ezraty et al, 2006; Lavergne et al, 2010) that are consequently hard to inspect for inconsistency.

Sea ice motion is important as a transport of fresh water and latent heat. Its

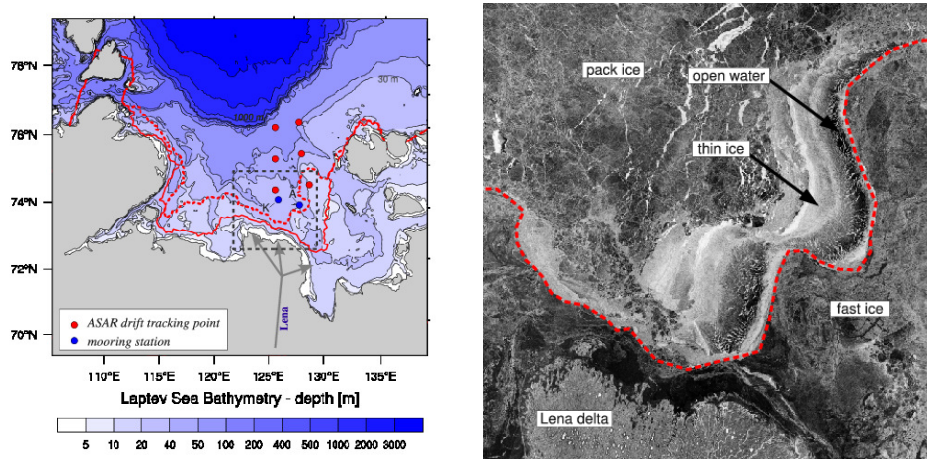


Figure 2.1: Left: Laptev Sea bathymetry (Jakobsson et al, 2008). The fast ice extents in December 2007 (solid red line) and in May 2008 (dashed red line) determine the position of the mid-shelf flaw polynya. The mooring stations Anabar and Khatanga are labeled by letters "A" and "K", respectively. The distance from the fast ice edge to the mooring stations changes from about 100 to 20 km, while the distance to the furthest ASAR tracking point changes from about 300 to 250 km during the winter. The black dashed box represents the area of the ASAR image on the right. Right: ASAR (Advanced Synthetic Aperture Radar) satellite image from 30th April 2008 showing the fast ice in the southeastern Laptev Sea. The Lena delta is at the bottom of the image. An advanced flaw polynya with low backscatter values in the open water area (dark area) developed at the fast ice edge (marked by dashed red line). The high backscatter values (bright area) in the polynya indicates presence of the newly formed ice.

shear and convergent motion causes dynamical ice growth and influences the ice thickness distribution. The sea ice drift, and in particular the divergent sea ice motion causes opening of leads and polynyas. The extensive Laptev Sea polynya system (Figure 2.1) is estimated to contribute as much as 20% of the sea ice area transported through Fram Strait (Rigor and Colony, 1997) Despite this there was so far no validation of the sea ice drift focusing on the Laptev Sea shelf, where low ice concentrations and fast movements in the polynya zones could influence the quality of the ice drift products (Ezraty et al, 2006).

North Atlantic/Arctic Ocean Sea Ice Model (NAOSIM) that we use in this paper (model is described in more detail in section Model Description) gives a relatively good representation of the large scale Arctic sea ice features such as Beaufort Gyre, Transpolar Drift and sea ice export out of Fram Strait (Karcher et al, 2003; Martin and Gerdes, 2007). However, the performance of this pan-Arctic model in the sea ice drift over the shelf has yet not been validated. The primary aims of this paper is to examine the quality of the available ice drift data and use it for a simple validation of the model results on the Laptev Sea shelf.

Similarly to other sea ice models NAOSIM is not able to simulate the formation of fast ice (König Beatty and Holland, 2010; Adams et al, In press). Due to this deficiency the simulated flaw polynya does not occur at the fast ice edge, but directly at the coast instead. The dislocation of the polynya results in severe regional biases in sea ice concentration, ice growth, ice thickness, winter temperature and salinity distribution. A significantly improved representation of sea ice concentration as well as ocean temperature and salinity distribution was obtained by including the fast ice in the model (Rozman, 2009; Adams et al, In press). The fast ice edge region is usually referred to as the mid-shelf, while the regions coastward and seaward from the edge are referred to as inner and outer shelf, respectively. The secondary aim of this paper is to show that in the outer shelf the parameterization does not have a significant impact on the sea ice drift.

2.2 Observational Data

Observational data analyzed in this study are in-situ data from two moored stations as well as satellite remote sensing products. Mooring data were retrieved from upward-looking Acoustic Doppler Current Profilers (ADCP Teledyne-RDI Workhorse Sentinel 300 kHz) deployed by the "Laptev Sea System Project"

in the eastern Laptev Sea mid-shelf. The mooring station "Anabar" was deployed at 74.33°N , 128.00°E at a depth of 30 m and station "Khatanga" at 74.71°N , 125.29°E at a 43 m depth (Figure 2.1). The devices were operating from September 2007 until August 2008 and they were recording the ice movements at the sea surface above them as described by Belliveau et al (1990).

All available sources of satellite-based ice drift products regardless the spatial resolution were used for the validation of the model simulations. Table 2.1 shows an overview of the used data.

The sea ice drift vectors distributed by Center for Satellite Exploitation and Research (CERSAT), at the French Research Institute for Exploitation of the Sea (IFREMER), Plouzané (France), were processed from pairs of Advanced Microwave Scanning Radiometer aboard EOS/Aqua (AMSR-E) images acquired by the 89 GHz channels and with 6.25 km pixel size (Ezraty et al, 2006) - from here on we name the product IFREMER. The gridded drift data has a spatial resolution of 31.25 km. For this study, 3-day drift vectors were used. The dataset is only available from October until the onset of ice melt at the beginning of May and has quality flags indicating the input data and method used for the drift estimation.

The second ice drift product used for the validation is the low resolution sea ice drift dataset (62.5 km equally spaced grid) of the EUMETSAT Ocean and Sea Ice Satellite Application Facility (OSI-SAF) (Lavergne et al, 2010), also processed from AMSR-E images and available from October till May. Conversely to the IFREMER product, it computes 2-day ice motion vectors from the 37 GHz channels (12.5 km pixel size), hence the coarser spatial resolution. The Laptev Sea has many coastal areas and two vast archipelagos. Consequently, the coarse resolution of the latter product considerably limits its use for comparison in the southernmost parts of the sea. At the Khatanga mooring location no OSI-SAF data are available and a point more northward had to be analyzed instead.

The third ice drift product we generated from Advanced Synthetic Aperture Radar (ASAR) satellite images. An ASAR image covers an area of approximately $400 \times 800 \text{ km}^2$ with a spatial resolution of $150 \times 150 \text{ m}^2$ (Cordey et al, 2004). We used the ASAR scenes for the sea ice drift detection at the mooring locations and at six locations in the eastern Laptev Sea outer shelf (Figure 2.1) chosen in a way to form a 1° grid. We manually tracked the movements of remarkable ice floes in the vicinity of these points to obtain drift vectors. The floes were tracked inside a search window with a radius proportional to the scale of the ice drift and preferably chosen in a way that they drifted directly

through the grid points. On average the search window radius was under 5 km. The ASAR images were available from November until April with major gaps in January and March. The time difference between two images varies from 2 to 4 days.

	temporal availability	initial temp. resolution	source	spatial resolution	type	quality flags	error estimate
ADCP	September 2007- August 2008	30 min	mooring	2 points	E	no	0.0004 m/s
IFREMER	October- April	3 days	AMRS-E/ EOS-Aqua	31.25 km	L	yes	0.026 m/s, 35°
OSI-SAF	October- April	2 days	AMRS-E/ EOS-Aqua,	62.5 km	L	yes	0.015 m/s
ASAR	November- April	12 h - 4 days	ASAR/ ENVISAT	1° (5 km)	L	no	0.004 - 0.002 m/s

Table 2.1: The overview of the datasets used in the validation. Type 'E' stands for Eulerian type of motion and type 'L' for Lagrangian. The error estimate for the ADCP instrument given here is a mean error velocity of the Khatanga mooring record. This error is estimated on the basis of the difference between the velocities measured by the four beams of the device and is a measure of combination of a horizontal homogeneity and errors caused by malfunctioning equipment (Instruments, 1996). The error for the Anabar mooring which was later corrected for the compass bias is larger - 0.001 m/s.

The estimated errors of the satellite remote sensing data are low. Validation of both, the IFREMER 3-day ice drift and the OSI-SAF 2-day product have been conducted against drifting buoys in the central Arctic (Ezraty et al, 2006; Lavergne et al, 2010). For the IFREMER product Girard-Ardhuin and Ezraty (2005) report standard deviations of 6.7 km and 35°, which corresponds to 0.026 m/s uncertainty on the drift speed. For the OSI-SAF product Lavergne et al (2010) document a standard deviation of 2.6 km, which translates into 0.015 m/s uncertainty on the zonal and meridional drift component. One should note, however, that the reference dataset used for both validation exercises were different, as well as the collocation methods and time period.

ASAR drift was extracted from the geolocated images. The geolocation uncertainty could result in an error of up to 2 pixels (300 m) (Rosich and Meadows, 2004). We estimate that the deformation of the tracked ice floe could contribute to an error of another 1-3 pixels and therefore result in a drift error for the tracked floe of around 0.004 m/s. The true error of the ASAR drift compared to the real velocities at the tracking points (position of the tracked ice

floe was not exactly at the tracking point) is unknown. The ice drift situation in the northern 4 points was homogeneous, while the southern most points were very close to the flaw polynya where the sea ice drift is more heterogeneous.

2.3 Model Description

NAOSIM is a coupled ocean-sea ice model developed at Alfred Wegener Institute for Polar and Marine Research (Gerdes et al, 2003; Karcher et al, 2003; Fieg et al, 2010). The model domain encloses the northern North Atlantic, the Nordic Seas and the Arctic Ocean. The highest resolving version of NAOSIM (Fine Resolution Model) has a horizontal grid spacing of $1/12^\circ$ on a rotated spherical grid where the equator runs across the North Pole. Near the surface vertical resolution is 10 m. The ocean component of the model is based on the Modular Ocean Model MOM-2 of the Geophysical Fluid Dynamics Laboratory (Pacanowski, 1995). It is coupled to a dynamic-thermodynamic sea ice model (Hibler, 1979) which employs a viscous-plastic rheology. The wind forcing in this experiment was taken from the 6-hourly NCAR/NCEP (National Centers for Environmental Prediction/National Center for Atmospheric Research) re-analysis data. Fast ice information (Figure 2.1: left) was integrated in the model in a way that the fast ice covered cells were excluded from the calculation of the sea ice momentum balance. Fast ice remained at rest while all thermodynamic calculations were performed as usual. Such procedure was already successfully applied by Lieser (2004). There a fast ice parameterization on the basis of sea ice thickness and bathymetry in a $1/4^\circ$ model was used. To enable a realistic representation of the flaw polynya processes in our high resolution model, we used prescribed high resolution fast ice area instead. Monthly fast ice masks for winter 2007/08 (from December to May) were obtained from thermal bands of Moderate Resolution Imaging Spectroradiometer (MODIS) sensor aboard EOS/Aqua (Adams et al, In press).

2.4 Data Analysis Methods

All ice drift data, modeled and observed, were converted to 3-day running mean ice drift to average out tidal and inertial movements of sea ice and obtain comparable quantities. The OSI-SAF 2-day means were first divided into daily means and then re-averaged to 3-day means. The low temporal resolution did not allow a complete averaging of the ASAR drift estimates for which in

some cases single values were used to represent the 3-day period. The satellites carrying AMSR-E and ASAR sensors fly over the Laptev Sea twice per day, usually at noon and midnight. The three day means in all of the AMSR-E products are calculated from noon first day until noon of the fourth day (in total 3 to maximum 8 overflights as the neighboring scenes overlap in high latitudes). To avoid a phase shift between the datasets also the mooring and modeled ice drift was calculated for the same time window. As noon images of ASAR are rare most of the images we analyzed were taken at midnight (typically 2-3am UTC) and consequently the ASAR time series still have a small time shift compared to other time series.

We converted the data on the meridional and zonal sea ice movement to two sea ice drift properties: speed (magnitude) and direction (angle) and analyzed them separately. We first examined the time series of speed and sine of direction for all datasets and checked that there is no or minimal time shift between them. In section Observed Sea Ice Drift we show results of the linear regression analysis for the correlations between the observational datasets for speed and circular regression for the directional correlations. The ADCP record has the full time coverage and is the only dataset measured in-situ at the drifting ice surface. Despite this the mooring record represents a point measurement, while the satellite products represent gridded information (as also the model output is) produced from individual daily snapshots. No mooring with ice drift recording device has ever been recovered in the Laptev Sea outer shelf. In this paper we therefore compared the ADCP data to all other observational datasets in the mid-shelf. In the outer shelf, where no such data is available, we made a cross-comparison of all other data. In section Simulated Sea Ice Drift we then show the correlations between the observational data and the model simulations. If available we also analyzed the observational data with the best quality flags only. Finally, in section Drift Vector Validation we compare the zonal and meridional drift vectors of all satellite remote sensing products and model simulations to the in-situ data. This eases the comparison with previously published validation statistics for the central Arctic.

Statistics such as linear regression analysis are not appropriate for the analysis of the circular data where the numerical value for the parameter depends on the assignment of zero-direction and direction of rotation. The angles such as 0° and 359° are as numerical values very distant and would result in erroneous mean values if regular arithmetic mean is applied. Various circular (directional) statistics methods have been suggested and used over the past decades to overcome this problem (Fisher, 1996; Jammalamadaka and Sengupta, 2001). The

mean of an angular dataset is computed by treating all angular measurements as points on a unit circle, and computing the resultant vector of the unit vectors determined by the data points (Fisher, 1996; Jammalamadaka and Sengupta, 2001). The mean direction is the direction of this resultant vector, and the mean resultant length provides a measure of concentration of the circular data. For the angular data α with statistical population n , mean direction $\bar{\alpha}$ is defined as

$$\bar{\alpha} = \begin{cases} \arctan\left(\frac{S}{C}\right) & \text{if } S > 0, C > 0 \\ \arctan\left(\frac{S}{C}\right) + \pi & \text{if } C < 0 \\ \arctan\left(\frac{S}{C}\right) + 2\pi & \text{if } S < 0, C > 0 \end{cases} \quad (2.1)$$

where S and C are

$$S = \sum_{i=0}^n \sin(\alpha_i) \quad (2.2)$$

$$C = \sum_{i=0}^n \cos(\alpha_i) \quad (2.3)$$

The circular variance is defined as $1 - \bar{R}$ where $R = \sqrt{S^2 + C^2}$ and $\bar{R} = R/n$. Its values fall in the interval $[0, 1]$, where data highly concentrated around one direction take values close to 0, while widely dispersed data have values close to 1. Statistical mean and variance for linear variables x, y or circular variables α, β were then used for calculation of statistical bias ($\bar{x} - \bar{y}$ or $\bar{\alpha} - \bar{\beta}$) and variance ratio F (var_x/var_y or var_α/var_β).

One of the possible measures of correlations between two circular variables was suggested by Jammalamadaka and Sengupta (2001) where for two angular data sets α and β the circular correlation coefficient $r_{\alpha\beta}$ is defined as

$$r_{\alpha\beta} = \frac{\sum_{i=1}^n \sin(\alpha_i - \bar{\alpha}) \sin(\beta_i - \bar{\beta})}{\sqrt{\sum_{i=1}^n \sin^2(\alpha_i - \bar{\alpha}) \sin^2(\beta_i - \bar{\beta})}} \quad (2.4)$$

If α and β are independent, $r_{\alpha\beta}$ is close to 0 and if the two variables are rotationally dependent the $r_{\alpha\beta}$ would be close to ± 1 . The correlation is then

defined as $r_{\alpha\beta}^2$. This is an analogue formula to the classical linear regression correlation coefficient where for two linear variables x and y the correlation coefficient r_{xy} is defined as $r_{xy} = \frac{\sum_{i=1}^n (x_i - \bar{x})(y_i - \bar{y})}{\sigma_x \sigma_y}$.

2.5 Observed Sea Ice Drift

Figure 2.2 shows scatter diagrams and statistical coefficients for the Khatanga and Anabar mooring locations in the mid-shelf. The ADCP and IFREMER datasets agree well in the direction of the drift. The statistical correlation between datasets are high ($r^2 = 0.8$), statistical bias is low and variance ratio (F) is close to 1. The correlations of ASAR and OSI-SAF datasets to the ADCP record are lower ($r^2 = 0.6$) with both, ASAR and OSI-SAF datasets underestimating the ADCP measured speeds. There was no OSI-SAF drift point available for the exact Khatanga location and a point further off-shore was analyzed instead. Consequently it is not surprising that the correlations of all datasets with the OSI-SAF are moderate.

On the outer shelf correlations between the datasets are higher than in the mid-shelf region (r^2 from 0.65 to over 0.8). In Figure 2.3 we show scatter diagrams and statistical coefficients for the combination of data for all six points on the ASAR grid.

2.6 Simulated Sea Ice Drift

The time series of sea ice drift speed and direction in Figures 2.4 and 2.5 show that the model is simulating the ice drift in comparison with the observed drift well. The model is underestimating the ADCP velocities, but is simulating all of the peak speed events from the consolidation of the sea ice cover in November on. The directions during the high speed events are represented correctly. Erroneous drift directions occur mainly during the events with low drift speed. The speeds lower than 0.035 m/s would contribute to a displacement up to 9 km during the 3-day averaging period. As this movement is a subgrid process for a model with $1/12^\circ$ horizontal grid resolution we excluded this directions from the circular regression analysis. The displacements smaller than half of a pixel (3.12 km for IFREMER product and 6.25 km for OSI-SAF) are also not detectable by the tracking algorithms. Apart from a slight reduction in speed in the second part of the winter there is no significant change in ice drift

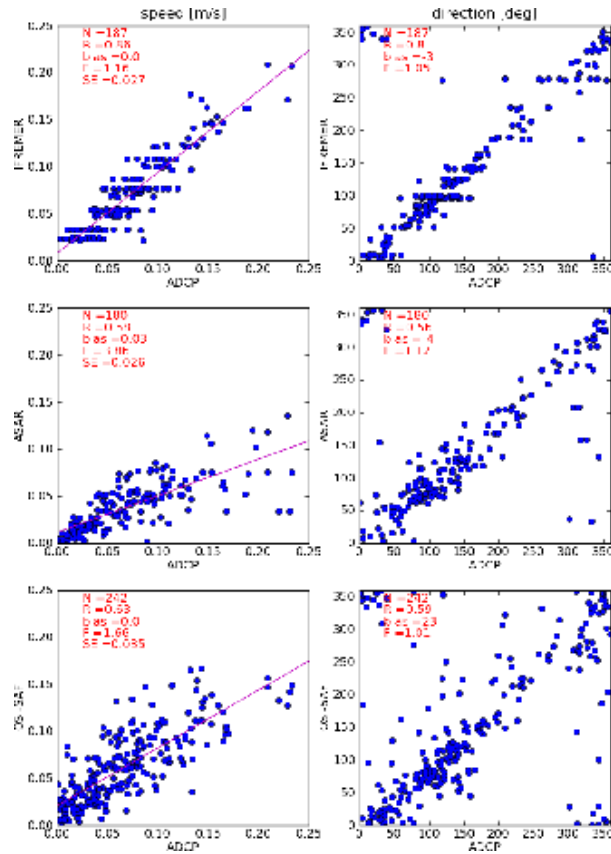


Figure 2.2: Scatter plots of sea ice drift speed and direction at the Anabar and Khatanga mooring locations for observational data comparison from November 2007 till May 2008. The numbers on the plots show number of data pairs in the analysis - N , correlation value (r^2) - R , statistical bias - $bias$, variance ratio - F , standard deviation of the error - SE . Speed units are m/s and direction values are degrees. All correlations shown are statistically significant at probability 0.99 (P value less than 0.001).

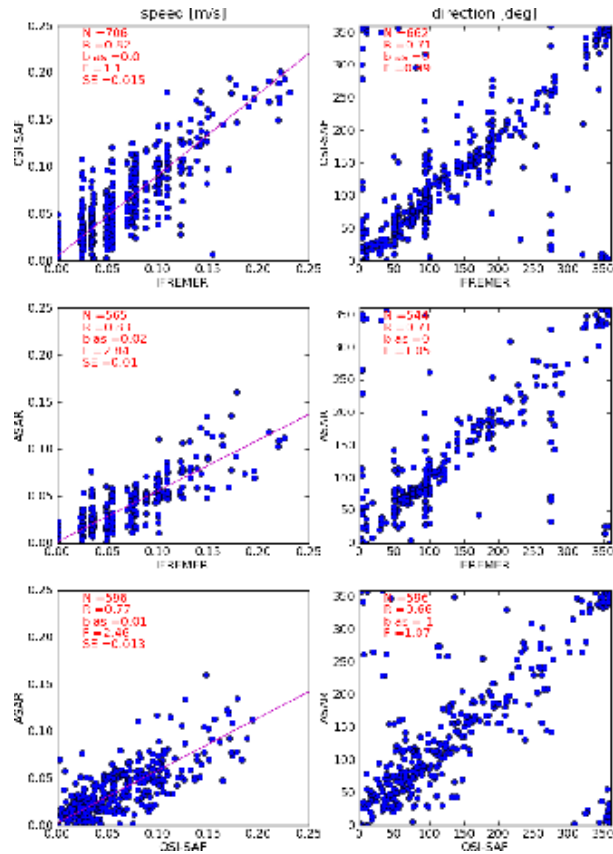


Figure 2.3: Scatter plots of sea ice drift speed and direction in the outer shelf for observational data comparison from November 2007 till May 2008. The numbers on the plots show number of data pairs in the analysis - N , correlation value (r^2) - R , statistical bias - $bias$, variance ratio - F , standard deviation of the error - SE . Speed units are m/s and direction values are degrees. All correlations shown are statistically significant at probability 0.99 (P value less than 0.001).

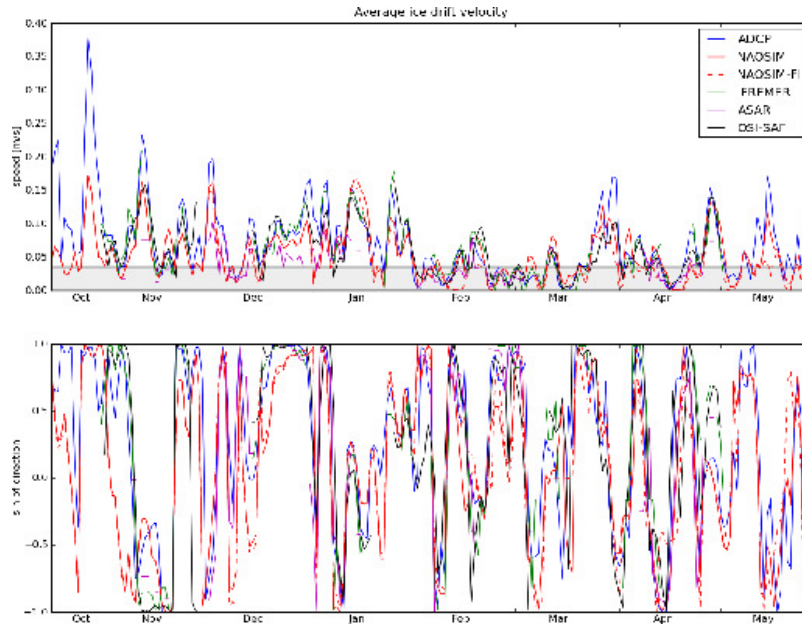


Figure 2.4: Simulated sea ice drift speed (top) and direction (bottom) without (full red line) and with (dashed red line) integrated fast ice compared to observational and remote sensing drift for the Khatanga mooring location from 15th October 2007 till 15th May 2008. The gray box in the top graphs marks the speeds that were not included into the directional correlation analysis.

simulation after the integration of the fast ice for any of the analyzed locations on the mid- or outer shelf (Figures 2.4 and 2.5).

Figures 2.6 and 2.7 show scatter diagrams and statistical coefficients of the observational data and the model simulations. The model speed simulations have low statistical bias compared to all observational data, but the variance ratio (F) is high when compared to all of the datasets, except compared to the ASAR drift speed. The simulated directions have a moderate bias, but variance ratio (F) slightly lower than 1.

The simulated sea ice speed at the mooring locations and in the outer shelf is moderately correlated to the observational speeds (r^2 from 0.4 to 0.7). The regression line shows a general underestimation of the speed compared to observations. Once the directions simulated at low speeds were removed from the statistical analysis the circular correlations to the observational datasets are moderate to high (r^2 from 0.5 to 0.9). Using only the best quality flags for the IFREMER and OSI-SAF datasets the number of data points in time reduces, but the correlations do not improve.

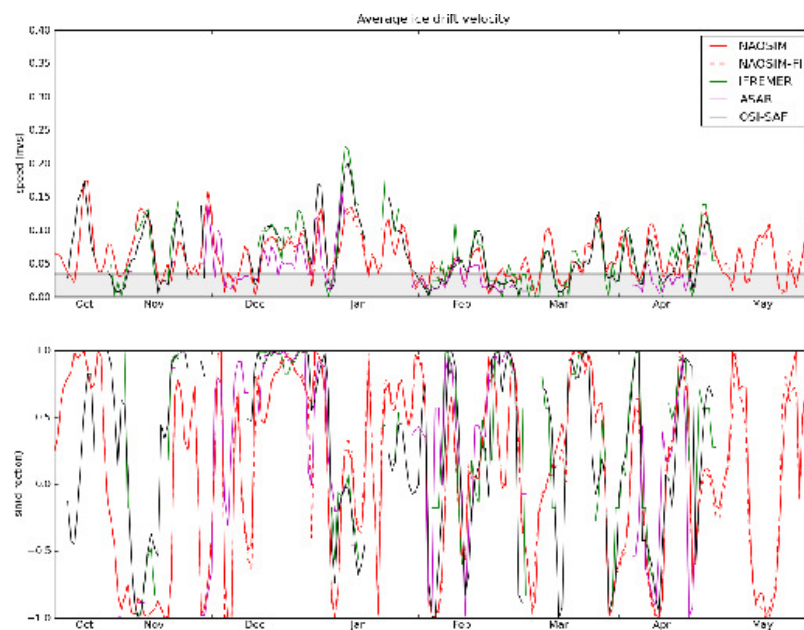


Figure 2.5: Simulated sea ice drift speed (top) and direction (bottom) without (full red line) and with (dashed red line) integrated fast ice compared to observational and remote sensing drift for the for a point in the outer shelf ($77^{\circ}N$, $125^{\circ}E$) from 15th October 2007 till 15th May 2008. The gray box in the top graphs marks the speeds that were not included into the directional correlation analysis.

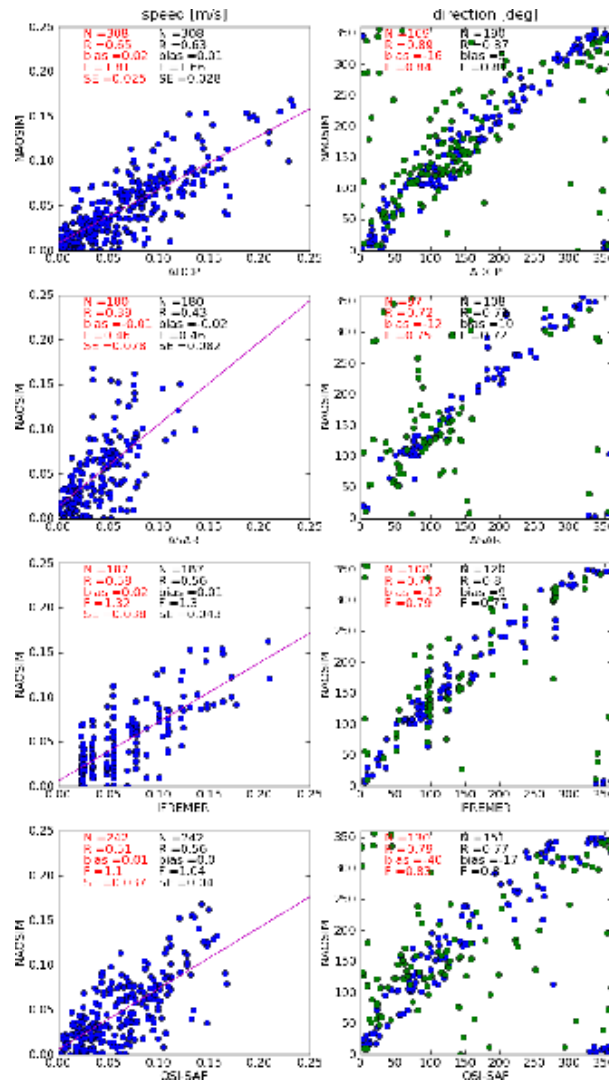


Figure 2.6: Scatter plots of sea ice drift speed and direction at the Anabar and Khatanga mooring locations for model simulation with the fast ice and observational data comparison from November 2007 till May 2008. The data points included into the statistical analysis are marked by blue dots. The points with drift speed under 0.035 m/s at the drift direction scatter plots are marked by green dots. The numbers on the plots show number of data pairs in the analysis - N , correlation value (r^2) - R , statistical bias - $bias$, variance ratio - F , standard deviation of the error - SE . Speed units are m/s and direction values are degrees. All correlations shown are statistically significant at probability 0.99 (P value less than 0.001). Numbers printed in red (black) show the statistical characteristics of the model simulations with (without) the fast ice.

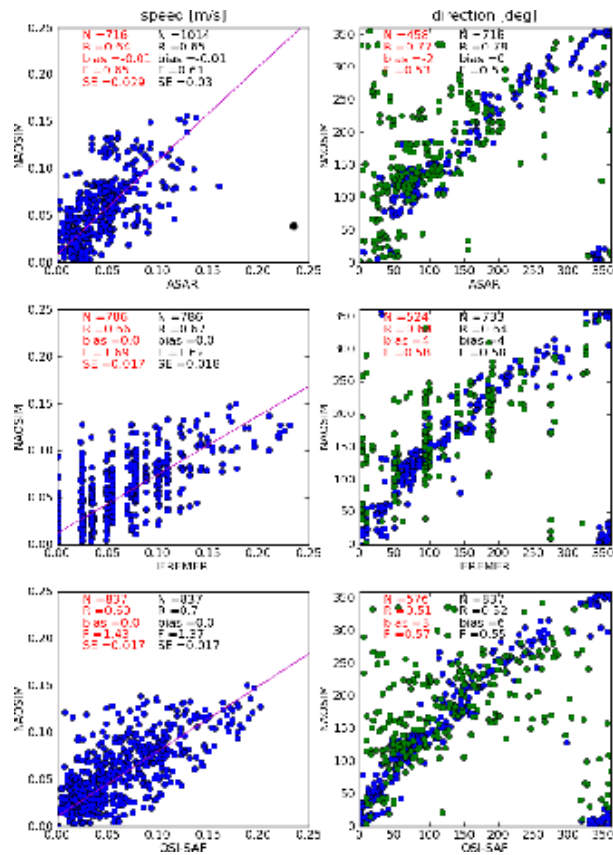


Figure 2.7: Scatter plots of sea ice drift speed and direction at in the outer shelf for model simulation with the fast ice and observational data comparison from November 2007 till May 2008. The data points included into the statistical analysis are marked by blue dots. The points with drift speed under 0.035 m/s at the drift direction scatter plots are marked by green dots. The numbers on the plots show number of data pairs in the analysis - N , correlation value (r^2) - R , statistical bias - *bias*, variance ratio - F , standard deviation of the error - SE . Speed units are m/s and direction values are degrees. All correlations shown are statistically significant at probability 0.99 (P value less than 0.001). Numbers printed in red (black) show the statistical characteristics of the model simulations with (without) the fast ice.

2.7 Drift Vector Validation

	N	$bias_{\bar{u}}$	$bias_{\bar{v}}$	$SD_{\bar{u}}$	$SD_{\bar{v}}$	$r_{\bar{u}}^2$	$r_{\bar{v}}^2$
IFREMER	187	-0.006	0.002	0.030	0.027	0.90	0.93
OSI-SAF	242	0.040	0.006	0.040	0.031	0.69	0.84
ASAR	180	0.003	0.005	0.027	0.021	0.73	0.86
NAOSIM	190	0.005	0.014	0.033	0.025	0.85	0.87
NAOSIM - FI	169	0.009	0.014	0.037	0.025	0.84	0.87

Table 2.2: The validation results of the drift vector components of the satellite products and model simulations with the in-situ measurements for the Laptev Sea mid-shelf in winter 2007/2008. The columns show statistical parameters for the zonal (\bar{u}) and meridional (\bar{v}) components of the drift: number of data pairs in the analysis - N , statistical bias - $bias$, standard deviation of the error - SE and correlation value - r^2 . Velocity units are m/s. All correlations shown are statistically significant at probability 0.99 (P value less than 0.001).

The comparison of the zonal and meridional drift component of satellite products and model simulations to the in-situ data shows high correlations (r^2 higher than 0.7, Table 2.2), but higher standard deviations of errors as in the central Arctic basin (Table 1). The mean measured error velocity for the Khatanga mooring ADCP is 0.0004 m/s (Table 1), while the error velocity for the Anabar, which compass bias was calibrated only after the instrument was recovered, is 0.001 m/s. For the model again only the drifts with speed higher than 0.035 m/s were analyzed.

2.8 Discussion

The observational data and model simulations were compared at two mooring locations in the mid-shelf dominated by the polynya activity and at six regularly spaced points in the outer shelf region where the thin ice gradually grows into the pack ice.

The comparison of the satellite observational data shows that ice drift directions are all moderately to highly correlated to the ADCP record. The IFREMER product is also highly correlated in speed. The ASAR and OSI-SAF speeds are only moderately correlated, regarding the temporal and spatial mismatch a relatively good result. While the ASAR datasets still have a small phase shift due to prevailing midnight overflights and 3-day averages based on a small number of images, the OSI-SAF product does not cover the Khatanga mooring location and an alternative location further offshore was used in comparison.

The scatter diagrams on Figures 2.2 and 2.3 show that the IFREMER dataset only occupy certain discrete values. This "quantization noise" is a well known effect of the robust Maximum Cross Correlation method (Kwok et al, 1998; Girard-Ardhuin and Ezraty, 2005; Lavergne et al, 2010) that the IFREMER dataset algorithm is using for the ice drift estimation. The effect causes no obvious problems at this stage of the model validation. The OSI-SAF product is using the Continuous Cross Correlation Method (CMCC) (Lavergne et al, 2010) which avoids this problem.

For the mooring locations the model simulation is in good agreement with the ADCP and satellite remote sensing data (Figure 2.4). The simulated ice drift speeds compared to these datasets are very similar starting from November, when the sea ice cover in the Laptev Sea becomes relatively stable. It is remarkable that the simulated and ADCP speeds match not only in phase, but also in magnitude and the model is able to simulate the early winter extreme velocities (peaks in Figure 2.4). The ice drift directions are similar for the whole observation period and especially during the high speeds. The time series also show the scarcity of the satellite retrieved data, which can be unavailable on the scale of weeks.

The statistical bias of the model results is much lower on the outer shelf than on the mid-shelf. The variance ratio (F) of directions decreases on the outer shelf as well and shows that the simulated model directions are more disperse than observed.

The correlations between all of the observational data and the model simulations are slightly higher on the mid-shelf than on the outer shelf. This is surprising as in the dynamic mid-shelf environment, dominated by polynya events, the model should have more difficulties with correct simulations than on the relatively homogeneous outer shelf. The reason for this unexpected result is probably a smaller number of observations analyzed on the mid-shelf. As we decided to exclude all of the drift directions for drift speed lower than 0.035 m/s, a relatively larger part of the data was excluded on the mid-shelf where the ice velocity is generally lower and only the fastest movements (top 50%) of the data entered the analysis. In the outer shelf almost 70% of all data entered the analysis.

There is still some remaining phase shift (Figure 2.4) between the model and the observations due to the temporal resolution of the wind forcing data. The 6-hour wind situation does not represent the wind changes during the 6 hour interval. The time shift error is occurring randomly and depends on the timing

of the wind direction change. This error can only be excluded by a high enough temporal resolution of the forcing data or by full coupling of the model.

Furthermore, differences in observed drift arise also because the measurement techniques are principally different. The model and the mooring velocities are Eulerian while the remote sensing velocities are Lagrangian. The high correlation between the ADCP and the IFREMER data shows that the averaged Lagrangian velocities around the mooring location are comparable to the Eulerian velocities measured over the mooring station. The classical sea ice drift validation was done with the drifting buoys that also represent a Lagrangian type of measurements (Ezraty et al, 2006; Lavergne et al, 2010). IFREMER and OSI-SAF drift products are spatial averages, while the ADCP record and ASAR drift data represent a non-averaged single point/floe drift. Each drift vector from the OSI-SAF product pertains to an area of approximately $120 \times 120 \text{ km}^2$ while the IFREMER vectors pertain to roughly $60 \times 60 \text{ km}^2$ (4 times less), thanks to the higher resolution of the 89 GHz channels. This results were then gridded to the spatial resolutions of 62.5 km and 31.25 km, respectively.

The model simulations and the ASAR dataset are systematically underestimating the in-situ measured speed, when velocities are higher than 0.1 m/s. The reasons for too low simulated drift speeds could be found in a too low wind stress or to high ocean drag influencing momentum balance of the sea ice in the model. The ASAR dataset peak speeds are systematically lower than the ones of IFREMER, OSI-SAF and ADCP by about a half. For the ASAR drift only remarkable features in sea ice such as big pressure ridges and hummocks were used for tracking. Despite a great surface roughness, detectable also by high backscatter signatures on the ASAR images, these features are not drifting as fast as one would expect from a greater wind stress acting on their sails. It seems that the friction between rough jagged floes is an important sink of energy for shearing at floe boundaries (Rothrock, 1975). The big ice floes, as used for tracking on the ASAR images, are therefore less appropriate for the estimation of the prevailing ice drift situation. The ASAR velocities which have been retrieved specifically for this research have still been proven to be an useful alternative source of information, independent from other satellite remote sensing products. In November and December, when there are occasionally no AMSR-E ice drift products available (Figures 2.4 and 2.5), ASAR derived speed and direction are similar to the in-situ measured and to the simulated.

The standard deviations of the error for the satellite products and model simulations validated with the ADCP record are in the range of 0.03 m/s (Table

2.2). Compared to the buoy validation performed in the central Arctic and Canadian Archipelago these errors are slightly higher (for 0.005 m/s) for the IFREMER (Ezraty et al, 2006) and double for the OSI-SAF product (Lavergne et al, 2010). This confirms our hypothesis that the errors of the estimates are higher over the shelf seas. The in-situ ice drift velocities measured in the Laptev Sea mid-shelf are relatively higher than in the buoy validation set that was used by Ezraty et al (2006) and Lavergne et al (2010). A part of this error can be certainly attributed to the inhomogeneous drift environment in the mid-shelf. The datasets used in this paper also exhibit frequent peaks in speeds over 0.1 m/s, while such events in the buoy datasets were not common. This suggests that despite the larger errors the satellite and simulated velocities are still relatively good estimates.

The fast ice parameterization has no major impact on the ice drift simulations apart from additionally reducing the drift speed in the mid shelf region during the periods with low speeds (in our case: from February on). This effect is hardly detectable further offshore (Figure 2.5). The correlations of model results with and without fast ice parameterization with the observational data are similar (Figures 2.6, 2.7).

NAOSIM was already validated by Martin and Gerdes (2007) with the product merged from Quick Scatterometer (QuikSCAT) and Special Sensor Microwave/Imager (SSM/I) drift estimations provided by CERSAT/IFREMER. The product has a spatial resolution of 62.5 km and is available for the central Arctic only. Using monthly means from 3- or 6-day products the validation was performed for the period 1992 - 2001. NAOSIM, similarly to other models in the Arctic Ocean Model Intercomparison Project (AOMIP), slightly overestimated the drift speeds. The model also had a slight deviation of the drift angles to the right. On the other hand, NAOSIM on the Laptev shelf underestimates the drift speed and has a slight angle deviation to the left. This again points at the systematic differences between the central Arctic and the shelf seas.

The above mentioned AOMIP intercomparison also revealed the differences between the simulations of different sea ice-ocean coupled models. Although it has been estimated that the 70 % of short term ice drift variability is explained by the wind variability (Thorndike and Colony, 1982) and the models in the project all used identical atmospheric forcing, the resulting sea ice drift simulations differed substantially (Martin and Gerdes, 2007). To explain the differences in the model performances Martin and Gerdes (2007) pointed out the differences in the implementation of the atmospheric and oceanic forcing,

among them the actual prescription of the wind stress and the implementation of the ocean-ice drag term.

For the NAOSIM in this case study the correlation of simulated sea ice drift to the in-situ data in sea ice direction or in individual vector components largely exceeds the 70 % of the variability that should be explained by the wind variability (Thorndike and Colony, 1982). This means that not only wind stress, but also other important contributors to the sea ice momentum balance such as the ocean-ice drag, the internal sea ice stress and the Coriolis force (Harder et al, 1998), are realistically implemented in the model. Another evidence for the role of the ocean and ice dynamics in the model is the spatial variability between the drift records at the Khatanga mooring location (Figure 2.4) and in the outer shelf (Figure 2.5). The difference between the both time series is much larger as expected from a difference between two grid points of the wind forcing data with a spatial resolution of 1.875° (Kanamitsu et al, 2002).

2.9 Conclusions

In this paper we used unique in-situ sea ice drift records from the Laptev Sea shelf to validate the satellite remotes sensing products and model simulations. Our results show that:

1. The fast ice parameterization in the model has no major impact on the sea ice drift simulations and it's smoothing effect disappears already at distance larger than 100 km (about 10 model grid points).
2. The standard deviations of the error for the satellite products validated with the in-situ record are larger on the shelf than in the central Arctic. The errors for the satellite products and model simulations are in the range of 0.03 m/s.
3. The sea ice drift remote sensing products compared to the in-situ mooring records give good estimates for the shelf regions. Especially the high resolution IFREMER product has a high correlation and low standard deviation compared to the in-situ data.
4. For the validation of the sea ice drift on the Eurasian shelf simulated by the eddy resolving sea ice models we recommend the use of the in-situ data and high resolution satellite retrieved products. Because of the

differences between the products in our validation we recommend to use more than one satellite product for the validation.

5. The correlation of simulated sea ice drift to the in-situ data in sea ice direction or in individual vector components is at least 0.84. To achieve a more realistic simulations of the drift speed, the calculation of the wind stress and ocean drag terms should be studied closely. The model drift simulation have contrary to the satellite products a full temporal and spatial coverage and the correlations to the in-situ data are high enough to use them as sea ice drift estimates on the Laptev Sea shelf.

Acknowledgments

This research was conducted as part of the BMBF project "System Laptev Sea" (03G0639A). ENVISAT/ASAR satellite images were obtained through ESA Project EO-500 "Formation, transport and distribution of sediment-laden sea-ice in the Arctic Shelf seas". P.R. would like to express her gratitude to the Slovenian Academy of Science and Art, to the Municipality of Ljubljana, Slovenia and to the Otto-Schmidt-Laboratory, Saint Petersburg, Russia for supporting her master studies with scholarships and grants. The authors would like to thank the anonymous reviewers whose helpful comments and criticism provided substantial improvements of the manuscript.

Chapter 3

Is weaker Arctic sea ice
changing the Atlantic water
circulation?

Abstract

With a numerical model we test the sensitivity of the Arctic Ocean circulation at mid-depth (212-1200 m) to the change in the sea ice rheology parameter P^* that controls the sea ice compressive strength. We show that the reduction of the sea ice strength via P^* within commonly used envelope reduces the sea ice extent and consequently enhances the ocean surface heat loss in the marginal ice zone. This leads to cooling of the Atlantic water inflow into the Arctic Ocean. As a result Eurasian Basin and Amerasian Basin temperatures are in average cooled by 0.1 °C and 0.05 °C, respectively. An increased sea ice drift speed in the central Arctic leads to an enhanced circulation of the anticyclonic Beaufort Gyre of the Amerasian Basin, which in turn weakens the cyclonic Atlantic water circulation below and enhances the recirculation of the Atlantic water in the Eurasian Basin. Consequently the balance of the volume fluxes through the Arctic gateways changes. Fram Strait net outflow increases by 0.46 Sv, Barents Sea Opening net inflow increases by 0.19 Sv and Davis Strait net outflow decreases by 0.28 Sv. This may spread the effects of the sea ice strength change beyond the limits of the Arctic Ocean and into the deep water convection zones in the North Atlantic. These substantial effects should be considered also in the model optimization efforts where P^* is commonly used as one of the tuning parameters to achieve better sea ice simulations, whereas the effects on the ocean circulation are rarely taken into account.

3.1 Introduction

Where the Arctic Ocean is covered by sea ice, its fresh upper ocean waters are close to the freezing point. At mid-depth the Arctic Ocean has temperatures up to several degrees above zero, ranging from about 4 °C at the inflow in Fram Strait to 0-1 °C in the central Arctic Ocean. The bulk of this warm and salty water is composed of Atlantic Water (AW) that enters the Arctic Ocean through the Fram Strait and the Barents Sea (Rudels et al, 1994). The multi-year surface circulation is characterized by the anticyclonic Beaufort Gyre in the Amerasian Basin and a Transpolar drift that transports the sea ice and surface water towards the Fram Strait (light blue arrows on Fig. 2.1). The extent of the Beaufort Gyre and the orientation of the Transpolar drift change on multi-year timescale, driven by changes in the large scale wind fields. A high Arctic Oscillation (AO) leads to small Beaufort Gyre and a Transpolar drift oriented from the Bering Strait to Fram Strait, while a low AO leads to a large

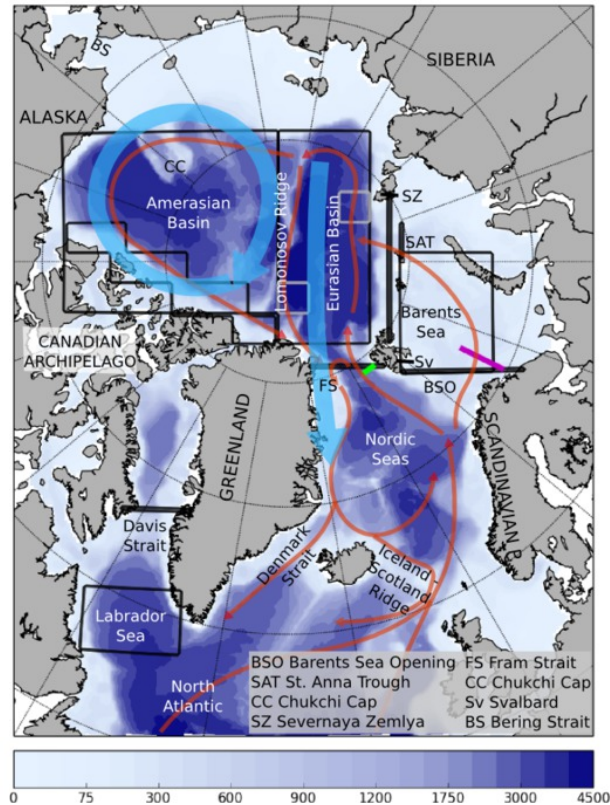


Figure 3.1: The model domain and bathymetry. The sea ice and surface circulation is schematically represented by light blue arrows and the mid-depth circulation by red arrows (for the Arctic Ocean simplified from Rudels et al (1994) and for the Nordic Seas and North Atlantic from Eldevik et al (2005)). The oceanographic sections for the comparison with the observational data in the West Spitzbergen Current and the Kola section in the Barents Seas are marked by green and purple color, respectively. The black lines and black and grey boxes mark the sections and regions used in the model analysis.

Beaufort Gyre and shifts the Transpolar drift axis eastward. In contrast, the mid-depth circulation of the Atlantic Water Layer (AWL), typically defined by its potential temperatures as roughly above 0 °C below the halocline which is located at about 200 m depth (300 m depth in the Beaufort Sea) (Carmack et al, 1997; Swift et al, 1997), is characterized by generally cyclonic motion, most of which occurs in boundary currents along the deep ridges and shelfbreaks (red arrows on Fig. 2.1, Rudels et al (1994)). Before entering the central Arctic Ocean basins Fram Strait Branch (FSB) and the Barents Sea Branch (BSB) experience heat loss and are modified by ice melt and freeze-up, the latter also by river runoff (Rudels et al, 1994). Both AW branches feed the AWL and after passing through the basins leave the Arctic ocean on return through the Fram Strait as Arctic Intermediate Water (AIW). The AIW flows into the Nordic Seas and has an important role in the dense water formation that feeds the Atlantic Meridional Overturning circulation (Schmitz and McCartney, 1993; Swift, 1984). The pathways of the AWL circulation as deduced from hydrographic observations were confirmed by dispersion of anthropogenic tracers in observations and model experiments (Smith et al, 1999; Karcher et al, 2012). Based on model simulations and few observations, recently questions have been raised regarding periods of potential breakdown or even reversal of the cyclonic circulation of the upper part of the AWL in the Amerasian Basin (Karcher et al, 2012). Additionally, recent observational studies report on the warming of the FSB (Beszczynska-Möller et al, 2012) as well as the AWL in the central Arctic (Polyakov et al, 2005b; Dmitrenko et al, 2008b).

Along with the changes in the ocean also the Arctic sea ice cover is changing: it is getting thinner (Kwok and Rothrock, 2009), more mobile (Rampal et al, 2009; Spreen et al, 2011) and the sea ice extent is shrinking (Stroeve et al, 2012). The reasons for the changes have been investigated in various observational and modeling studies (Shimada et al, 2006; Perovich et al, 2008; Polyakov et al, 2010; Kattsov et al, 2010; Zhang et al, 2012) that revealed that the observed changes are complex and connected with numerous feedbacks. In an attempt to artificially isolate and understand the effects of only one changing sea ice property, the sea ice strength, we perform a modeling sensitivity experiment by changing the value of a single rheology parameter and pay specific attention to the response in the ocean.

It has been hypothesized that the inflow of the warm AW to the Arctic Ocean has an influence on the decline of the sea ice extent and thickness (Polyakov et al, 2010; Ivanov et al, 2012). In our study we investigate if there is any reverse connection: can a change in the Arctic sea ice characteristics influence

the flow in the AWL and the AIW outflow?

In numerical models sea ice motion is based on employing a rheology (e.g. Hibler (1979); Hunke and Dukowicz (1997)) that connects the sea ice motion to the sea ice mechanical properties. One of these properties is the maximal compressive sea ice strength (P). In the viscous-plastic rheology introduced by Hibler (1979) P is described by the formula

$$P = P^* h \exp(-C^*(1 - A)), \quad (3.1)$$

where h and A are sea ice thickness and concentration, whereas P^* and C^* are sea ice strength parameters that are empirical constants. While changing C^* does not have a major effect on the sea ice properties (Juricke et al, 2013), P^* needs to be set in a way to optimize sea ice drift (Hibler and Walsh, 1982; Kreyscher et al, 2000b) or can be estimated from observational data by calculating the force exerted by the wind over sea ice (Tremblay and Hakakian, 2006). The P^* values estimated by Hibler and Walsh (1982) and Kreyscher et al (2000b) are 15.000 N/m² and 27.500 N/m². None of these two values is extreme, both fit well into the interval of commonly used values (e.g. 5000 - 50000 N/m² used by Sumata et al (2013); 5000 - 35000 N/m² used by Juricke et al (2013)) and are often used in the Arctic sea ice-ocean models (Martin and Gerdes, 2007). The aim of our research is to examine the sensitivity of the ocean simulations to the model optimization exercises by changing P^* as this is often overlooked.

The outline of this paper is as follows. In section 3.2 we describe the model and experimental setup. Section 3.3 contains an assessment of the model performance using observations. In sections 3.4, 3.5 and 3.6 we present and discuss the simulation results. A summary of our findings and final remarks are in section 3.7.

3.2 Model and sensitivity study setup

Our model is a regional coupled sea ice ocean model based on the Massachusetts Institute of Technology General Circulation Model code - MITgcm (Marshall et al, 1997; MITgcm Group, 2014a) with the model domain covering the Arctic Ocean, Nordic Seas and northern North Atlantic (Fig. 2.1). The horizontal resolution is 1/4° (~28 km) on a rotated grid with the grid equator crossing

the geographical North Pole along 30°W . The model vertical grid consists of 36 unevenly distributed levels. The upper ocean spanning from 0 to 212 m is resolved in 15 levels with thickness increasing from 2 to 42 m. The mid-depth ocean spanning from 212 to 1200 m is resolved in 12 levels with thickness increasing from 43 to 100 m. The deep ocean layer spanning from 1200 to 4500 m is resolved in 10 levels with thickness spanning from 100 to 500 m. Thus, the resulting vertical resolution of the surface layer is enhanced on the account of the poor resolution in the deep layer. The AWL layer in this study is defined by the constant depth boundaries of 212 and 1200 m. Vertical mixing in the ocean interior is parameterized by a K-Profile Parameterization (KPP) scheme (Large et al, 1994) and tracers (temperature and salinity) are advected with an unconditionally stable seventh-order monotonicity preserving scheme (Daru and Tenaud, 2004) that requires no explicit diffusivity. The sea ice model is a dynamic-thermodynamic sea-ice model with a viscous-plastic rheology described by Losch et al (2010) and based on Zhang and Hibler (1997). The model has a non-linear free surface and sea ice that depresses the surface ocean layer according to its mass. We avoid numerical issues associated with too thin ocean surface layer when the ice becomes too thick by using a rescaled vertical coordinate z^* (Campin et al, 2008) that distributes the excursion of the free sea surface between all vertical levels to the bottom.

The model is initialized by the PHC climatology (Steele et al, 2001) and has initially no sea ice cover. For the spin-up we run the model for 30 years with atmospheric climatology from the Coordinated Ocean Research Experiment (CORE) version 2 based on the reanalysis from the National Center for Atmospheric Research/National Centers for Environmental Prediction (NCAR/NCEP) (Large and Yeager, 2009). Subsequently the model is driven from 1948 to 2007 by realistic daily atmospheric data also provided by CORE. Surface salinity in ice free regions is restored to a mean salinity field (PHC climatology) with a time scale of 180 days to avoid model drift. River runoff was prescribed for the main Arctic rivers according to the Arctic Ocean Model Intercomparison Project (AOMIP, <http://www.whoi.edu/projects/AOMIP/>) protocol and treated like a surface volume flux. Open boundaries are formulated following Stevens (1990) and are located at 50°N in the Atlantic and just south of the Bering Strait. Temperature and salinity at the open boundaries are taken from the PHC climatology. The Bering Strait inflow is prescribed to 0.8 Sv. The stream function at the open boundary in the Atlantic Ocean is corrected at the end of the run for the sea surface height fluctuations in the model domain and the model is re-run with the new stream function.

In this study we are comparing two identical experiments with the only difference being the P^* parameter of the sea ice model rheology:

- control run (CTRL): $P^*=27.500$ N/m² (the value estimated by Hibler and Walsh (1982))
- low P^* run (WEAK): $P^*=15.000$ N/m² (the value estimated by Kreyscher et al (2000b))

For our study we have used one of the longest atmospheric reanalysis available (60 years, 1948-2007) so that the differences between the runs in the sensitivity study can fully develop. The first 20 years of the simulations (1948-1967) are considered to be influenced by adjustment processes in the ocean and are excluded from the calculation of temporal means for the analysis, but are still shown in the time series to track the development of the differences between the runs.

The statistical significance of the sensitivity experiment has been assessed for all the time series and maps which show the difference between the two experiments. We have de-trended the time series to calculate the standard deviation of the CTRL to test if the time series of the WEAK lay within one standard deviation envelope. To test if the mean of the difference between the runs is different from zero we employed a t-test for paired differences of dependent samples (Wilks, 1995; Von Storch and Zwiers, 2001):

$$t = \frac{\bar{\mu}_D}{S_D/\sqrt{n}}, \quad (3.2)$$

where μ_D is the mean difference, S_D^2 is the variance of the differences between the CTRL and WEAK and n is the size of the sample of differences. We have compared the obtained t value to the critical value for the significance at 2% confidence level for a two-sided test.

3.3 Comparison to observations

To demonstrate that our model simulation is able to capture the relevant observations, we perform a comparison of CTRL to observational data. We focus on comparing the sea ice results, since the thin layer of sea ice is sensitive to the changes in both layers that it divides, ocean and atmosphere and is as such

an indicator of the coupled system performance. Since the beginning of the satellite remote sensing era the sea ice observations have become widely available and here we can address the sea ice concentration, sea ice thickness, sea ice volume and sea ice drift. For the mid-depth ocean fewer long time series are available and we compare the temperature time series at the Fram Strait and Barents Sea Opening and the circulation of the water masses in the model domain.

The sea ice concentration data for the model validation are obtained from EUMETSAT Ocean and Sea Ice Satellite Application Facility (OSI-SAF): Global sea ice concentration reprocessing dataset (OSI-SAF, 2013). The accuracy of the OSI-SAF sea ice concentration during the winter is estimated to 5-10% (in the MIZ up to 12%) and to up to 20% during the summer. The model tends to overestimate the sea ice extent in the Marginal Ice Zone (MIZ) throughout the year; it also overestimates the summer sea ice concentration on the Arctic Shelf, and underestimates it in the Central Arctic (Fig. 3.2).

We compare the model sea ice thickness to the ICESat (Ice, Cloud, and land Elevation Satellite) sea ice thickness maps (Zwally et al, 2002). The ICESat maps are only available for the central Arctic where the sea ice thickness is greater than 1 m. For 2007, which is the last year of our model run the maps are available for the February/March and October/November (Fig. 3.3, panels a and c). The comparison shows that our model captures the general sea ice distribution pattern (Fig. 3.3, panels b and d), but has too much ice in the Canadian Basin and too little in the area directly adjacent to the Canadian Archipelago and Northern coast of Greenland, both in winter and in fall. The large uncertainty of the ICESat sea ice thickness (0.7 m) (Kwok and Cunningham, 2008) prevents a more detailed comparison.

The time series of the sea ice volume data are obtained from the Pan-Arctic Ice-Ocean Modeling and Assimilation System (PIOMAS) version 2.1 (Schweiger et al, 2011). PIOMAS is a sea ice ocean coupled model with assimilated sea ice concentration observations and sea surface temperatures in the ice free regions. Since the large spatial and temporal coverage of the sea ice thickness data is not available, PIOMAS sea ice volume is a commonly used dataset used to estimate the performance of the models that do not assimilate any observational data. The time series of the Arctic sea ice volume on Fig. 3.3, panel e show that our model captures very well the sea ice volume decline of the recent decades. Our model simulations have higher sea ice volume as the PIOMAS, despite the fact that our model domain does not extend to the North Pacific which is

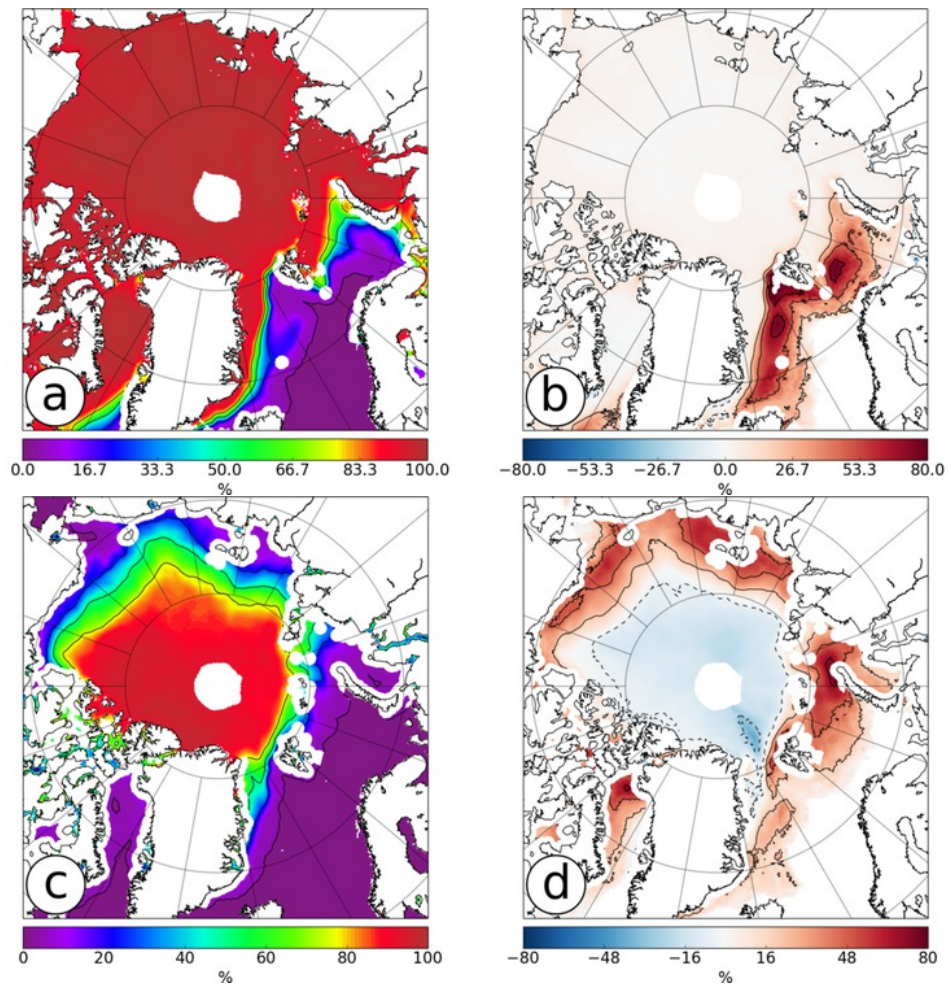


Figure 3.2: March (a,b) and September (c,d) mean (1988-2007) sea ice concentration observations by OSI-SAF and the differences model minus OSI-SAF. On b and d: blue color means model is underestimating sea ice concentration, red color means model is overestimating sea ice concentration.

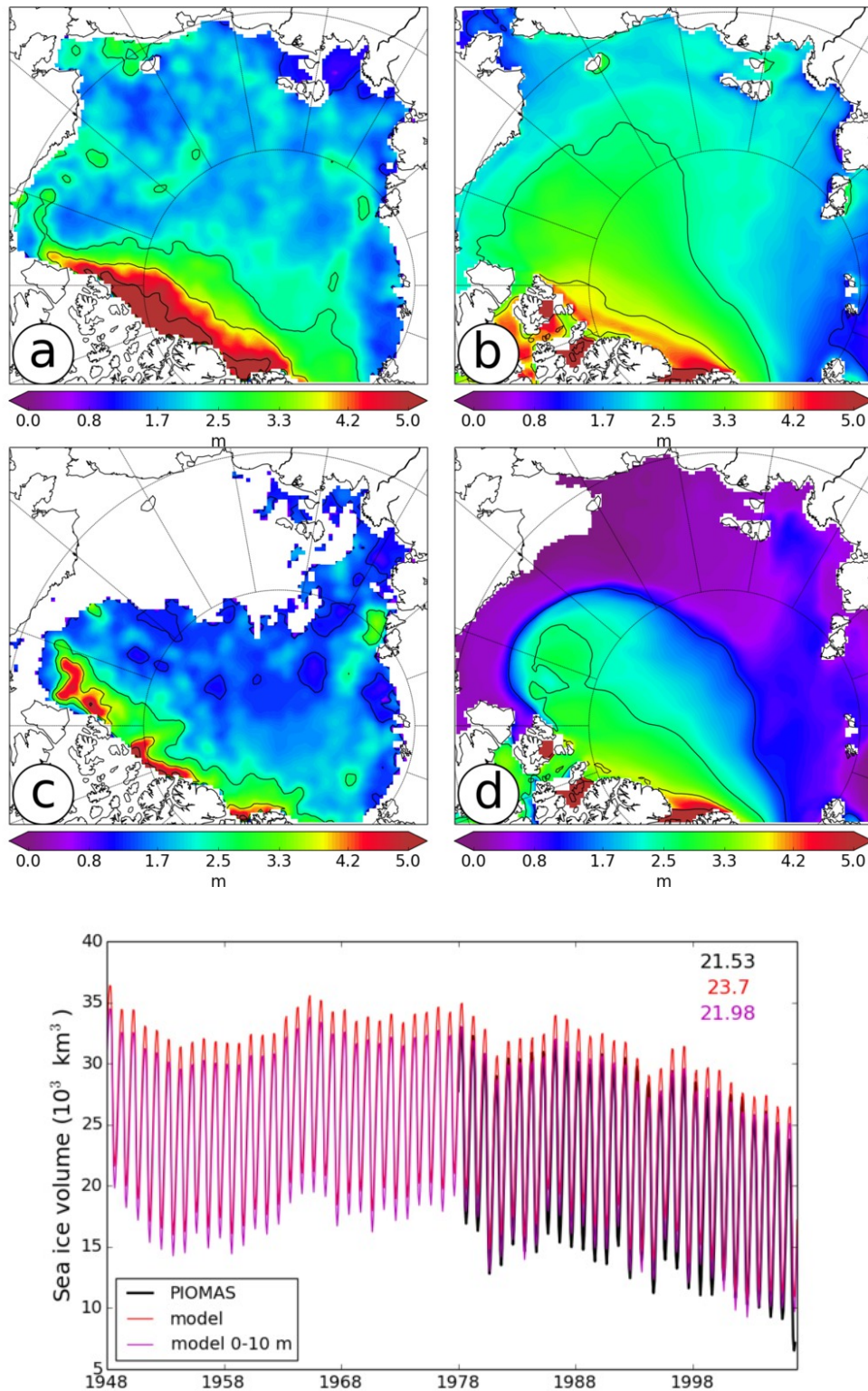


Figure 3.3: Sea ice thickness comparison: a - ICESat February/March 2007, b - CTRL February/March 2007, c - ICESat October/November 2007, d - CTRL October/November 2007, e - Monthly sea ice volume for CTRL, for CTRL with the sea ice thickness capped at 10 m (model 10 m) and for the PIOMAS model. The temporal means are printed in the colors corresponding to the legend.

the case for the PIOMAS. The reason for this overestimation is the very thick ice that accumulates in our model in the straits of the Canadian Archipelago. Similarly to our model, PIOMAS has problems reproducing thick sea ice along the Canadian and Greenland coast (Schweiger et al, 2011). If we limit the sea ice thickness used in the sea ice volume calculation to the maximum of 10 m, our simulations get even closer to the PIOMAS dataset.

We have compared the sea ice drift of our model to the monthly satellite remote sensing products provided by the National Snow and Ice Data Center (NSIDC) (Fowler et al, 2013) and Centre ERS d'Archivage et de Traitement (CERSAT) (Girard-Arduin and Ezraty, 2012). We are using two datasets as it has been pointed out before e.g. by Martin and Gerdes (2007) and recently by Sumata et al (submitted to the JGR) that the ice drift products might differ substantially. The histograms of March and September sea ice drift speed show that our model is biased towards high drift speeds (Fig. 3.4). The differences between the model and the satellite drift products are in places smaller than the differences between the NSIDC and CERSAT products which underlines the high uncertainties in the sea ice drift observations.

Hydrographic data for the Kola section (1958-2007) are from the Knipovich Polar Research Institute of Marine Fisheries and Oceanography (PINRO, <http://www.pinro.ru>). The section comprising 4 CTD stations is located in the Murman Current along 33°30'E between 71°N and 73°N. The data is averaged over 0 to 200 m depth. While our simulation has a low temperature bias of about 1 °C (Fig. 3.5, panel a), the linear correlation between the model and observations is high, 0.8 and significant at 1% confidence level.

To compare the simulated temperature of the Fram Strait inflow we have chosen a region in the West Spitzbergen Current (WSC) between 78°30' - 79°12'N and 5° - 9°E. We used hydrographic data from the World Ocean Database 2009 (<http://www.nodc.noaa.gov/OC5/WOD>), HydroBase3 (<http://www.whoi.edu/science/P0/hydrobase>) and from cruises of the Alfred Wegener Institute and the Norwegian Polar Institute (Schauer et al, 2008; Hughes and Holliday, 2006) from 1956 to 2007. For each station, the vertical mean of 50-500 m was obtained after interpolating temperature linearly to fixed depths in 10 m steps. Station means were averaged over each summer (May to October). By choosing a large depth interval we captured the whole WSC core in the observations and in our model. Panel b on Fig. 3.5 shows that despite the low linear correlation between the model and observations, 0.28, the modeled values lie inside the error bars of the observations and depict a warm phase in

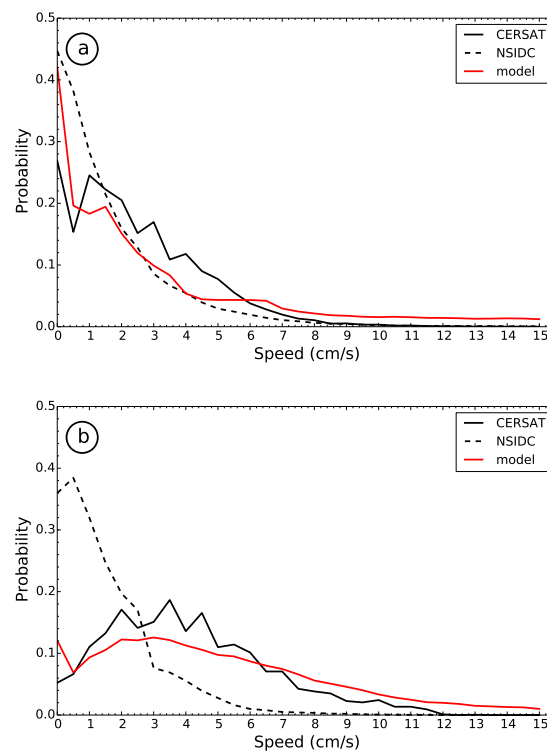


Figure 3.4: Histograms of March (a) and September (b) sea ice drift speed for period 1992-2007 for the satellite remote sensing products (CERSAT and NSIDC) and our model. Bin width is 0.5, beginning at 0.5 cm/s.

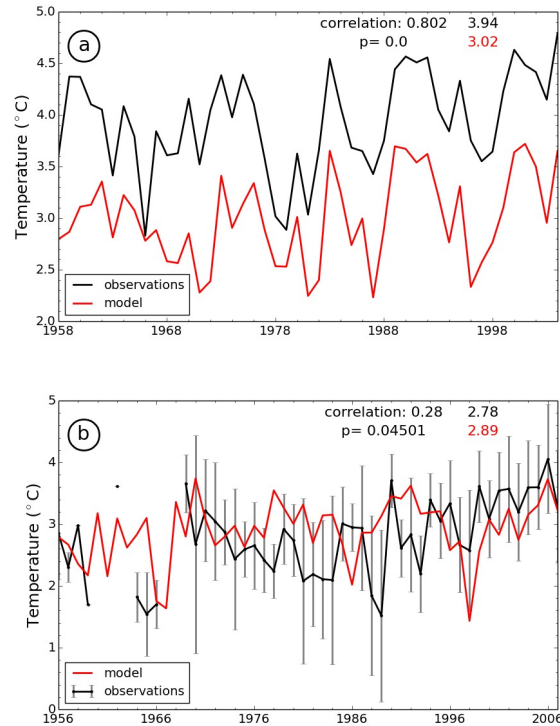


Figure 3.5: a: Vertical mean 0-200 m annual temperature at the Kola section in the central Barents Sea. b: Vertical mean 50-500 m summer temperature in the WSC. Error bars on the observational time series denote one standard deviation. No error is provided for years with less than five measurements. No error information is provided to the Kola section. The temporal means from 1958 to 2007 are printed in the colors corresponding to the legend.

the 1990s, followed by a cool phase and the strong warming period in recent years.

The AWL circulation in our model (arrows on Fig. 3.8, panel a) is closely following pathways described by Rudels et al (1994). The warm mid-depth water is entering the Arctic Ocean from the Nordic Seas through the Fram Strait and Barents Sea Opening. Part of it circumnavigates the Eurasian Basin and exits again on the western side of the Fram Strait, while the other part flows over the Lomonosov Ridge into the Amerasian Basin where it follows the topographical features of the shelf break (e.g. Chukchi Cap) flows north of the Canadian Archipelago and Greenland and exits in the Fram Strait.

Despite a bias in the sea ice extent and the Kola temperature time series the overall model performance is reasonable. Some of the biases in the simulation can be attributed to the biases in the atmospheric forcing as demonstrated by

e.g. Hunke and Holland (2007) and Lindsay et al (2014).

3.4 Sea ice and ocean surface

Figs. 3.6 and 3.7 show the differences between the CTRL and the WEAK experiment. All maps are March means (1968-2007) as the differences in sea ice winter extent and thickness are largest for the performed runs. Differences based on the annual means are similar to the winter patterns (not shown). The value of P^* determines P and reducing P^* almost by half has a similar effect on P (Fig. 3.6, panels a and b) despite an increase of the sea ice thickness (Fig. 3.7, panels a and b). Fig. 3.6, panels c and d show the mean sea ice motion in CTRL and WEAK minus CTRL. In WEAK the anticyclonic motion of the sea ice in Beaufort Gyre is enhanced in comparison to CTRL, whereas the Transpolar Drift is slower. Overall, the ocean surface stress, calculated as sum of the wind stress and internal ice stress (Losch et al, 2010) is higher in WEAK (color shading of the same panels). The highest ocean surface stresses occur in the ice free ocean and in the East Greenland Current, where sea ice is the most mobile. However, the highest relative differences between the experiments (calculated as ocean stress difference between the WEAK and CTRL normalized by local mean ocean stress in CTRL) occur in the relatively slow ice of the central Arctic.

Lower P^* in WEAK increases the compressibility of the sea ice and through the differences in the sea ice motion this is reflected also in the sea ice thickness (Fig. 3.7, panels a and b) and concentration (Fig. 3.7, panels c and d). Due to enhanced converging motion of sea ice and consequently sea ice thickening we find in WEAK thick ice accumulation in the Beaufort Gyre, along the Canadian Archipelago and along the Greenland coast. Some smaller areas of increased thickness are seen north of Bering Strait and around Svalbard and Severnaya Zemlya. The MIZ in WEAK has lower sea ice concentration related to reduced sea ice export from the Arctic to the northern Nordic Seas and the Barents Sea (not shown). This pattern is reflected in the surface heat flux differences of WEAK minus CTRL (Fig. 3.7, panels e and f). Locally in the MIZ the differences amount up to 40 W/m^2 .

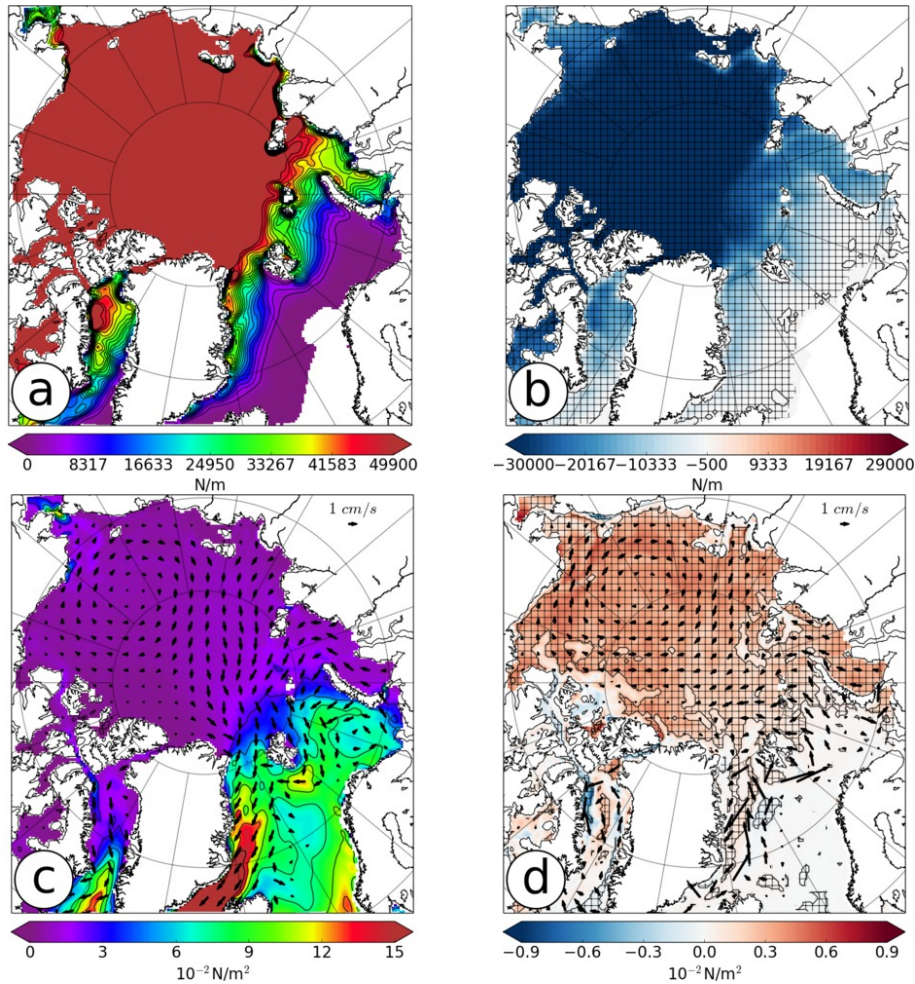


Figure 3.6: Sea ice and ocean surface properties: left - CTRL, right - WEAK minus CTRL: a,b: compressive sea ice strength (P); c,d: ocean surface stress magnitude (color) sea ice drift (vectors - only every 5th vector is shown, on panel a velocities are capped at 1 cm/s for better comprehension). All variables are March means for the period from 1968 to 2007. Hatched polygons cover the areas where the differences between WEAK and CTRL are significant at 2% confidence level for a two-sided test.

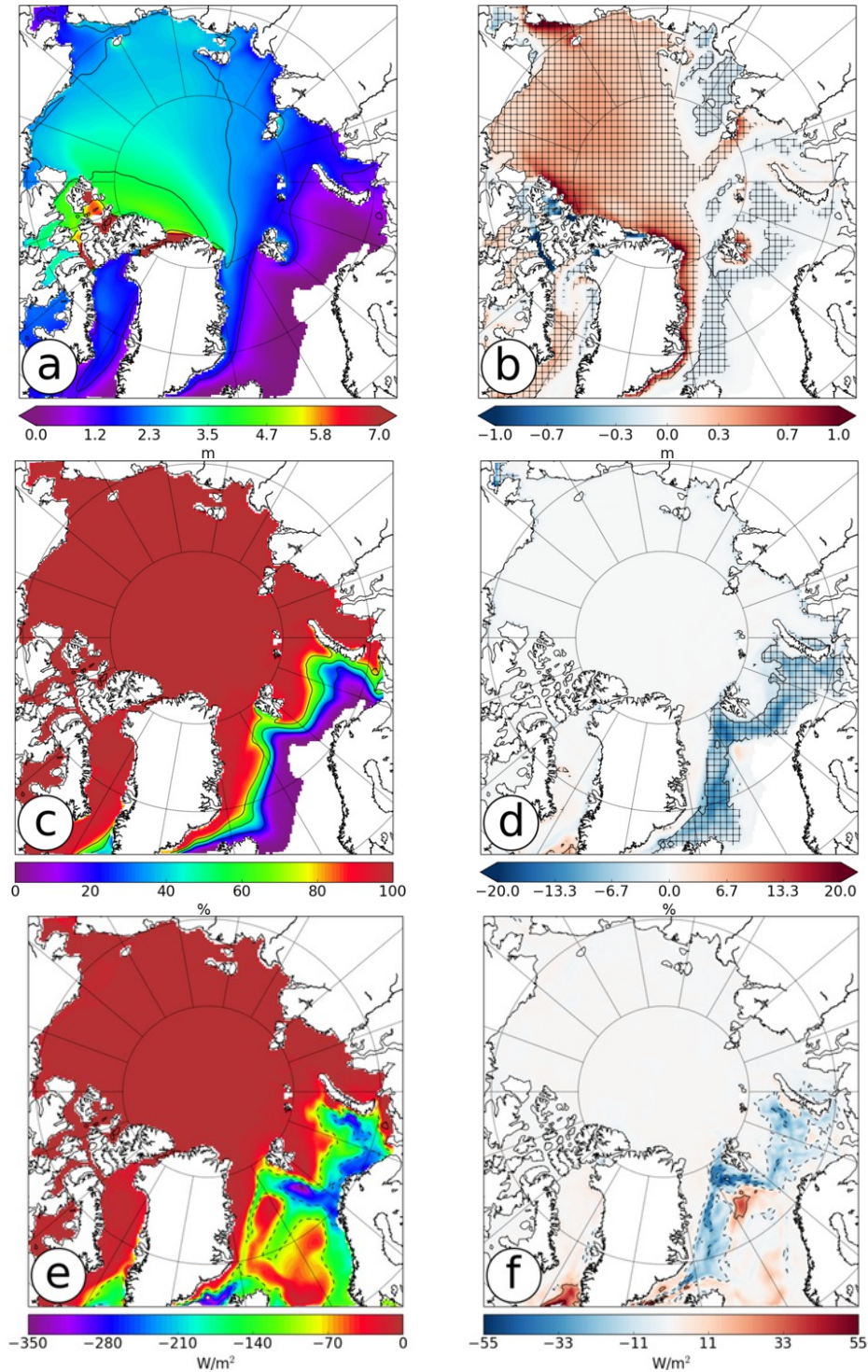


Figure 3.7: Sea ice and ocean surface properties: left - CTRL, right - WEAK minus CTRL: a,b: sea ice thickness; c,d: sea ice concentration; e,f: surface heat fluxes. The hatched polygon covers the area where the differences between WEAK and CTRL are significant at 2% confidence level for a two-sided test.

3.5 Mid-depth ocean

Turning to the differences in the AWL (212 - 1200 m) we find all Arctic basins to be considerably cooler in the case of WEAK (Fig. 3.8). The differences are especially large in the Eurasian Basin, but the signal spreads also into the Amerasian Basin. In WEAK also the temperatures in the boundary current in the Nordic Seas are much lower. Compared to the AWL circulation in CTRL the circulation in the Eurasian Basin is enhanced and in the Amerasian Basin the dominant flow is across the basin from the Lomonosov ridge towards the Alaskan Coast. The cyclonic gyre of the AWL in the Amerasian Basin is pushed away from the Eurasian shelfbreak, reduced in size, but enhanced in velocity. Additionally a small anticyclonic gyre develops in the Amerasian Basin between Chukchi Cap and the Lomonosov Ridge. The gyre is reaching to the bottom of the AWL (not shown) and is returning the water mass back to the Eurasian Basin (visible also as vectors on Fig. 3.8, panels b and e).

The temporal development of the AWL temperatures reveals that the differences between WEAK and CTRL develop already in the first years of the simulations (Fig. 3.9). During the first year differences occur in the Nordic Seas, mostly in the MIZ, and in the Barents Sea. During the second year the differences are visible in the outflow through St. Anna Trough, while in the Nordic Seas recirculation and propagation of the cold signal southward beyond the Denmark Strait becomes apparent. During the third year the difference signal has traveled around the whole cyclonic gyre in the Nordic Seas and reached the bifurcation point of the Norwegian Current to the BSB and FSB north of the Scandinavian Peninsula. The propagation of the negative (cold) signal is not uniform and also positive differences occur locally. Fig. 3.9, panels a and b show that the signal reaches the Eurasian Basin partly through Fram Strait and partly through the St. Anna Trough while a minor part reaches the basin through the strait between Svalbard and Franz-Josef Land. Integrated over the entire basins a cooling trend is apparent in both basins, though significantly more pronounced, and with an earlier onset in the Eurasian basin as compared to the Amerasian Basin (Fig. 3.10, panel a). The cooling that develops off the Barents Sea shelf and in the Nordic Seas spreads with the cyclonic circulation of the AWL throughout the Eurasian Basin. After 4 to 5 years the time series of temperature north of Severnaya Zemlya (downs. SAT on Fig. 3.10 panel b) show the arrival of a strong cooling. The signal recirculates along the Siberian shelf slope and the Lomonosov Ridge and reaches the area upstream of Fram Strait 15 years into the simulation (ups. FS Fig. 3.10, panel b). The temperatures in the Fram

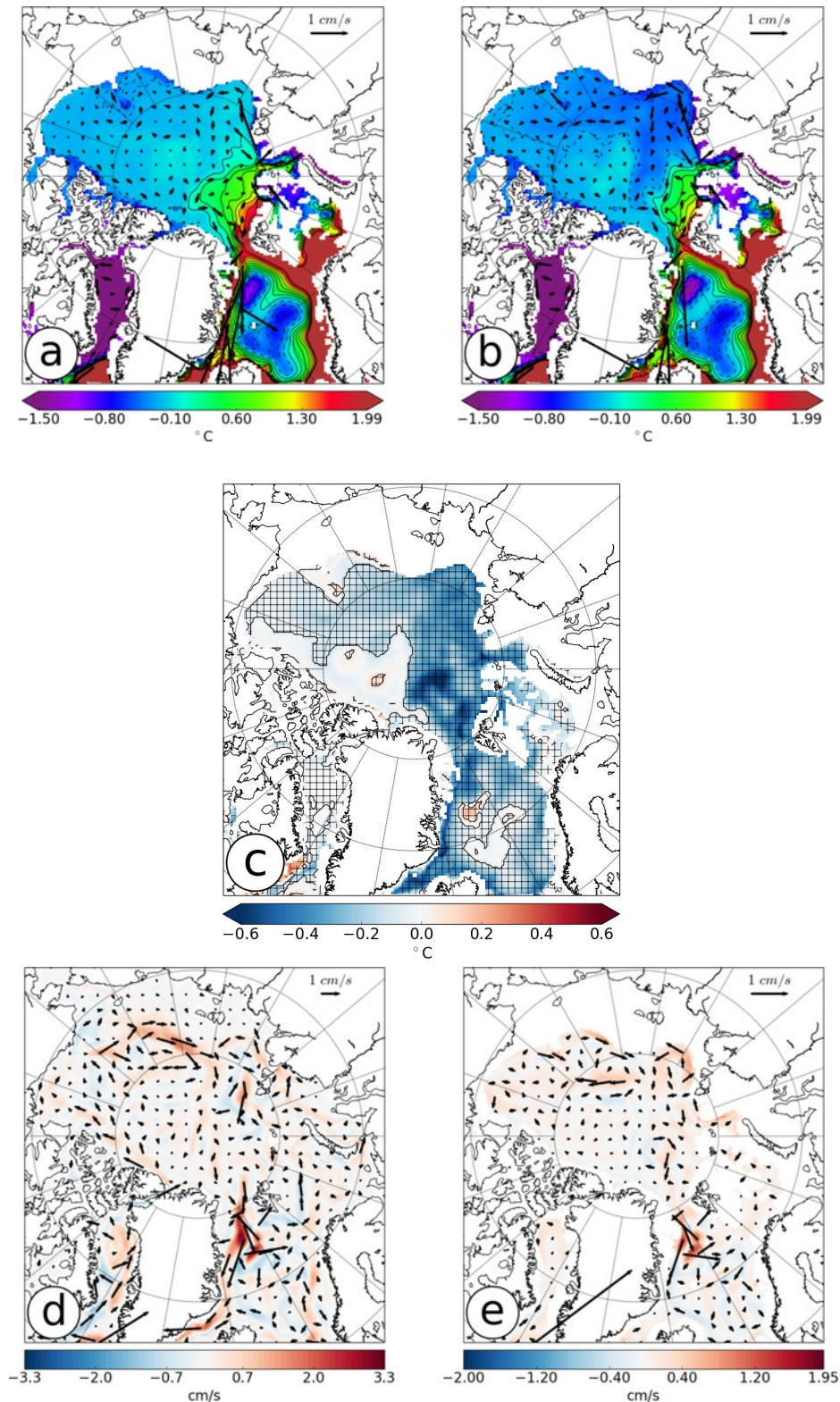


Figure 3.8: Temperature and velocity means (1968-2007) in the AWL (212 - 1200 m): a - CTRL, b - WEAK, c - WEAK minus CTRL. Hatched polygons cover the areas where the differences between WEAK and CTRL are significant at 2% confidence level for a two-sided test. Speed mean (1948-2007) difference between WEAK and CTRL in the: d - surface (0-50 m), e - AWL (212-1200 m). Velocities are represented by vectors. Only every 5th vector is shown. To enhance comprehension of the maps only velocities in areas with the surface layer and AWL thicker than 50 m are shown.

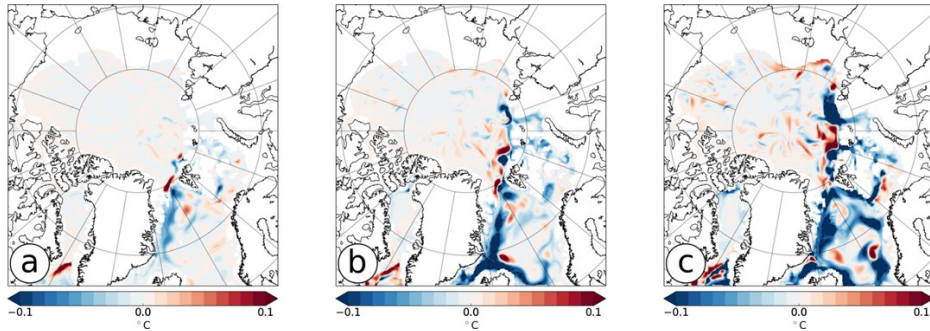


Figure 3.9: Development of the AWL (212 - 1200 m) temperature differences WEAK minus CTRL in during: a - first, b - second and c - third year of the simulations.

Strait outflow (FS outflow on Fig. 3.10, panel c) remain predominately cooler after 20 years into the simulation. The temperatures in the St. Anna Trough inflow (SAT inflow on Fig. 3.10, panel c) become cooler in WEAK already during the first years of the simulation. The temperatures in the Fram Strait inflow (FS inflow on Fig. 3.10, panel c) are fluctuating and no stable offset in temperature between WEAK and CTRL occurs, but after about 10 years into the simulation the inflow is mostly colder in the case of WEAK, likely enhanced by the recirculation of the colder temperature signal in the Nordic Seas. The WEAK time series of temperature in the Eurasian and Amerasian Basin are outside of the one standard deviation envelope around the CTRL time series. For all of the time series, the mean difference of the means between the WEAK and CTRL is significant at the 2% confidence level.

Mean (1968-2007) temperature sections at the St. Anna Trough and the Fram Strait (Fig. 3.11) show that at both gateways water masses are cooler in WEAK, with the exception of the uppermost layers in the Fram Strait. In the St. Anna Trough the AW core which originates from the FSB partially enters the trough on the western slope, recirculates and exits on the eastern side together with the BSB. In the case of WEAK, the cooler FSB thus contributes to the cooler AW leaving St. Anna Trough to feed into the AWL.

The changes in the FSB and BSB temperatures are connected also to the change in the volume fluxes across the Arctic Straits (Fig. 3.12). WEAK has stronger net Barents Sea Opening inflow (by 0.19 Sv), stronger net Fram Strait outflow (by 0.46 Sv) and weaker net Davis Strait outflow (by 0.28 Sv) comparing to CTRL. The mean difference of the mean volume fluxes is significant at the 2% confidence level.

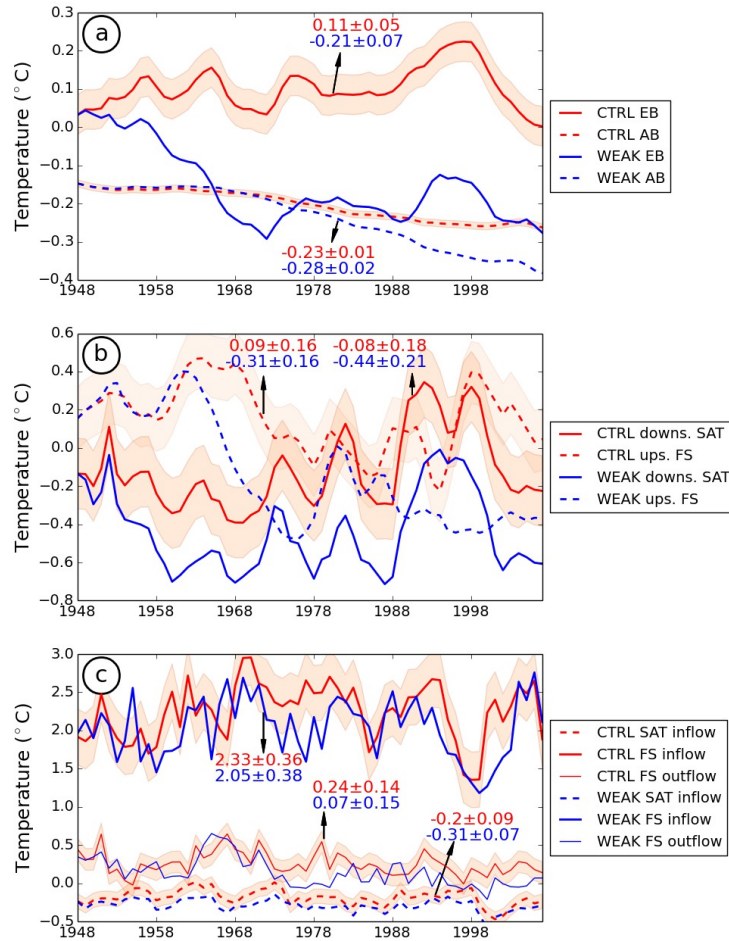


Figure 3.10: Development of the AWL (212 - 1200 m) temperatures: a - time series of vertically averaged temperature for the AWL in the Eurasian (EB) and Amerasian Basin (AB), b - for the box area in the Eurasian Basin downstream the St. Anna Trough (downs. SAT) and box area in the Eurasian Basin upstream the Fram Strait (ups. FS), c - for the upper AWL (212 - 700 m) inflow to the Arctic Ocean at the St. Anna Trough (SAT inflow) and Fram Strait (FS inflow) and lower AWL (700 - 1200 m) outflow at the Fram Strait (FS outflow), f - for the box area in the Eurasian Basin downstream the St. Anna Trough (downs. SAT) and box area in the Eurasian Basin upstream the Fram Strait (ups. FS). The 1968-2007 means and standard deviations are printed in the colors corresponding to the legend.

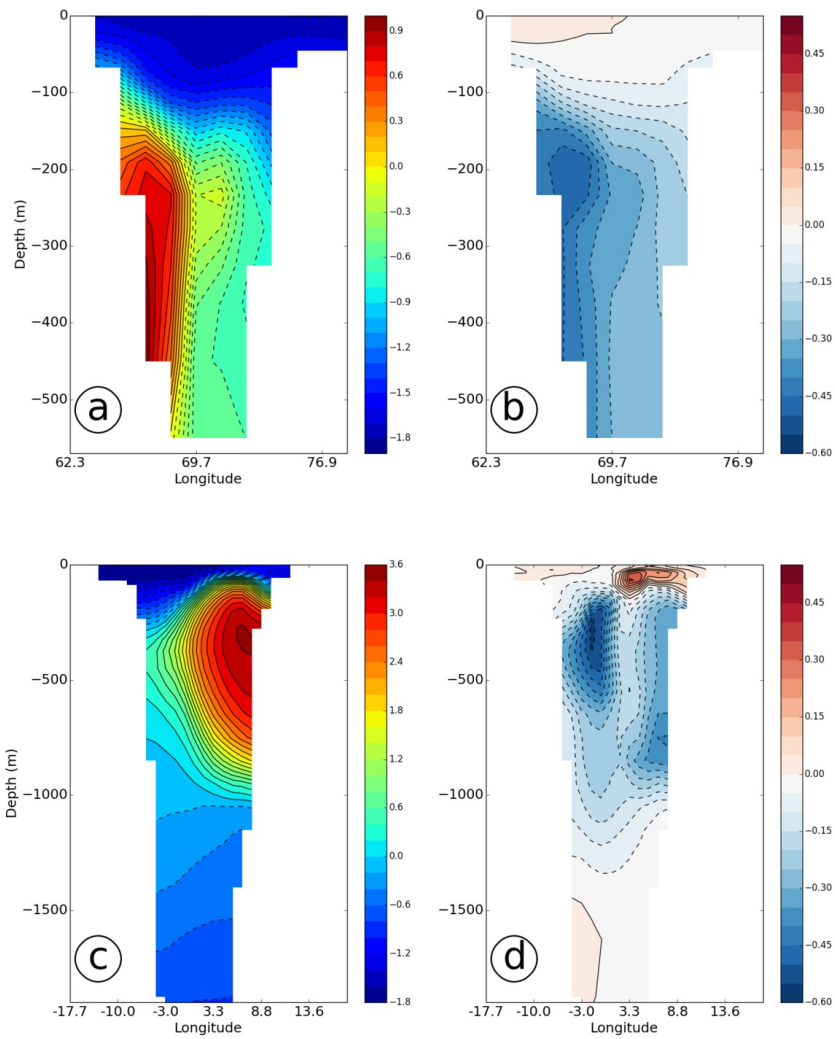


Figure 3.11: Mean temperature (1968-2007) sections at the key regions: St. Anna Trough and Fram Strait: CTRL (a,c) and WEAK minus CTRL (b,d). Both sections are oriented zonally and reader looking into the page is facing northwards.

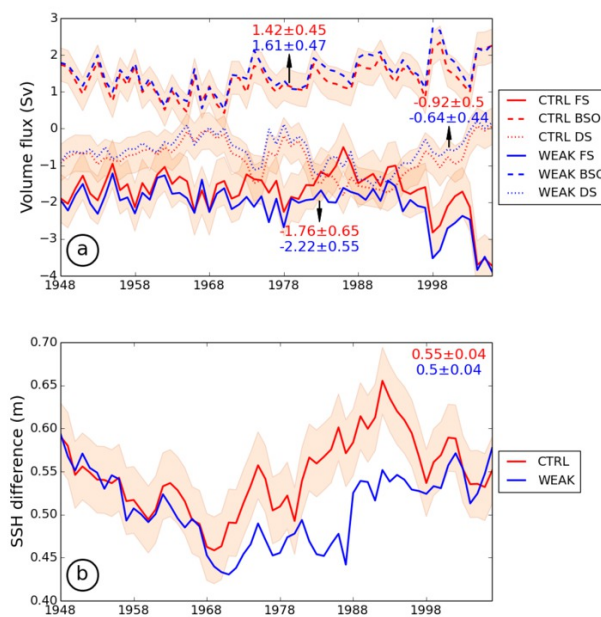


Figure 3.12: Time series of the net volume fluxes at the major Arctic Straits: Fram Strait (FS), Barents Sea Opening (BSO), Davis Strait (DS). c - sea surface height difference between the Arctic Ocean north of the Canadian Archipelago and the Labrador Sea. The temporal means and standard deviations 1968-2007 are printed in the color corresponding to the legend.

3.6 Connecting the sea ice and mid-depth ocean

In the Barents Sea and in the northern Nordic Seas WEAK has lower sea ice concentration than CTRL. Large areas of the ocean exposed directly to the atmosphere in the Barents Sea lead to a high heat loss at the ocean surface and to strong cooling of the AW that sinks to the bottom and forms the dense part of the BSB (Fig. 3.13, panels a, b and c). Although the areal and temporal mean difference between CTRL and WEAK in surface heat fluxes in the Barents Sea is only 2.8 W/m^2 (Fig. 3.13, panel b), this alone can lead to a substantial difference in the bottom water temperature. Calculating the total amount of heat Q for a mean year and grid box area and inserting it to formula $Q = c_p * m * \Delta T$ (where m is mass, $c_p = 3994 \text{ J/kg/K}$ is heat capacity), will in a 200 m deep water column yield in a temperature change ΔT of 0.1 K. This matches the mean temperature difference between WEAK and CTRL in the St. Anna Trough inflow into the Eurasian Basin (SAT inflow on Fig. 3.10, panel c).

While the net surface outflow (0-170 m) from the Barents Sea into the Eurasian Basin through the section between Svalbard and Severnaya Zemlya is very similar in both runs, the net deep outflow (170-212 m) is increases in WEAK with respect to CTRL and indicates a stronger dense water production on the Barents Sea shelf (SSZ surface and SSZ bottom on Fig. 3.13, panel d). At the same time, Barents Sea Opening volume fluxes (BSO inflow on Fig.3.13 panel d) show a stronger net inflow into the Barents Sea. The mean difference of the means is significant at the 2% confidence level, except for the net surface inflow between Svalbard and Severnaya Zemlya. The relation of stronger BSB formation and lower sea ice extent in the Barents Sea has been pointed out already in a sensitivity study by Harms et al (2005).

The FSB in WEAK is cooled by enhanced surface heat loss in the northern Nordic Seas, just as the BSB is conditioned in the Barents Seas. The cooling in the northern Nordic Seas in case of WEAK is apparent down to the deep part of the Fram Strait inflow (700-1200 m). This is a consequence of cooling of the whole boundary current in Nordic Seas (Fig. 3.9, panels a, b and c) and the recirculation of the colder water in the Nordic Seas. When the colder water mass recirculates towards the bifurcation in the Norwegian current lead to an additional decrease in temperature. We interpret the intensified cooling in the deep WSC starting about 20 years into the simulation as consequence of the arrival of colder water from the BSB reaching the Fram Strait as a part of the AIW. The maximum in temperature difference between WEAK and CTRL in

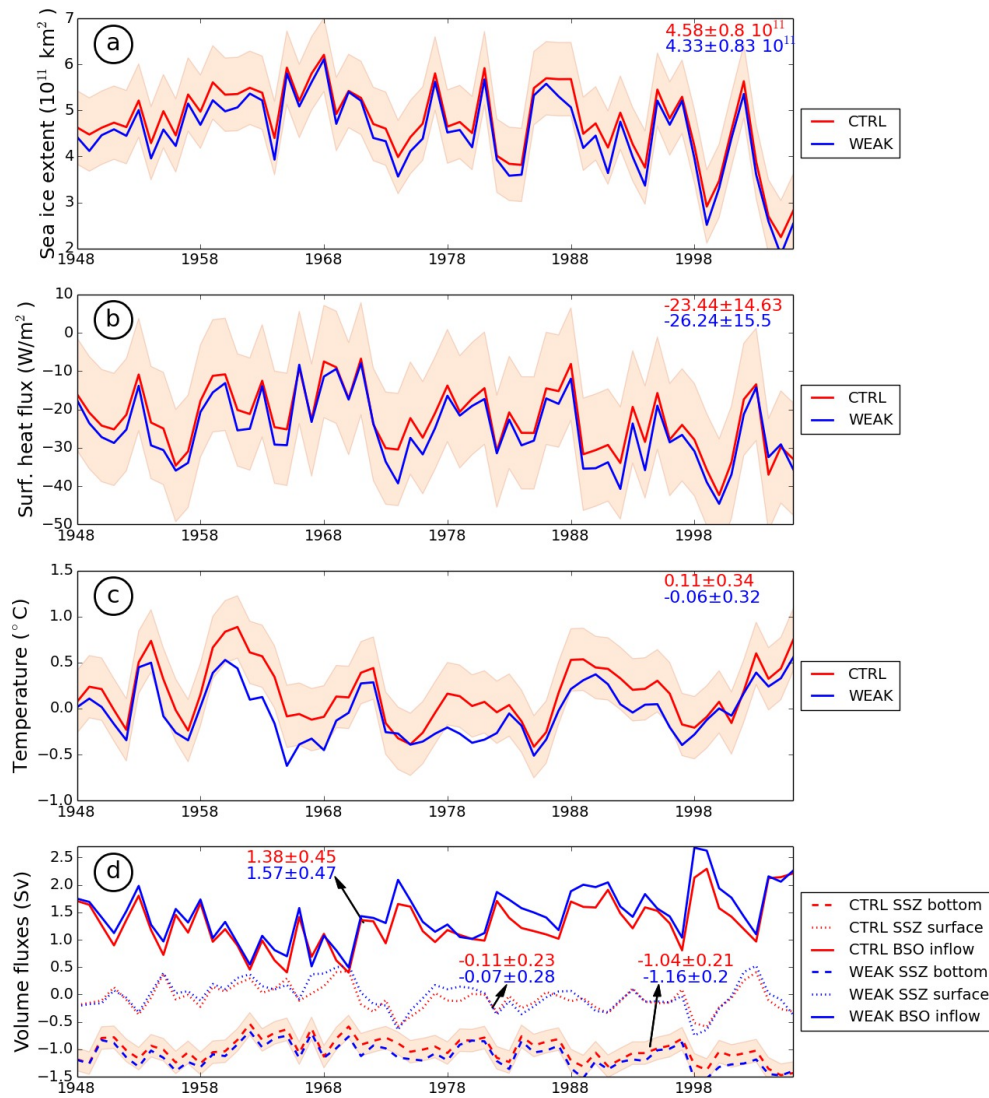


Figure 3.13: Time series of the annual mean sea ice and ocean variables for the Barents Sea: a - sea ice extent, b - surface heat flux, c - bottom (170-212 m) water temperature, d - net bottom (170 m - bottom) volume outflow into the Arctic between Svalbard and Severnaya Zemlya (SSZ deep), net surface (0 - 170 m) volume outflow into the Arctic between Svalbard and Severnaya Zemlya (SSZ surface) and Barents Sea Opening net inflow into the Barents Sea (BSO inflow). The temporal means and standard deviations 1968-2007 are printed in the colors corresponding to the legend.

the WSC in the Fram Strait is at the lower AWL depth (Fig. 3.11, panel d). Finally the temperature difference between CTRL and WEAK in the Eurasian Basin stabilize by 0.2 K.

The AWL circulation is not only governed by the inflow at the Arctic gateways, but also by local processes in the central Arctic, e.g. by surface stresses imposed by the combination of wind stress and sea ice motion. In WEAK the faster sea ice drift in the anticyclonic Beaufort Gyre (Fig. 3.6, panel d) leads to an intensification of the oceanic Beaufort Gyre (Fig. 3.8, panel e). Yang (2009) observed a faster sea ice motion and a gradual intensification of the Beaufort Gyre in the 1977-2006 that could not be attributed to the changes in the wind stress, but rather to the changes in the sea ice dynamical properties. The intensification of the Beaufort Gyre is accompanied with a steepening of the slope in the halocline and as a consequence of Ekman pumping also a deepening of the halocline (see e.g. Rabe et al (2011) and Karcher et al (2012)). This leads to a hampering of the underlying cyclonic circulation of the AW boundary current. A similar process has been described by Karcher et al (2012). They found that a strong anticyclonic Beaufort Gyre in the Amerasian Basin after 2004 led to a reduction and partial stopping of AW inflow from the Eurasian Basin into the Amerasian Basin. Instead, an intensification of the recirculation of AW in the Eurasian Basin along the interior ridges took place. A similar situation appears in our study where a part of the AW entering Amerasian Basin from the Eurasian Basin is returned due to a small anticyclonic gyre that develops in the Amerasian Basin between Chukchi Cap and the Lomonosov Ridge (Fig. 3.8, panel e). Also here the loop of the AWL in the Eurasian Basin is enhanced and leads to an intense BSB core marked by cool temperatures looping along the Eurasian Basin side of the Lomonosov Ridge towards the Fram Strait. We suggest that the arrival of this plume about 20 years into the simulation (Fig. 3.10, panel c) triggers an adjustment in the fluxes through Fram Strait, together with the recirculation signals in the Nordic Seas. Thus, the net volume fluxes through both entrances to the Arctic, Fram Strait and the Barents Sea Opening change and necessarily lead to an adjustment of the volume fluxes through Davis Strait. The decrease of the Davis Strait outflow follows the increase in the East and then West Greenland Current fluxes originating from the Fram Strait outflow and the resulting sea surface rise in the Labrador Sea (Fig. 3.12, panel b), as described by McGeehan and Maslowski (2012). The mean sea surface height difference between WEAK and CTRL is significant at 2% confidence level. The difference is high in the 3 decades between 1968 and 1998 which matches the timing of enhanced differences in the volume fluxes

between the straights (Fig. 3.12, panel a).

3.7 Summary and conclusions

We have presented a study in which we reduce the sea ice strength parameter P^* , commonly used as a tuning parameter in sea-ice models, to investigate the sensitivity of the ocean circulation to this change. As a result, we find a number of modifications of the Arctic Ocean circulation from the surface down to lower AWL depths. Primary results of the imposed reduction of ice strength is a lower sea ice concentration in the MIZ and more mobile sea ice in the central Arctic. This leads to an enhanced surface heat loss in the MIZ, stronger dense water formation that contributes to colder and more abundant BSB that cascades down the St. Anna Trough and is fed by an intensified inflow from the Barents Sea Opening. The FSB in the WSC, which is warmer than the BSB, is also experiencing enhanced surface heat loss in the MIZ. This leads to a cooling of the Eurasian Basin of about 0.2 K. In addition, cooling of the mid-depth Nordic Seas along the entire basin's margin, including the Denmark Strait sill region, takes place. This is a consequence of an intensified heat loss in the Nordic Seas MIZ in addition to a colder BSB which, after recirculation in the Arctic Ocean, reaches Fram Strait as a part of the AIW. The loop closes when after recirculation inside the Nordic Seas, the part of the cooling signal which moves into the WSC enters the Arctic Ocean and is another contributor to the cooler AWL there.

In the Arctic Ocean the reduced sea ice strength leads to a more mobile sea ice in the central Arctic which in turn leads to an enhancement of the anticyclonic Beaufort Gyre circulation of the sea ice and the upper ocean. The latter suppresses the cyclonic AW circulation in the Amerasian Basin and reduces the flow of the AW boundary current beyond the Lomonosov Ridge. Instead the shorter loop of the AW in the Eurasian Basin enhances. Changes also apply for the volumetric balance between the Arctic straits. In the case of the weaker sea ice stronger net inflow (by 0.19 Sv) in the Barents Sea takes place in conjunction with stronger net outflow (by 0.46 Sv) in the Fram Strait and weaker net outflow (by 0.28 Sv) in the Davis Strait. The transport in Fram Strait adjusts to the propagation of the cooling in the FSB and the BSB and leads to further adjustments in the Davis Strait transports when the anomalies propagating in the West Greenland Current reach the Labrador Sea and rise the local sea surface height. Using an atmosphere-ice-ocean coupled model Wu

et al (2006) and Rinke et al (2013) demonstrated a connection of the Barents Sea sea ice cover reduction to the Beaufort Sea atmospheric circulation, while in the present study sea ice concentration in the Barents Sea and ice-ocean circulation in the Beaufort Gyre are triggered solely by changes in the P^* .

In addition to the local changes in the circulation and hydrography in the Arctic Ocean as a consequence of changes in ice strength, we found changes in the mid depth AIW exiting the Arctic Ocean in the Fram Strait and changes in the southward boundary current in the Nordic Seas from Fram Strait to the Denmark Strait. These may have an impact on the Atlantic Meridional Overturning Circulation (AMOC) since they directly feed into overflows over the Greenland-Scotland sills. The discovered change in the ratio of the Fram and Davis Strait volume transports might result in a change of the water mass characteristics in the deep water formation areas in the Labrador Sea that also feed the AMOC.

These significant changes in the mid-depth ocean temperature and volume fluxes show that those model optimization exercises in which P^* is used to improve ice extent and thickness simulations should be done with care and with an assessment of the imposed changes in the ocean properties.

We also believe that from this study we can learn about possible consequences of a weakening of the sea ice strength, as an element of ongoing reductions in the Arctic sea ice cover (Stroeve et al, 2012) and acceleration in speed (Rampal et al, 2009; Spreen et al, 2011). Our experiments suggest that the decrease of the sea ice cover in the MIZ has a potential to milden the observed AW inflow warming (Polyakov et al, 2010; Beszczynska-Möller et al, 2012).

Acknowledgments

We would like to thank Wilken-Jon von Appen and Karel Castro Morales, both Alfred Wegener Institute (AWI) for the help with the observational data comparison. We are grateful to Karel, Martin Losch and Kathrin Riemann-Campe, also AWI who have contributed to the model development. Frank Kauker, AWI has advised us with the statistical analysis of the results. Polona Itkin's PhD studies have been partially supported by a grant of the Municipality of Ljubljana, Slovenia. Michael Karcher and Rüdiger Gerdes acknowledge support from the project 'RACE - Regional Atlantic Circulation and Global Change' funded by the German Ministry for Education and Research (BMBF). The manuscript

has been greatly improved by helpful comments and discussions of two anonymous reviewers.

Chapter 4

Landfast ice affects the stability of the Arctic halocline: evidence from a numerical model

Abstract

Landfast ice covers large surface areas of the winter Siberian Seas. The immobile landfast ice cover inhibits divergent and convergent motion, hence dynamical sea ice growth and re-distribution, decouples winter river plumes in coastal seas from the atmosphere and positions polynyas at the landfast ice edge offshore. In spite of the potentially large effects, state-of-the-art numerical models usually do not represent landfast ice in its correct extent. A simple parametrization of landfast ice based on bathymetry and internal sea ice strength is introduced its effects on the Arctic Ocean are demonstrated. The simulations suggest that the Siberian landfast ice impacts the Arctic halocline stability through enhanced brine production in polynyas located closer to the shelf break and by re-directing river water to the Canadian Basin. These processes strengthen the halocline in the Canadian Basin, but erode its stability in the Makarov and Eurasian Basin.

4.1 Introduction

One of the dominant characteristics of the winter Arctic shelf seas is landfast ice (also land-fast, fast or shore-fast ice), sea ice that is immobile and mechanically fastened to the coast or to the sea floor. As there is no compressive deformation, landfast ice grows only thermodynamically and rarely exceeds thicknesses of 1.5 m (Romanov, 2004). It can extend a few (Beaufort Sea, Chukchi Sea, Western Laptev Sea) to several hundred kilometers from the coast into the ocean (Kara Sea, Eastern Laptev Sea, East Siberian Sea, see Fig. 4.1). The mechanisms that determine the landfast ice formation, extent and decay are not fully understood. To complicate things further, these mechanisms differ regionally. In the Chukchi and Beaufort Sea the landfast ice edge is found at relatively shallow depth of 18 m (Mahoney et al, 2007), while on the Eurasian shelf this depth is between 25 and 30 m (Dmitrenko et al, 2005b; Proshutinsky et al, 2007). In the Chukchi and Beaufort Sea the landfast ice is immobilized behind a row of bottom reaching pressure ridges (Mahoney et al, 2007). In the Kara Sea the landfast ice is formed behind a row of small islands parallel to the coast (Divine et al, 2004). At the landfast ice edge in the Laptev and East Siberian Seas grounded pressure ridges are rare (Reimnitz et al, 1994; Eicken et al, 2005). Proshutinsky et al (2007) proposed that the landfast ice edge occurs where the warm intermediate Atlantic water reaches the surface after upwelling at the shelfbreak. König Beatty and Holland (2010) attributed the landfast ice extent to the mechanical properties of the sea ice. Strong

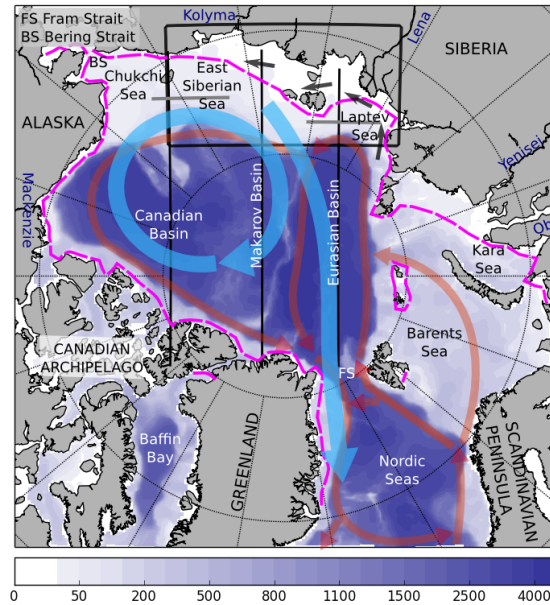


Figure 4.1: The Arctic Ocean and its marginal seas. The sea ice and surface circulation is schematically represented by light blue and mid-depth circulation by red arrows (simplified from Rudels et al (1994)), respectively. The landfast ice edge is depicted by the magenta dash line. The coastal current in the Laptev and East Siberian Seas is schematically represented by the black arrows. The black lines and box mark the sections and regions used in the model analysis.

freshwater and brackish sea ice (Dethleff et al, 1993; Eicken et al, 2005) formed in low salinity shelf seas with high river water content might ground at wide and shallow sand banks (Dethleff et al, 1993; Reimnitz et al, 1994) and from there extend with long tongues toward the landfast ice edge. Tides in the region are very weak and the tidal amplitudes of up to 10 cm in the Southeastern Laptev Sea (Fofonova et al, 2014) might not be large enough to deform the extensive landfast ice cover.

Especially in the Siberian Seas, where landfast ice has the largest extent, it is thought to have three roles:

1. Landfast ice limits the sea ice thickness by preventing sea ice compression (e.g. pressure ridges) in convergent motion of sea ice. By the same token it lowers the sea ice production by preventing sea ice divergence and lead formation. If these processes are not adequately represented in a numerical model, simulated thickness fields are not realistic (Johnson et al, 2012).

2. An immobile lid of the landfast ice effectively decouples the inner shelf from the atmosphere and affects the river water distribution. The seasonal runoff of the large Siberian rivers (Ob, Lena, Yenisei) determines the water masses of the shallow Siberian shelf. In a summer with strong onshore winds large parts of the summer maximal discharge can be held back on the inner shelf until winter (Dmitrenko et al, 2005a). The large amount of the fresh river water in the Arctic surface layer enhances the ocean stratification.
3. The extent of landfast ice determines the areas of low sea ice concentration—so called flaw polynyas (also flaw lead polynyas or flaw leads)—along the landfast ice edge during offshore wind conditions. The water in these polynyas is more saline than directly at the coast, where ocean salinities remain low due to fresh river water inflow and consequently more brine is rejected during sea ice production. The brine formed in the winter shelf seas maintain, along with the cool water formed by winter convection north of the Barents Sea (Rudels et al, 1996), the Arctic halocline (Aagaard et al, 1981; Martin and Cavalieri, 1989; Cavalieri and Martin, 1994a; Winsor and Björk, 2000). The cold and saline water flows off the shelves and sinks along the shelf break where it feeds into the halocline layer (Fig. 4.2), which decouples the cold Arctic surface layer from the warm intermediate-depth Atlantic layer. The surface layer stays cold with temperatures close to the freezing point due to a seasonal sea ice melting - freezing cycle and the layer is fresh due to a strong river runoff. In contrast, the ocean temperature at mid-depth is up to several degrees above zero. This warm and saline Atlantic water enters the ocean through the Nordic Seas (Fig. 4.1).

Landfast ice has been found important for the accurate simulation of the sea surface height (Proshutinsky et al, 2007) and sea ice thickness Johnson et al (2012). Although landfast ice is also important for the processes maintaining the Arctic halocline, it is usually not properly represented in state-of-the-art sea ice-ocean models. In this study we demonstrate the effects of the landfast ice for the Arctic halocline.

The outline of this paper is as follows. In section 4.2 we describe the numerical model for the sensitivity study. In Section 4.2.1 we describe the details of the landfast ice parametrization. In sections 4.3, 4.4 and 4.5 we present and discuss our results. A summary of our findings and final remarks are given in section 4.6.

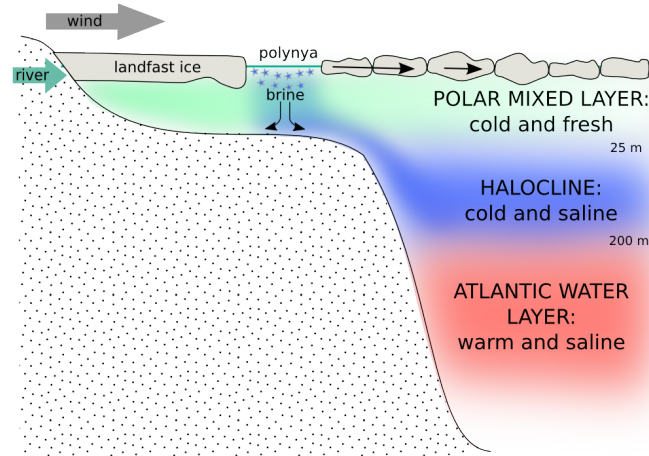


Figure 4.2: Arctic Ocean vertical stratification and winter processes maintaining the Arctic halocline.

4.2 Model setup

Our model is a regional coupled sea ice - ocean model based on the Massachusetts Institute of Technology General Circulation Model code - MITgcm (Marshall et al, 1997; MITgcm Group, 2014b) with a model domain covering the Arctic Ocean, Nordic Seas and northern North Atlantic. The horizontal resolution of is $1/4^\circ$ (~ 28 km) on a rotated grid with the grid equator passing through the geographical North Pole. The model has 36 vertical levels unevenly distributed in a way that the surface layer is well resolved at the cost of the poor resolution in the deep layer. The shelf bottom topography has realistic details that allow dense brine to flow downslope and off the shelf. Vertical mixing in the ocean is parameterized by a K-Profile Parameterization (KPP) scheme (Large et al, 1994) and tracers (temperature and salinity) are advected with an unconditionally stable seventh-order monotonicity preserving scheme (Daru and Tenaud, 2004) that requires no explicit diffusivity. The sea ice model is a dynamic-thermodynamic sea-ice model with a viscous-plastic rheology (Losch et al, 2010). The model has a non-linear free surface and sea ice that depresses the surface ocean layer according to its mass. We avoid numerical issues associated with too thin surface layers when ice gets very thick by using a rescaled vertical z^* -coordinate (Campin et al, 2008) that distributes the excursion of the free sea surface between all vertical levels to the bottom. The same model set-up has been used by Itkin et al (2013) except that now the vertical background diffusivity has been lowered to 10^{-6} m^2/s as recommended by Nguyen et al (2009) to achieve a better defined Arctic halocline.

The model is initialized by the PHC climatology (Steele et al, 2001) and has initially no sea ice cover. For a spin-up we run the model for 30 years forced by the atmospheric climatology of the Coordinated Ocean Research Experiment (CORE) version 2 based on a reanalysis of the National Center for Atmospheric Research/National Centers for Environmental Prediction (NCAR/NCEP) (Large and Yeager, 2009). Subsequently the model is driven from 1948 to 1978 by daily atmospheric data also provided by CORE. Our model experiments start in 1979 and continue until 2010. They are forced by the atmospheric reanalysis – The Climate Forecast System Reanalysis (NCEP–CFSR) (Saha et al, 2010). Surface salinity in ice free regions is restored to a mean salinity field (PHC climatology) with a time scale of 180 days to avoid model drift. River runoff was treated like a surface volume flux and it was prescribed for the main Arctic rivers according to the Arctic Ocean Model Intercomparison Project (AOMIP, <http://www.whoi.edu/projects/AOMIP/>) protocol. Open boundaries are formulated following Stevens (1991); they are located at 50°N in the Atlantic and just south of the Bering Strait. Temperature and salinity at the open boundaries are taken from the PHC climatology. The Barents Strait inflow is prescribed as 0.8 Sv and the stream function at open boundary in the Atlantic Ocean derived from a North Atlantic simulation (Gerdes and Köberle, 1995) and modified to balance the net volume flow in the model domain.

4.2.1 Landfast ice Parameterization

The mechanisms that determine the landfast ice formation and extent depend of the specific region and are not fully understood. There have been many attempts to model or parameterize landfast ice. Lieser (2004) developed a parameterization based on the ratio of sea ice thickness and total water column depth. For a specified threshold ratio the grid cells assigned as landfast ice remained at rest and surface momentum flux into the ocean was set to zero. His approach in a $1/4^\circ$ (28 km) model resulted in too thick landfast ice that even survived the summer. A similar procedure was used in higher horizontal resolution models (3-12 km) by Johnson et al (2012) and Rozman et al (2011). Both studies use prescribed landfast ice areas obtained from bathymetrical limits or observations. In the Kara Sea, where the landfast ice forms over deep waters behind a row of coastal islands, Olason (2012) successfully modeled landfast ice by adjusting the internal sea ice strength parameters in the viscous-plastic rheology of Hibler (1979).

Our model grid does not resolve small islands and shallow topographical features

in the Siberian Seas, where the landfast ice might get grounded. Therefore we designed a simplified and uniform parametrization based on König Beatty and Holland (2010) that takes into account water column depth and landfast ice internal strength. The latter is justified by a sharp salinity gradient between the shallow shelf waters of the Kara, Laptev and East Siberian Sea and the deep ocean. In 1992, Dethleff et al (1993) documented freshwater ice up to 100 km seaward off the Lena Delta. In 1999 the freshwater and brakish sea ice with salinity below 1 was confined to the coastal waters adjacent to the eastern Lena Delta with water depth less than 10 m, while river water on average still contributed 62 % of the landfast ice further offshore in the southeastern Laptev Sea (Eicken et al, 2005). .

In the widely used sea ice strength parametrization (e.g. Hibler (1979); Zhang and Hibler III (1997)) compressive strength P depends just on the sea ice thickness h and concentration A :

$$P = P^* h \exp(-C^*(1 - A)), \quad (4.1)$$

where the empirical sea ice strength parameters, $P^* = 2750N/m^2$ and $C^* = 20$ are constants.

The landfast ice parametrization used in this study takes into account the unresolved shallow topographical features inside the maximal landfast ice edge mark (25 m) and increased sea ice internal strength attributed to the lower sea ice salinity in the same area by setting the P^* to the double of the drift ice. Such landfast ice would still fail under strong offshore wind if the distance between the coastline and 25-m-bathymetrical boundary is large. To prevent this we amended the sea ice rheology in the regions shallower than 25 m with sea ice tensile strength T following König Beatty and Holland (2010):

$$\zeta = \frac{P + T}{2\Delta}, \quad (4.2)$$

$$\eta = \frac{P + T}{2\Delta e^2} = \zeta/e^2, \quad (4.3)$$

and

$$p = P - T, \quad (4.4)$$

where ζ is bulk viscosity, η is shear viscosity, $e = 2$ is eccentricity constant and p is the pressure term. This moves the elliptical yield curve in the principal

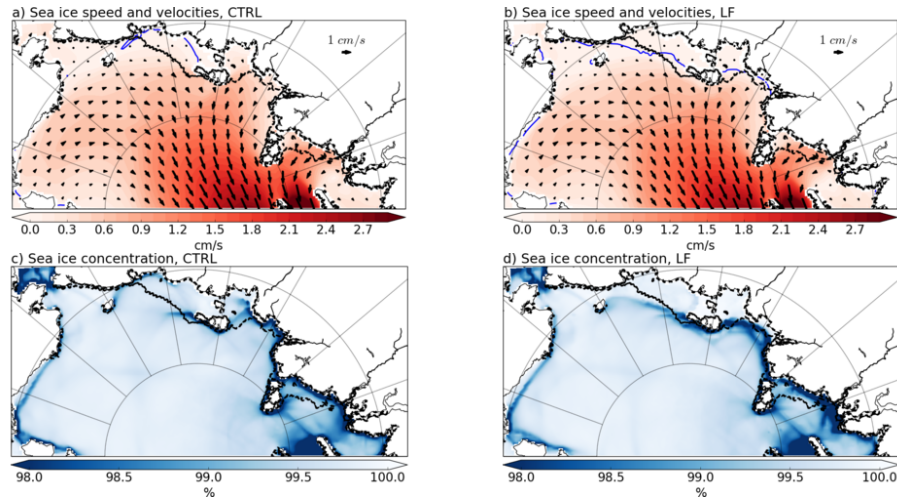


Figure 4.3: The effect of the landfast ice parametrization on the mean April (2000-2010) sea ice concentration (a,b) and motion (c,d). a,c - CTRL, b,d - LF. Speed 1 mm/s is contoured by blue line. Mean April landfast edge from the AARI dataset (1997-2006) is depicted by gray dash line.

stress space into the I. quadrant, when the water column is shallower than 25 m and leaves the curve unmodified otherwise. $T = \frac{P}{2}$, which is consistent with the estimates by Tremblay and Hakakian (2006).

For the sensitivity study we compare a control run (CTRL) and a landfast ice run (LF) that differ only in this additional landfast ice parameterization.

4.3 Impact of the landfast parameterization on the sea ice

In the Laptev and East Siberian Sea the landfast ice cover forms in December, reaches its maximal extent in April, breaks up into fully drifting ice in May or June and melts in summer. Starting in May, the atmospheric temperatures are too warm to have a significant amount of brine produced in the polynya. Hence, in this study we define wintertime as the months December to April. In our model landfast ice breaks up completely in early summer. At atmospheric temperatures above zero and when A drops below 1, sea ice loses its internal strength exponentially making P^* irrelevant, because P depends exponentially on A .

If we define coastal sea ice with drift speeds below 1 mm/s as landfast ice, then the parametrization in LF comparing to CTRL leads to substantially larger

areas of landfast ice in April, during the annual maximal extent (Figure 4.3 panels a and b). The simulated landfast ice is slow enough for polynyas to form at its seaward edge (Figure 4.3 c and d). The 1 mm/s contour and polynyas in LF agree better with the 1997-2006 landfast ice edge produced by the Arctic and Antarctic Research Institute, Saint Petersburg, Russia (Smolyanitsky et al (2007), hereafter AARI dataset). In LF, however, the Laptev Sea the polynya is located too far away from the coast. This might be a consequence of the coarse model resolution and the high P^* value. In the Kara Sea our parametrization has only a minor effect because the shelf sea ice is much deeper than the 25 m threshold we use in the parametrization and the small offshore islands there are located in areas where the surrounding seas exceed the depth of 150 m.

The effect of the parametrization is clearly visible in the sea ice thickness maps (Fig. 4.4). LF sea ice is thinner by up to 30 cm under the regions affected by the landfast ice parametrization in the Kara, Laptev, East Siberian, Chukchi and Beaufort Seas. The difference pattern accurately matches the landfast ice extent from the AARI dataset (Fig. 4.3). The largest negative differences are in the polynya at the landfast ice edge in the East Siberian and Laptev Seas, while in the coastal regions of the Laptev Sea differences are positive to reflect the erroneous polynya location in the CTRL.

The thinner sea ice in the landfast ice area in LF is a consequence of exclusive thermodynamic sea ice growth. The thermodynamical growth itself is also different between the runs (Fig. 4.4): in both cases the highest growth rates occur in the polynyas. In LF this is further offshore than in CTRL.

As a volume of water is thermodynamically turned into sea ice, salt is expelled from this volume and remains in the ocean. Because this process increases the salinity in the surface ocean, one can define a 'virtual salt flux' $S_{flux} = FW_{flux}S$, where FW_{flux} is freshwater flux and S is the salinity of the surface water minus 4 where the salinity is equal or higher than 4. This approximates the constant sea ice salinity of 4 in our model. The resulting S_{flux} differences resemble the difference pattern in the thermodynamic growth (Fig. 4.4). Because S_{flux} depends also on the sea surface salinity its is relatively low in the East Siberian Sea although the sea ice production there is high. S_{flux} is an order of magnitude higher and opposite in sign compared to the virtual salt flux generated by the sea surface salinity restoring (not shown). Salinity is only restored to climatology in the ice free part of the model grid cell.

The largest differences in the winter sea ice cover between the runs are found in the Laptev and East Siberian Seas. This is the area with the greatest landfast

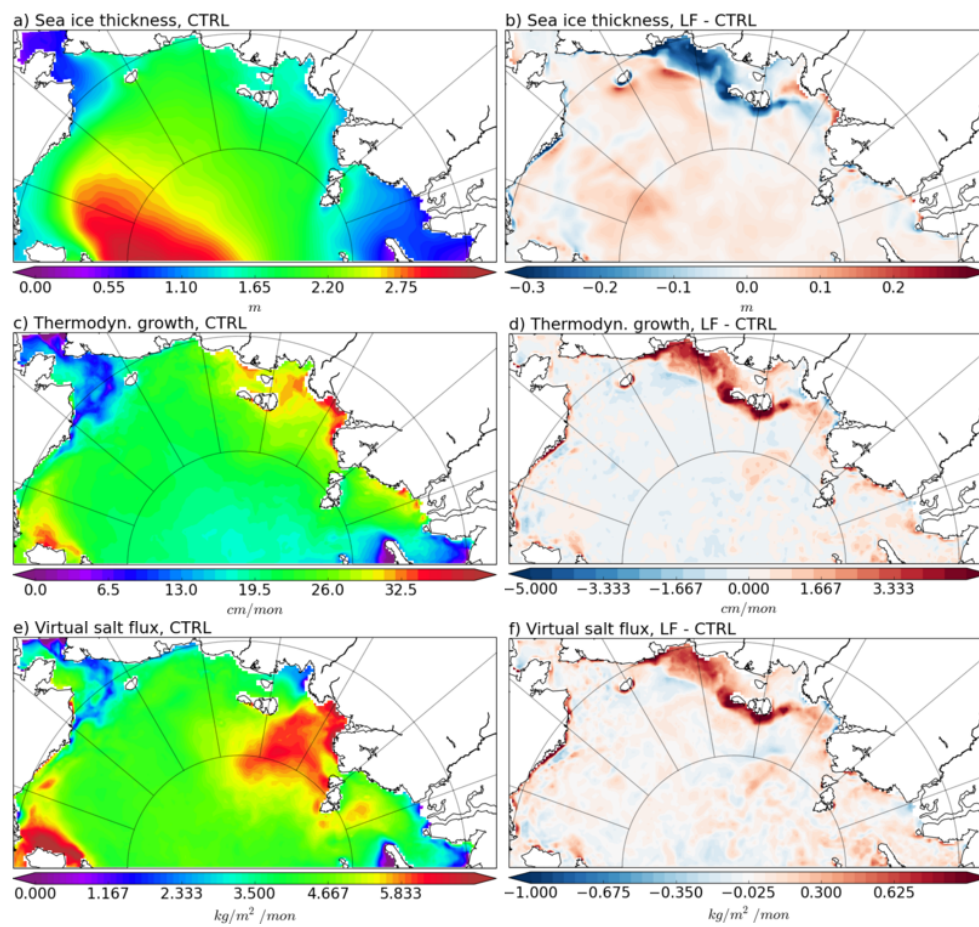


Figure 4.4: Mean winter (2000-2010) sea ice thickness, thermodynamical growth and salt flux from the sea ice thermodynamical growth: a - CTRL, b - LF minus CTRL.

ice extent over the shallow shelf and hence our parametrization has the largest effect there. In time series, we compare the contributions of wintertime sea ice concentration, thickness, sea ice production, ocean surface salinity and S_{flux} to wintertime dense shelf water production in both simulations (Fig. 4.5). The mean sea ice concentration over the Siberian Seas is high and very similar in both simulations. This is not surprising as the differences between the runs are mainly in the positioning of the polynyas within the Siberian Seas. The sea ice concentrations are a little lower in CTRL as the drifting sea ice allows more small leads. Sea ice is about 10 cm thinner in LF than in CTRL. This is a consequence of less ridging through convergent motion in the landfast ice area and less advection of sea ice into the region. In contrast, there is more thermodynamically grown sea ice in LF. While the polynyas in LF are shifted offshore into more saline sea water, a higher fraction of fresh river water reduces the salinity in the shelf seas. Towards the end of the runs these counteracting effect leads to a similar surface salinity in polynyas in both runs. Still, higher sea ice production leads to higher S_{flux} in LF.

The differences in the sea ice production and S_{flux} between CTRL and LF are geographically distributed as expected so that we conclude that this sensitivity study can be used to estimate the importance of the landfast ice for the Arctic Ocean halocline stability.

4.4 Impact of the landfast parameterization on the Arctic halocline

In this section we compare the end of winter (April) climatologies (2000-2010) because of the high seasonality of the mixed layer depth in the Arctic. First we examine the buoyancy, $b = -g \frac{\rho - \rho_0}{\rho_0}$ at the top of the halocline (25 – 30 m). The differences between LF and CTRL show regional effects of the landfast ice parametrization with less buoyancy in LF in the Canadian Basin and more buoyancy centered in Makarov and Eurasian Basins (Fig. 4.6a and b).

To understand the relevance of these differences to the water column stability we examine three oceanographic sections; each section runs through one of the major Arctic basins: Canadian, Makarov and Eurasian as shown on Fig. 4.1 and 4.6. In the first section running from the Eurasian coast over the Wrangel Island to the Ellesmere Island (Fig. 4.7) there is increased salinity by locally up to 0.6 at the halocline layer in LF (25 – 30 m), while the surface layer tends to

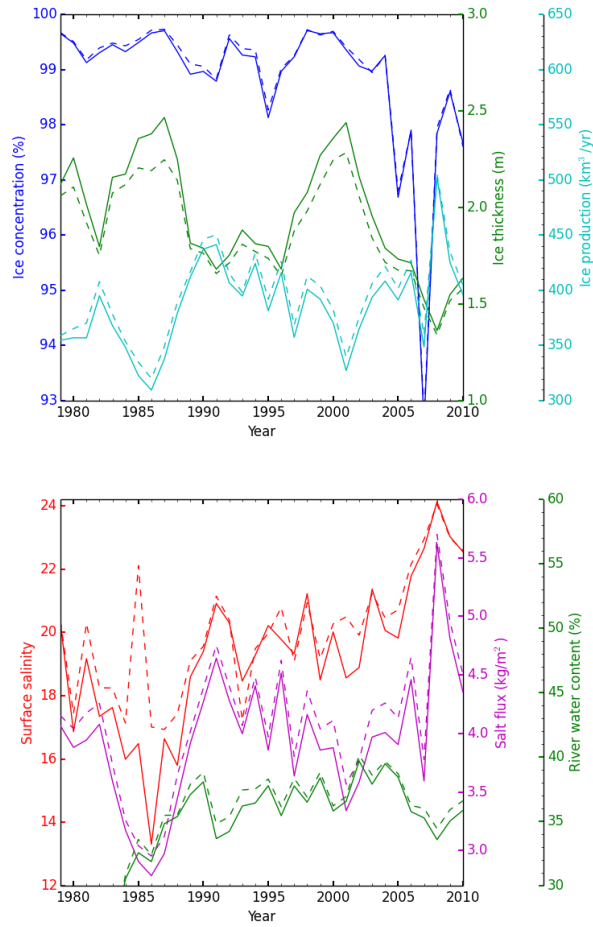


Figure 4.5: Mean winter (December-April) sea ice time series for the Laptev Sea and East Siberian Sea. CTRL and LF are represented by solid and dash lines, respectively: a - mean sea ice concentration and thickness with total sea ice production; b - sea surface salinity of the areas with the production higher than 30 cm, salt flux resulting from the production and river water content.

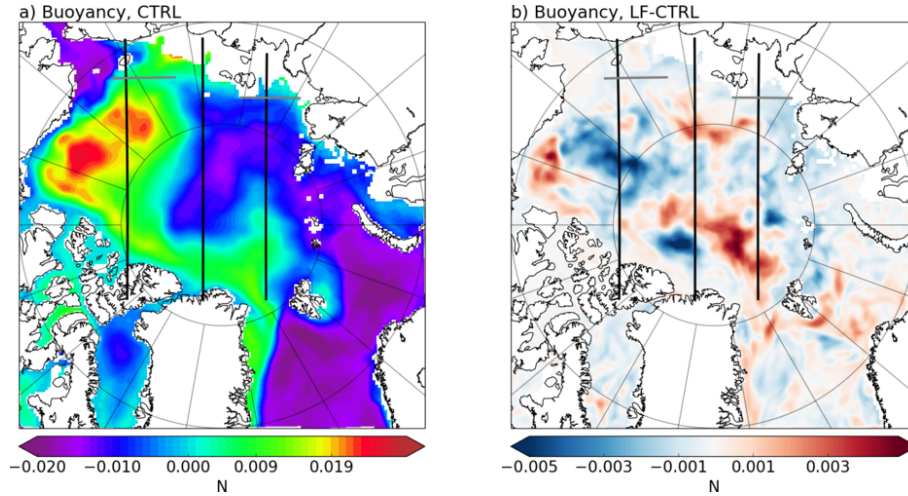


Figure 4.6: Mean April (2000-2010) buoyancy at the top halocline (25-30 m): a - CTRL, b - LF minus CTRL. Black lines mark the profile sections across Canadian, Makarov and Eurasian Basins (Figs. 4.7, 4.9, and 4.10). Gray line marks a section for the time series at the Eurasian shelf break (Fig. 4.8).

be fresher than in CTRL. Especially in the surface layer, the differences are not homogeneous and locally have alternating signs. Along with the increased temperature at the top halocline depth this suggests this layer is fed by relatively warm shelf bottom water mixed with brine originating from the sea ice production. This influence is supported by the Hovmöller diagrams of differences at the section across the pathway of the water masses from the East Siberian Sea to the Canadian Basin (Fig. 4.8 a and b). In LF, this shelf water has continuously larger salinity at the halocline depth (panel a), while the surface layer is typically fresher which generally is associated with higher river water content (panel b). The salinity and river water fraction in the surface layer differences are not constant in time. Notably the salinity difference is positive in the early 1990s and in the mid 2000s. Both events are accompanied with a negative difference in river water fraction. The differences in temperature and salinity described above have consequences for the stratification. The buoyancy frequency N^2 is larger in LF than in CTRL pointing to a higher stability at the winter mixed layer depth.

In contrast, the second section which runs from East Siberian Sea to the Northern Greenland (Fig. 4.9) shows a different pattern with higher salinities by up to 0.8 in the surface layer that reflects a decreased river water content in LF compared to CTRL. The salinity at the depth of the halocline only increases only by about 0.1, such that the overall stability of the upper halocline is reduced. The third section runs from the Laptev Sea to the Fram Strait (Fig. 4.10). Here

the differences between the runs are similar as in the second section, but not as pronounced. While there is still less river water in the surface layer, the halocline layer has more river water in LF than in CTRL. Here, the landfast ice parametrization has no clear effect on the halocline stability. This is again supported by the Hovmöller diagrams of differences at the section across the pathway of shelf water from the Laptev Sea (Fig. 4.8 c and d). In LF, the surface layer is mostly more saline, while the time series of the river water fraction differences show a strong seasonal cycle with typically less river water in the surface layer in the winter and more in the summer (not shown).

4.5 Discussion

Landfast ice simulated in LF grows almost exclusively thermodynamically and allows very little ice production due to convergent motion (dynamical sea ice growth). Therefore the coastal regions covered by landfast ice in LF are thinner than in CTRL. To some extent, the arbitrary choice of the 25 m isobath for turning on the parameterization places the polynyas in the approximately observed positions. In contrast, in CTRL polynyas are located directly on the coast. The shift of the polynyas from the coast in CTRL toward a realistic landfast ice edge location in LF moves the brine production closer to the shelfbreak and into more saline ocean where more brine is produced per sea ice volume.

To determine if the amount of brine produced in our simulations is realistic we first compare the available sea ice production estimates for the Laptev Sea. In LF during 2000s a mean of 144 km^3 of sea ice is produced per winter (not shown, but Fig. 4.5a shows winter sea ice production for the East Siberian and Laptev Sea, roughly half of which is produced in that Laptev Sea. That is above Rabenstein et al (2013)'s estimate of $94 \pm 27 \text{ km}^3$ for the southeastern Laptev Sea for winter (late December till mid-April) 2007/2008. Willmes et al (2011) estimate a lower $55 \pm 15 \text{ km}^3$ for the entire Laptev Sea during winter, but these authors only took into account ice production in areas with sea ice thinner than 20 cm.

Our results indicate that with an appropriate representation of landfast ice more river water is stored in the Siberian Seas. While in CTRL more river water is dispersed by the wind acting through the drifting sea ice, in LF this river water is protected from the wind by the immobile shield of the landfast ice and remains on the shelf. From there the river water plume is driven northeastward by geostrophic currents (black arrows on Fig. 4.1) into the Canadian Basin

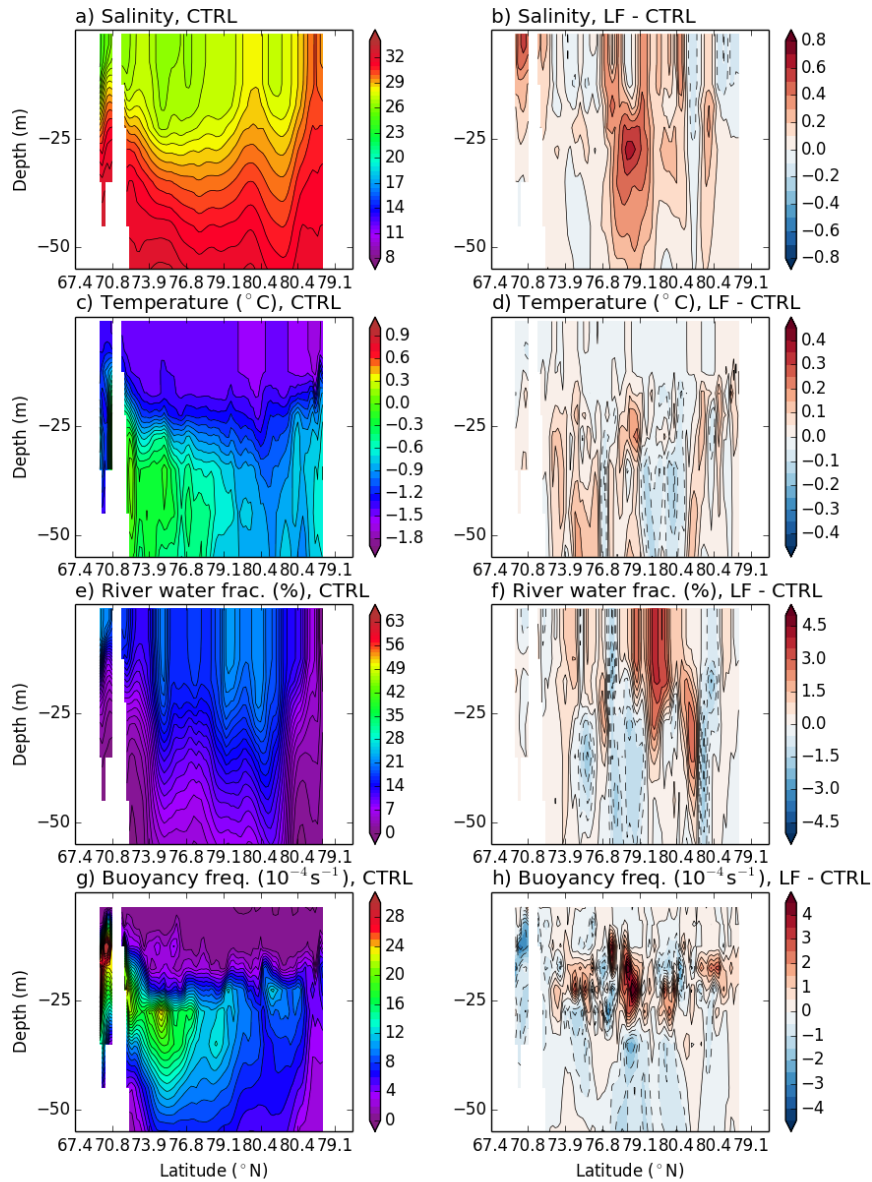


Figure 4.7: Mean April (2000-2010) salinity, temperature, river water fraction and buoyancy frequency along the section across the Canadian Basin.

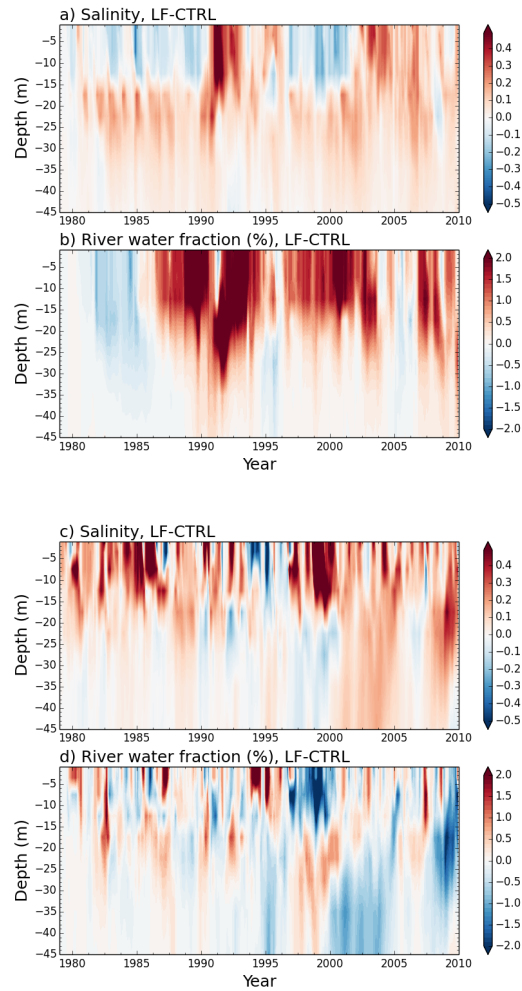


Figure 4.8: Hovmöller diagrams of monthly mean salinity and river water fraction differences between LF and CTRL: average over an oceanographic section at the Eurasian shelf break north of the East Siberian Sea (a,b) and at the Laptev Sea shelf break (c,d). Sections are marked by gray lines on Fig. 4.1 and 4.6.)

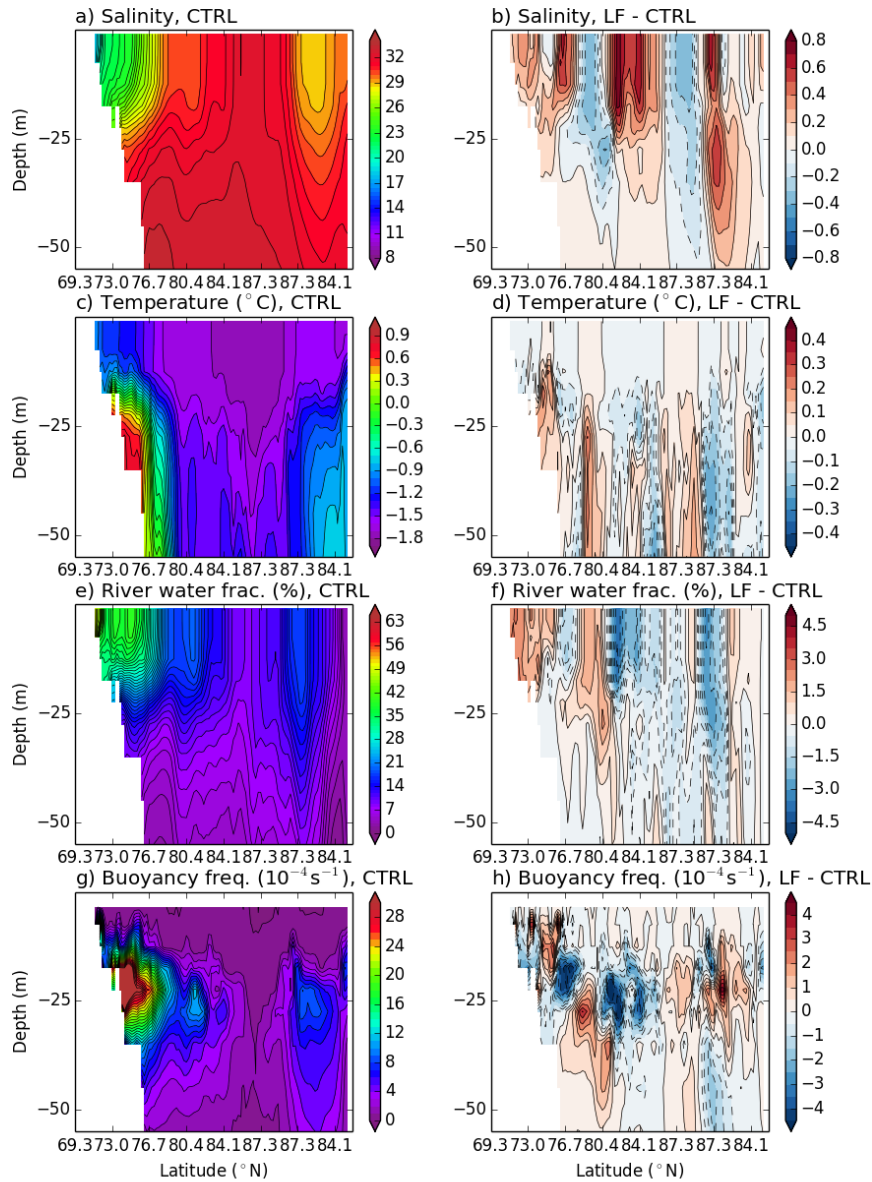


Figure 4.9: Mean April (2000-2010) salinity, temperature, river water fraction and buoyancy frequency along the section across the Makarov Basin

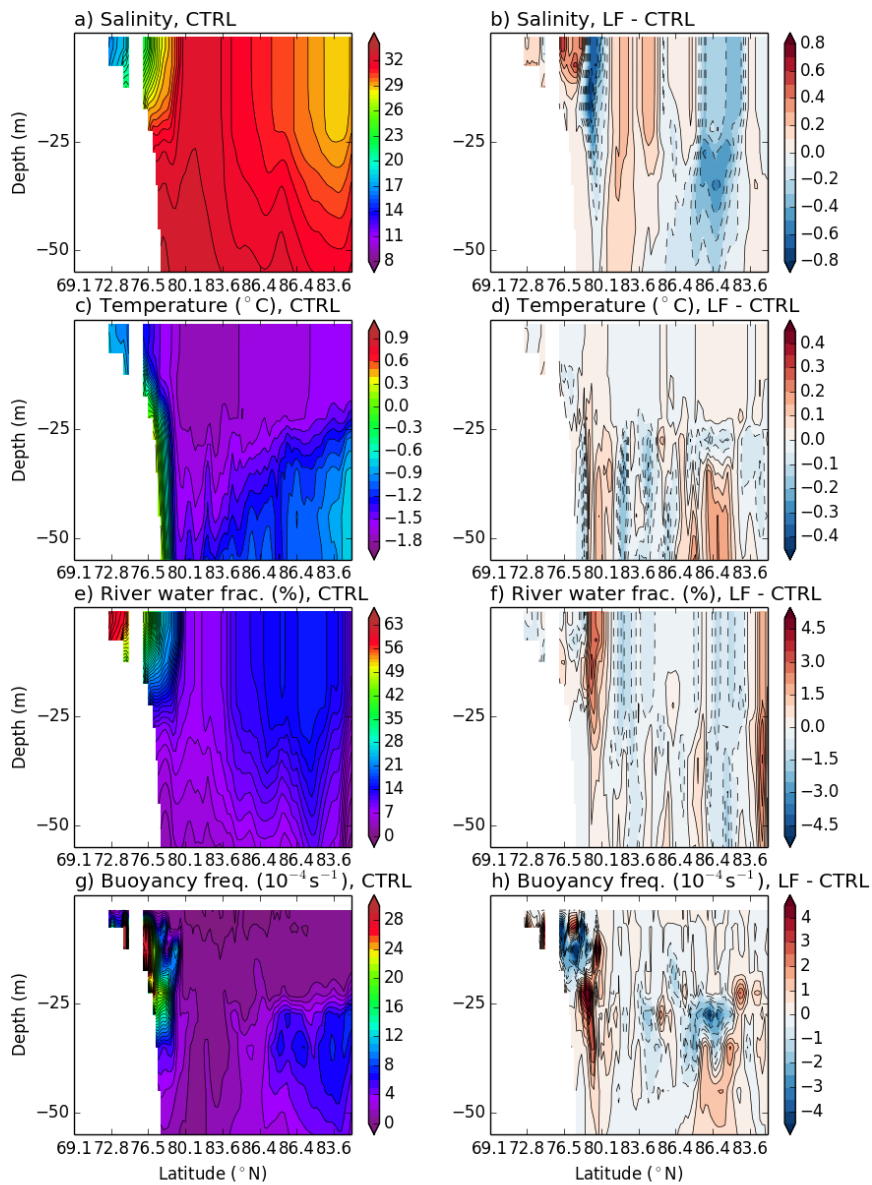


Figure 4.10: Mean April (2000-2010) salinity, temperature, river water fraction and buoyancy frequency along the section across the Eurasian Basin.

and less river water reaches other parts of the Arctic. In LF, in summers with strong offshore winds the increased amounts of the river water stored on the shelf during the winter are driven northwards into the European and Makarov Basins. Still, these river water pulses do not change the sign of the salinity differences in the surface layer and do not affect the halocline stability.

The combined effect of increased brine export to the Central Arctic and redistribution of the river water from the winter shelf in LF compared to the CTRL changes the buoyancy at the Arctic halocline. In the Canadian Basin the surface layer freshens locally due to increased river water content as a consequence of the landfast ice parametrization, while the halocline layer becomes saltier due to the difference in the brine production in the Siberian polynyas. Both surface and halocline depth differences make the halocline in LF stronger. Our simulation supports Nguyen et al (2012)'s conclusions that the Canadian Basin halocline is maintained by the dense water formed on the Eurasian shelf.

In the Makarov and Eurasian Basin the difference signal is dominated by the increase in the surface salinity that is again the consequence of the redirection of the river water to the Canadian Basin. Consequently the already weak halocline in this sector of the Arctic (Boyd et al, 2002; Rudels et al, 2004) is further eroded in LF. The effect of the landfast ice resembles that of the Great salinity anomaly (Steele and Boyd, 1998; Johnson and Polyakov, 2001) observed in the early 1990s, where the changes in the wind circulation enhanced the river water export to the Canadian Basin and increased brine production in the Siberian Seas polynyas that eroded the Arctic halocline over substantial parts of the Arctic Ocean. During the Great salinity anomaly and similarly also in the mid 2000s landfast ice in LF has an effect outweighing the anomalous offshore winds and the differences in surface salinity and river water content of the shelf waters originating from the East Siberian Sea during these two periods change the sign (Fig. 4.8a and b).

Yu et al (2014) detected a general decrease of the Arctic landfast ice extent of 7 ± 1.5 % per decade in the period from 1976 till 2007. In the Chukchi, Laptev and East Siberian Seas also the landfast ice season is getting shorter, reflecting the general negative trend in the summer sea ice extent in the Siberian Seas (Comiso et al, 2008; Stroeve et al, 2012). According to our results this trend should have implications for the halocline stability. The reduction in the extent and duration in the Siberian Seas would lead to a weaker halocline in the Canadian Basin, but conversely also to a stronger halocline in the Makarov and Eurasian Basins. Especially for the latter two basins the Atlantic water

layer has been reported to be warming (Polyakov et al, 2010). In such a case, the loss of the landfast ice would inhibit the heat transport from the Atlantic Water layer to the surface and delay the further rapid sea ice loss in the Arctic.

4.6 Summary and conclusions

An accurate representation of the landfast ice in a sea ice-ocean coupled model has an impact not only on the winter sea ice and brine production but also on the river water distribution. The landfast ice in the LF shields the river water that remains on the shelf in winter from the winds and promotes northeastward flow of the river water with the coastal currents. We have been able to show this in a sensitivity study with a simple-to-implement landfast ice parametrization that generated landfast ice over extensive areas of the Laptev and East Siberian Seas. In LF more river water reaches the Canadian Basin and less the Makarov and Eurasian Basin. Also the polynyas are located closer to the shelf break. From there more brine reaches the halocline depth of the Canadian Basin. The surface salinity decrease due to the river water and the halocline salinity increase due to the brine both strengthen the halocline in the Canadian Basin, whereas in the Makarov and Eurasian Basins the surface salinity increase erodes the already low halocline stability. Consequently in the latter two basins where the Atlantic water layer is still relatively warm and the halocline is already eroded, extensive landfast ice further weakens the halocline and promotes entraining Atlantic water into the ocean mixed layer that might lead to sea ice melt.

Based on our simulations we recommend to include our landfast ice parametrization to those regional numerical models that address the halocline stability and shelf - deep basin exchanges. The stratification modified by brine produced in the polynyas and the river water that supplies the Arctic Ocean with sediments, nutrients, and pollutants are key factors for biogeochemical processes.

Acknowledgments

We would like to thank Valeria Selyuzhenok, Alfred Wegener Institute for her help with the observational data comparison. We are grateful to Karel Castro-Morales and Kathrin Riemann-Campe, also Alfred Wegener Institute who have contributed to the model development. Polona Itkin's PhD studies have been partially supported by a grant of the Municipality of Ljubljana, Slovenia.

Chapter 5

Summary and Concluding Remarks

In this thesis our key hypothesis was that a change in the sea ice motion causes significant changes in the ocean properties and circulation.

1. For the Siberian Seas remote sensing products give a good estimate of the sea ice drift direction, but compared to a point in-situ measurements underestimate the sea ice drift speed. The model of a high spatial resolution as NAOSIM is able to reproduce a reasonable sea ice motion in the coastal areas.
2. Exact landfast ice parametrization can be achieved by prescribing a landfast ice mask. But due to the unavailability of such mask for a climatological simulation (landfast ice exhibits internannual variability) and unknown trends of the landfast ice extent in the future we decided for a more dynamical landfast ice parameterization where the sea ice in the shallow regions has tensile strength (resistance to divergence) and a doubled compressive strength (resistance to convergence and deformation).
3. Landfast ice in the model simulation shifts the flaw polynya, location of strong winter sea ice and brine production away from the coast in the more saline ocean waters and more brine reaches the Arctic halocline. This strengthens the halocline that shields cold surface waters and sea ice from the warm AWL underneath.
4. A general change in the sea ice internal strength leads to substantial changes in the ocean properties and circulation. Under weaker and more

mobile sea ice AWL temperatures are reduced by 0.2 K. The Eurasian basin circulation in the AWL is increased and this leads to the volume transports adjustments at the Arctic Straits.

5. The results from this sensitivity study can be understood as test of the two modes in the Arctic sea ice: prior to the recent climate change and thereafter.

This confirms our hypothesis. The slowing down and stopping of the sea ice motion over parts of the Siberian Seas by the means of the landfast ice results in changes of salinity of the Arctic halocline layer. The increase in the sea ice motion by means of decreasing the sea ice internal strength (P) results in changes of the AWL temperature and volume transports across the Arctic Straits. The latter effect shows that the Arctic sea ice properties and motion are not only important for the Arctic ocean, but may have consequences also for the global ocean circulation.

5.1 Outlook

A logical continuation of the work done for this thesis would be to downscale the MITgcm to a higher resolution and preform first a validation of the sea ice motion for the whole Arctic and then also a similar validation of the near coast sea ice motion in the Siberian Seas as it was done with NAOSIM in the Paper 1.

The landfast ice parametrization should be tested and possibly adjusted for the high resolution of the MITgcm. Further improvements towards a more physically based landfast ice parametrization would be to define the P* parameter as a function of the brine volume. In engineering sea ice strength is commonly defined as a function brine volume v_b (Timco and O'Brien, 1994; Timco and Weeks, 2010) in the empirical formulas:

$$v_b = S_i \left(\frac{49.185}{|T_i|} + 0.532 \right), \quad (5.1)$$

where S_i and T_i are the sea ice salinity and temperature, respectively. The uniaxial sea ice compressive strength σ_c for a horizontally loaded first year columnar ice is defined as:

$$\sigma_c = 37(\dot{\epsilon})^{.22} \left(1 - \sqrt{\frac{v_T}{270}}\right), \quad (5.2)$$

where $\dot{\epsilon}$ is the strain rate and $v_T = v_b + v_a$ is the total porosity which takes into account also the volume of the air bubbles in the ice (v_a). The tensile strength σ_t for horizontally loaded samples is approximated by:

$$\sigma_t = 4.278v_T^{-.6455}. \quad (5.3)$$

Another interesting task would be to explore the trends in the landfast ice duration and extent in the scope of the future climate changes. The current parametrization is sea ice concentration dependent which is in turn a function of the air temperature. This means that in the future warmer climate the landfast ice season would be appropriately shortened. The atmospheric forcing for the future climate could be obtained from one of the Coupled Model Intercomparison Project (CMIP5, <http://cmip-pcmdi.llnl.gov/cmip5/>) coupled climate models participating in the Intergovernmental Panel for Climate Change (IPCC) assessment reports.

Our research focuses on the importance of the sea ice internal stress for the sea ice mobility, but the sea ice motion depends on other factors as well. In the sea ice momentum balance equation 1.3 sea ice motion depends on the τ_a and τ_o - air and ocean stress. The intensity of the air-ice and ocean-ice is defined by the drag coefficients. While in nature the sea ice surface and underside are roughed by ridges, melt ponds and ice floe edges, in the state-of-the-art climate models the drag coefficients are kept constant in time and space without considering their dependence on the ice surface and bottom topography. Changing these values should have a significant influence on the sea ice motion.

Bibliography

- Aagaard K, Coachman L, Carmack E (1981) On the halocline of the Arctic Ocean. *Deep Sea Research Part A Oceanographic Research Papers* 28(6):529–545
- Abrahamsen E, Meredith M, Falkner K, Torres-Valdes S, Leng M, Alkire M, Bacon S, Laxon S, Polyakov I, Ivanov V (2009) Tracer-derived freshwater composition of the Siberian continental shelf and slope following the extreme Arctic summer of 2007. *Geophysical Research Letters* 36:L07,602
- Adams S, Willmes S, Heinemann G, Rozman P, Timmermann R, Schröder D (In press) Evaluation of simulated sea-ice concentrations from sea ice-ocean models using satellite data and polynya classification methods. *Polar Research Special Issue: Laptev Sea System*
- Alexandrov V, Martin T, Kolatschek J, Eicken H, Kreyscher M, Makshtas A (2000) Sea ice circulation in the Laptev Sea and ice export to the Arctic Ocean: Results from satellite remote sensing and numerical modeling. *Journal of Geophysical Research-Oceans* 105(C7)
- Bauch D, Dmitrenko I, Wegner C, Hölemann J, Kirillov S, Timokhov L, Kassens H (2009) Exchange of Laptev Sea and Arctic Ocean halocline waters in response to atmospheric forcing. *Journal of Geophysical Research-Oceans* 114(C5):C05,008
- Belliveau D, Bugden G, Eid B, Calnan C (1990) Sea ice velocity measurements by upward-looking Doppler current profilers. *Journal of Atmospheric and Oceanic Technology* 7(4):596–602
- Beszczyńska-Möller A, Fahrbach E, Schauer U, Hansen E (2012) Variability in Atlantic water temperature and transport at the entrance to the Arctic Ocean, 19972010. *ICES Journal of Marine Science: Journal du Conseil* DOI 10.1093/icesjms/fss056

- Boyd TJ, Steele M, Muench RD, Gunn JT (2002) Partial recovery of the Arctic Ocean halocline. *Geophysical Research Letters* 29(14):2–1–2–4, DOI 10.1029/2001GL014047
- Campin J, Marshall J, Ferreira D (2008) Sea ice-ocean coupling using a rescaled vertical coordinate z^* . *Ocean modelling* 24(1-2):1–14
- Carmack EC, Aagaard K, Swift JH, MacDonald RW, McLaughlin FA, Jones EP, Perkin RG, Smith JN, Ellis KM, Killius LR (1997) Changes in temperature and tracer distributions within the arctic ocean: results from the 1994 arctic ocean section. *Deep Sea Research Part II: Topical Studies in Oceanography* 44(8):1487 – 1502, DOI 10.1016/S0967-0645(97)00056-8
- Cavalieri D, Martin S (1994a) The contribution of Alaskan, Siberian, and Canadian coastal polynyas to the cold halocline layer of the Arctic Ocean. *Journal of Geophysical Research-Oceans* 99(C9)
- Cavalieri D, Martin S (1994b) The contribution of Alaskan, Siberian, and Canadian coastal polynyas to the cold halocline layer of the Arctic Ocean. *Journal of Geophysical Research-Oceans* 99(C9)
- Comiso J, Parkinson C, Gersten R, Stock L (2008) Accelerated decline in the Arctic sea ice cover. *Geophys Res Lett* 35(1):L01,703
- Cordey R, Desnos Y, Rosich B (2004) ASAR Wide-Swath Single-Look Complex Products: Processing and Exploitation Potential. In: *Proceedings of ESA FRINGE workshop 2003, vol 3*, pp 1–5
- de Couet T, Maurer T (2009) Surface Freshwater Fluxes into the World Oceans. Tech. rep., Global Runoff Data Centre. Koblenz: Federal Institute of Hydrology (BfG), URL http://www.bafg.de/GRDC/EN/03_dtprdcsts/31_FWFLX/freshflux_node.html
- Daru V, Tenaud C (2004) High order one-step monotonicity-preserving schemes for unsteady compressible flow calculations. *JOURNAL OF COMPUTATIONAL PHYSICS* 193(2):563–594, DOI {10.1016/j.jcp.2003.08.023}
- Dethleff D, Nürnberg D, Groth E (1993) East siberian arctic region expedition'92: the laptev sea: its significance for arctic sea-ice formation and transpolar sediment flux/by d. dethleff... *Berichte zur Polarforschung (Reports on Polar Research)* 120
- Divine D, Korsnes R, Makshtas A (2004) Temporal and spatial variation of shore-fast ice in the Kara Sea. *Continental Shelf Research* 24(15):1717–1736

- Dmitrenko I, Kirillov S, Eicken H, Markova N (2005a) Wind-driven summer surface hydrography of the eastern siberian shelf. *Geophysical research letters* 32(14):L14,613
- Dmitrenko I, Tyshko K, Kirillov S, Eicken H, Hölemann J, Kassens H (2005b) Impact of flaw polynyas on the hydrography of the Laptev Sea. *Global and planetary change* 48(1-3):9–27
- Dmitrenko I, Polyakov I, Kirillov S, Timokhov L, Frolov I, Sokolov V, Simmons H, Ivanov V, Walsh D (2008a) Toward a warmer Arctic Ocean: Spreading of the early 21st century Atlantic Water warm anomaly along the Eurasian Basin margins. *Journal of Geophysical Research* 113(C5):C05,023
- Dmitrenko IA, Polyakov IV, Kirillov SA, Timokhov LA, Frolov IE, Sokolov VT, Simmons HL, Ivanov VV, Walsh D (2008b) Toward a warmer Arctic Ocean: Spreading of the early 21st century Atlantic Water warm anomaly along the Eurasian Basin margins. *Journal of Geophysical Research: Oceans* 113(C5), DOI 10.1029/2007JC004158
- Dmitrenko IA, Kirillov SA, Tremblay LB, Bauch D, Hlemann JA, Krumpen T, Kassens H, Wegner C, Heinemann G, Schrder D (2010) Impact of the arctic ocean atlantic water layer on siberian shelf hydrography. *Journal of Geophysical Research: Oceans* 115(C8), DOI 10.1029/2009JC006020
- Eicken H, Reimnitz E, Alexandrov V, Martin T, Kassens H, Viehoff T (1997) Sea-ice processes in the Laptev Sea and their importance for sediment export. *Continental Shelf Research* 17(2):205–233
- Eicken H, Dmitrenko I, Tyshko K, Darovskikh A, Dierking W, Blahak U, Groves J, Kassens H (2005) Zonation of the Laptev Sea landfast ice cover and its importance in a frozen estuary. *Global and planetary change* 48(1-3):55–83
- Eldevik T, Straneo F, Sand AB, Furevik T (2005) Pathways and Export of Greenland Sea Water, American Geophysical Union, pp 89–103. DOI 10.1029/158GM08
- Ezraty R, Ardhuin F, Croizé-Fillon D (2006) Sea ice drift in the Central Arctic using the 89 GHz brightness temperatures of the Advanced Microwave Scanning Radiometer (AMSR-E). *User's Manual, Version 2* p 21
- Fieg K, Gerdes R, Fahrbach E, Beszczynska-Möller A, Schauer U (2010) Simulation of oceanic volume transports through Fram Strait 1995-2004. *Ocean Dynamics* 60(3):491–502

- Fisher N (1996) Statistical analysis of circular data. Cambridge University Press
- Fofonova V, Androsov A, Danilov S, Janout M, Sofina E, Wiltshire K (2014) Semidiurnal tides in the laptev sea shelf zone in the summer season. *Continental Shelf Research* 73(0):119 – 132, DOI <http://dx.doi.org/10.1016/j.csr.2013.11.010>
- Fowler C, W E, M T (2013) Polar pathfinder daily 25 km ease-grid sea ice motion vectors. version 2. (monthly mean gridded field)
- Frolov I, Ashik I, Kassens H, Polyakov I, Proshutinsky A, Sokolov V, Timokhov L (2009) Anomalous variations in the thermohaline structure of the Arctic Ocean. In: *Doklady Earth Sciences*, Springer, vol 429-2, pp 1567–1569
- Gerdes R, Köberle C (1995) On the influence of DSOW in a numerical model of the North Atlantic general circulation. *Journal of Physical Oceanography* 25:2624–2642, DOI [doi:10.1175/1520-0485\(1995\)025<2624:OTIODI>2.0.CO;2](https://doi.org/10.1175/1520-0485(1995)025<2624:OTIODI>2.0.CO;2)
- Gerdes R, Karcher M, Kauker F, Schauer U (2003) Causes and development of repeated Arctic Ocean warming events. *Geophysical Research Letters* 30(19):doi:10.1029/2003GL018,080
- Girard-Ardhuin F, Ezraty R (2005) Validation of Arctic sea ice drift with IABP buoys p 7, URL <http://www.ifremer.fr/docelec/doc/2005/acte-1292.pdf>
- Girard-Ardhuin F, Ezraty R (2012) Enhanced Arctic sea ice drift estimation merging radiometer and scatterometer data. *IEEE Transactions on Geoscience and Remote Sensing* 50(7):2639–2648
- Govorucha L, Gerasimov I (eds) (1970) *Sovetskaja Arktika - Morja i ostrova Severnogo Ledovitogo okeana* (Soviet Arctic - Seas and islands of the Arctic Ocean). Nauka, Moscow
- Haas C, Pfaffling A, Hendricks S, Rabenstein L, Etienne J, Rigor I (2008) Reduced ice thickness in Arctic Transpolar Drift favors rapid ice retreat. *Geophysical Research Letters* 35(17):1–L17,501
- Harder M, Lemke P, Hilmer M (1998) Simulation of sea ice transport through Fram Strait: Natural variability and sensitivity to forcing. *Journal of Geophysical Research* 103(C3):5595–5606

- Harms IH, Schrum C, Hatten K (2005) Numerical sensitivity studies on the variability of climate-relevant processes in the Barents Sea. *Journal of Geophysical Research: Oceans* 110(C6), DOI 10.1029/2004JC002559, URL <http://dx.doi.org/10.1029/2004JC002559>
- Hibler W (1979) A dynamic thermodynamic sea ice model. *Journal of Physical Oceanography* 9(4):815–846
- Hibler WD, Bryan K (1987) A diagnostic ice ocean model. *Journal of Physical Oceanography* 17:987–1015
- Hibler WD, Walsh JE (1982) On Modeling Seasonal and Interannual Fluctuations of Arctic Sea Ice. *Journal of Physical Oceanography* 12:1514–1523, DOI 10.1175/1520-0485(1982)012<1514:OMSAIF>2.0.CO;2
- Hölemann J, Kirillov S, Klagge T, Novikhin A, Kassens H, Timokhov L (2011) Near-bottom water warming in the Laptev Sea in response to atmospheric and sea ice conditions in 2007. *Polar Research* 30(0)
- Hughes SL, Holliday NP (2006) ICES report on ocean climate 2005. ICES
- Hunke E, Dukowicz JK (1997) An elastic-viscous-plastic model for sea ice dynamics. *Journal of Physical Oceanography* 27:1849–1867, DOI doi:10.1175/1520-0485(1997)027<1849:AEVPMF>2.0.CO;2
- Hunke EC, Holland MM (2007) Global atmospheric forcing data for Arctic ice-ocean modeling. *Journal of Geophysical Research: Oceans* 112(C4), DOI 10.1029/2006JC003640
- Instruments R (1996) Acoustic doppler current profilers principles of operation: A practical primer. RD Instruments
- Itkin P, Karcher M, R G (2013) Is weaker Arctic sea ice changing the Atlantic water circulation? *Journal of Geophysical Research* submitted
- Ivanov V, Alexeev V, Repina I, Koldunov N, Smirnov A (2012) Tracing Atlantic Water Signature in the Arctic Sea Ice Cover East of Svalbard. *Advances in Meteorology* 2012, DOI 10.1155/2012/201818, URL <http://dx.doi.org/10.1155/2012/201818>
- Jakobsson M, Macnab R, Mayer L, Anderson R, Edwards M, Hatzky J, Schenke H, Johnson P (2008) An improved bathymetric portrayal of the Arctic Ocean: Implications for ocean modeling and geological, geophysical and oceanographic analyses. *Geophysical Research Letters* 35(7):doi:10.1029/2008GL033,520

- Jammalamadaka S, Sengupta A (2001) Topics in circular statistics. World Scientific Publishing, London
- Johnson M, Polyakov I (2001) The Laptev Sea as a source for recent Arctic Ocean salinity changes. *Geophys Res Lett* 28(10):2017–2020
- Johnson M, Proshutinsky A, Polyakov I (1999) Atmospheric patterns forcing two regimes of arctic circulation: A return to anticyclonic conditions? *Geophysical Research Letters* 26(11):1621–1624
- Johnson M, Proshutinsky A, Aksenov Y, Nguyen AT, Lindsay R, Haas C, Zhang J, Diansky N, Kwok R, Maslowski W, Haekkinen S, Ashik I, de Cuevas B (2012) Evaluation of Arctic sea ice thickness simulated by Arctic Ocean Model Intercomparison Project models. *JOURNAL OF GEOPHYSICAL RESEARCH-OCEANS* 117, DOI {10.1029/2011JC007257}
- Juricke S, Lemke P, Timmermann R, Rackow T (2013) Effects of stochastic ice strength perturbation on Arctic finite element sea ice modeling. *Journal of Climate* 26(11):3785–3802, DOI 10.1175/JCLI-D-12-00388.1
- Kanamitsu M, Ebisuzaki W, Woollen J, Yang S, Hnilo J, Fiorino M, Potter G (2002) NCEP–DOE AMIP-II Reanalysis (R-2). *Bulletin of the American Meteorological Society* 83(11):1631–1643
- Karcher M, Gerdes R, Kauker F, Köberle C (2003) Arctic warming: Evolution and spreading of the 1990s warm event in the Nordic seas and the Arctic Ocean. *Journal of Geophysical Research* 108(C2):doi:10.1029/2001JC001,265
- Karcher M, Beszczynska-Mller A, Kauker F, Gerdes R, Heyen S, Rudels B, Schauer U (2011) Arctic Ocean warming and its consequences for the Denmark Strait overflow. *Journal of Geophysical Research: Oceans* 116(C2), DOI 10.1029/2010JC006265
- Karcher M, Smith JN, Kauker F, Gerdes R, Smethie WM (2012) Recent changes in Arctic Ocean circulation revealed by iodine-129 observations and modeling. *Journal of Geophysical Research* 117(C8):C08,007+, DOI 10.1029/2011jc007513, URL <http://dx.doi.org/10.1029/2011jc007513>
- Kattsov VM, Walsh JE (2000) Twentieth-Century Trends of Arctic Precipitation from Observational Data and a Climate Model Simulation. *Journal of Climate* 13:1362–1370

- Kattsov VM, Ryabinin VE, Overland JE, Serreze MC, Visbeck M, Walsh JE, Meier W, Zhang X (2010) Arctic sea-ice change: a grand challenge of climate science. *Journal of Glaciology* 56(200):1115–1121, DOI doi:10.3189/002214311796406176, URL <http://www.ingentaconnect.com/content/igsoc/jog/2010/00000056/00000200/art00016>
- Kauker F, Kaminski T, Karcher M, Giering R, Gerdes R, Vobeck M (2009) Adjoint analysis of the 2007 all time arctic sea-ice minimum. *Geophysical Research Letters* 36(3), DOI 10.1029/2008GL036323
- König Beatty C, Holland DM (2010) Modeling landfast sea ice by adding tensile strength. *Journal of Physical Oceanography* 40(1):185–198
- Kreyscher M, Harder M, Lemke P, Flato G (2000a) Results of the Sea Ice Model Intercomparison Project: Evaluation of sea ice rheology schemes for use in climate simulations. *Journal of Geophysical Research-Oceans* 105(C5):11,299–11,320
- Kreyscher M, Harder M, Lemke P, Flato GM (2000b) Results of the Sea Ice Model Intercomparison Project: Evaluation of sea ice rheology schemes for use in climate simulations. *Journal of Geophysical Research: Oceans* (1978–2012) 105(C5):11,299–11,320
- Kruppen T, Hölemann J, Willmes S, Maqueda M, Busche T, Dmitrenko I, Gerdes R, Haas C, Heinemann G, Hendricks S, et al (2011) Sea ice production and water mass modification in the eastern laptev sea. *Journal of Geophysical Research* 116(C5):C05,014
- Kwok R, Cunningham GF (2008) ICESat over Arctic sea ice: Estimation of snow depth and ice thickness. *Journal of Geophysical Research: Oceans* 113(C8), DOI 10.1029/2008JC004753
- Kwok R, Rothrock D (2009) Decline in Arctic sea ice thickness from submarine and ICESat records: 1958-2008. *Geophysical Research Letters* 36(15)
- Kwok R, Schweiger A, Rothrock D, Pang S, Kottmeier C (1998) Sea ice motion from satellite passive microwave imagery assessed with ERS SAR and buoy motions. *Journal of Geophysical Research* 103(C4):8191–8214
- Kwok R, Cunningham G, Wensnahan M, Rigor I, Zwally H, Yi D (2009) Thinning and volume loss of the Arctic Ocean sea ice cover: 2003-2008. *Journal of Geophysical Research* 114(C7):C07,005

- Large W, Yeager S (2009) The global climatology of an interannually varying air-sea flux data set. *Climate Dynamics* 33(2-3):341–364, DOI 10.1007/s00382-008-0441-3
- Large WG, McWilliams JC, Doney SC (1994) Oceanic vertical mixing: A review and a model with a nonlocal boundary layer parameterization. *Reviews of Geophysics* 32(4):363–403, DOI 10.1029/94RG01872
- Lavergne T, Eastwood S, Teffah Z, Schyberg H, Breivik LA (2010) Sea ice motion from low-resolution satellite sensors: An alternative method and its validation in the Arctic. *Journal of Geophysical Research: Oceans* 115(C10), DOI 10.1029/2009JC005958
- Lemke P, Hibler W, Flato G, Harder M, Kreyscher M (1997) On the improvement of sea-ice models for climate simulations: the Sea Ice Model Intercomparison Project. *Annals of Glaciology* 25:183–187
- Lieser J (2004) A numerical model for short-term sea ice forecasting in the Arctic= Ein numerisches Modell zur Meereisvorhersage in der Arktis. *Berichte zur Polar-und Meeresforschung= Reports on polar and marine research* 485:93
- Lindsay R, Wensnahan M, Schweiger A, Zhang J (2014) Evaluation of seven different atmospheric reanalysis products in the Arctic. *Journal of Climate* 27(2-3):2588–2606, DOI 10.1175/JCLI-D-13-00014.1
- Losch M, Menemenlis D, Campin JM, Heimbach P, Hill C (2010) On the formulation of sea-ice models. part 1: Effects of different solver implementations and parameterizations. *Ocean Modelling* 33(1):129–144
- Mahoney A, Eicken H, Gaylord A, Shapiro L (2007) Alaska landfast sea ice: Links with bathymetry and atmospheric circulation. *J Geophys Res* 112:C02,001
- Marshall J, Adcroft A, Hill C, Perelman L, Heisey C (1997) A finite-volume, incompressible Navier Stokes model for studies of the ocean on parallel computers. *J geophys Res* 102(C3):5753–5766
- Martin S, Cavalieri D (1989) Contributions of the Siberian Shelf Polynyas to the Arctic Ocean intermediate and deep water. *Journal of Geophysical Research* 94(C9)

- Martin T, Gerdes R (2007) Sea ice drift variability in Arctic Ocean Model Intercomparison Project models and observations. *Journal of Geophysical Research* 112(C04S10):doi:10.1029/2006JC003,617
- McClelland J, Holmes R, Peterson B, Stieglitz M (2004) Increasing river discharge in the Eurasian Arctic: Consideration of dams, permafrost thaw, and fires as potential agents of change. *Journal of geophysical research* 109(D18):D18,102
- McGeehan T, Maslowski W (2012) Evaluation and control mechanisms of volume and freshwater export through the Canadian Arctic Archipelago in a high-resolution pan-Arctic ice-ocean model. *Journal of Geophysical Research: Oceans* 117(C8), DOI 10.1029/2011JC007261, URL <http://dx.doi.org/10.1029/2011JC007261>
- Meier W, Maslanik J, Fowler C (2000) Error analysis and assimilation of remotely sensed ice motion within an Arctic sea ice model. *Journal of Geophysical Research-Oceans* 105(C2):3339–3356
- MITgcm Group (2014a) MITgcm User Manual. Online documentation, MIT/EAPS, Cambridge, MA 02139, USA, URL http://mitgcm.org/public/r2_manual/latest/online_documents
- MITgcm Group (2014b) MITgcm User Manual. Online documentation, MIT/EAPS, Cambridge, MA 02139, USA, http://mitgcm.org/public/r2_manual/latest/online_documents
- Münchow A, Weingartner T, Cooper L (1999) The Summer Hydrography and Surface Circulation of the East Siberian Shelf Sea. *Journal of Physical Oceanography* 29:2167–2182
- Nguyen AT, Menemenlis D, Kwok R (2012) Source and pathway of the Western Arctic upper halocline in a data-constrained coupled ocean and sea ice model. *Journal of Physical Oceanography* 42:802–823, DOI 10.1175/JPO-D-11-040.1
- Nguyen AT, Menemenlis D, Kwok R (2009) Improved modeling of the Arctic halocline with a subgrid-scale brine rejection parameterization. *JOURNAL OF GEOPHYSICAL RESEARCH-OCEANS* 114, DOI {10.1029/2008JC005121}
- Olason EÖ (2012) Dynamical modelling of kara sea land-fast ice. PhD thesis, University of Hamburg

- OSI-SAF (2013) EUMETSAT Ocean and Sea Ice Satellite Application Facility. Global sea ice concentration reprocessing dataset 1978-2009 (v1.1, 2011). URL <http://osisaf.met.no>
- Overland J, Wang M (2005) The Arctic climate paradox: The recent decrease of the Arctic Oscillation. *Geophysical Research Letters* 32(6)
- Overland J, Wang M (2010) Large-scale atmospheric circulation changes are associated with the recent loss of Arctic sea ice. *Tellus A* 62(1):1–9
- Pacanowski R (1995) MOM 2 documentation, users guide and reference manual. GFDL Ocean Group Tech Rep 3:232
- Perovich DK, Richter-Menge JA, Jones KF, Light B (2008) Sunlight, water, and ice: Extreme Arctic sea ice melt during the summer of 2007. *Geophysical Research Letters* 35(11), DOI 10.1029/2008GL034007, URL <http://dx.doi.org/10.1029/2008GL034007>
- Peterson B, Holmes R, McClelland J, Vorosmarty C, Lammers R, Shiklomanov A, Shiklomanov I, Rahmstorf S (2002) Increasing river discharge to the Arctic Ocean. *Science* 298(5601):2171
- Polyakov I, Beszczynska A, Carmack E, Dmitreko I, Fahrbach E, Frolov I, Gerdes R, Hansen E, Holfort J, Ivanov V, et al (2005a) One more step toward a warmer Arctic. *Geophysical Research Letters* 32:L17,605
- Polyakov I, Timokhov L, Alexeev V, Bacon S, Dmitrenko I, Fortier L, Frolov I, Gascard JC, Hansen E, Ivanov V, Laxon S, Mauritzen C, Perovich D, K S, H S, Sokolov V, Steele M, Toole J (2010) Arctic ocean warming contributes to reduced polar ice cap. *Journal of Physical Oceanography* 40:2743–2756, DOI 10.1175/2010JPO4339.1
- Polyakov IV, Beszczynska A, Carmack EC, Dmitrenko IA, Fahrbach E, Frolov IE, Gerdes R, Hansen E, Holfort J, Ivanov VV, Johnson MA, Karcher M, Kauker F, Morison J, Orvik KA, Schauer U, Simmons HL, Skagseth, Sokolov VT, Steele M, Timokhov LA, Walsh D, Walsh JE (2005b) One more step toward a warmer Arctic. *Geophysical Research Letters* 32(17), DOI 10.1029/2005GL023740
- Prange M (2003) Einfluss arktischer süßwasserquellen auf die zirkulation im nordmeer und im nordatlantik in einem prognostischen ozean-meereis-modell= influence of arctic freshwater sources on the circulation in the arctic mediterranean and the north atlantic in a prognostic ocean-sea ice model.

- Berichte zur Polar-und Meeresforschung (Reports on Polar and Marine Research) 468
- Prange M, Gerdes R (2006) The role of surface freshwater flux boundary conditions in Arctic Ocean modelling. *Ocean modelling* 13(1):25–43
- Proshutinsky A, Johnson M (1997) Two circulation regimes of the wind-driven Arctic Ocean. *Journal of Geophysical Research* 102(C6):12,493
- Proshutinsky A, Ashik I, Häkkinen S, Hunke E, Krishfield R, Maltrud M, Maslowski W, Zhang J (2007) Sea level variability in the Arctic Ocean from AOMIP models. *Journal of Geophysical Research* 112(C4):C04S08
- Rabe B, Karcher M, Schauer U, Toole JM, Krishfield RA, Pisarev S, Kauker F, Gerdes R, Kikuchi T (2011) An assessment of Arctic Ocean freshwater content changes from the 1990s to the 2006-2008 period. *Deep Sea Research Part I: Oceanographic Research Papers* 58(2):173 – 185, DOI <http://dx.doi.org/10.1016/j.dsr.2010.12.002>
- Rabenstein L, Krumpen T, Hendricks S, Köberle C, Haas C, Hölemann JA (2013) A combined approach of remote sensing and airborne electromagnetics to determine the volume of polynya sea ice in the Laptev Sea (vol 7, pg 947, 2013). *CRYOSPHERE* 7(4):1107–1108, DOI {10.5194/tc-7-1107-2013}
- Rampal P, Weiss J, Marsan D (2009) Positive trend in the mean speed and deformation rate of Arctic sea ice, 1979-2007. *Journal of Geophysical Research: Oceans* 114(C5), DOI 10.1029/2008JC005066, URL <http://dx.doi.org/10.1029/2008JC005066>
- Reimnitz E, Dethleff D, Nurnberg D (1994) Contrasts IN Arctic shelf sea-ice regimes and some implications - Beaufort Sea versus Laptev Sea. *Marine Geology* 119(3-4):215–225, DOI 10.1016/0025-3227(94)90182-1, 4th International Conference on Paleooceanography (ICP IV), KIEL, Germany, Sep. 21-25, 1992
- Rigor I, Colony R (1997) Sea-ice production and transport of pollutants in the Laptev Sea, 1979–1993. *Science of the Total Environment*, The 202(1-3):89–110
- Rigor I, Wallace J, Colony R (2002) Response of sea ice to the Arctic Oscillation. *Journal of Climate* 15:2648–2663
- Rinke A, Dethloff K, Dorn W, Handorf D, Moore JC (2013) Simulated Arctic atmospheric feedbacks associated with late summer sea ice anomalies.

- Journal of Geophysical Research: Atmospheres 118(14):7698–7714, DOI 10.1002/jgrd.50584, URL <http://dx.doi.org/10.1002/jgrd.50584>
- Rollenhagen K, Timmermann R, Janjic T, Schröter J, Danilov S (2009) Assimilation of sea ice motion in a finite-element sea ice model. *Journal of Geophysical Research* 114(C05007):doi:10.1029/2008JC005,067
- Romanov I (2004) Morphometric Characteristics of Ice and Snow in the Arctic Basin: Aircraft Landing Observations from the Former Soviet Union, 1928-1989. National Snow and Ice Data Center, Boulder, CO, digital media [Available online at <http://nsidc.org/data/g02140.html>]
- Rosich B, Meadows P (2004) Absolute calibration of ASAR level 1 products generated with PF-ASAR. ESA Document, Frascati, Italy
- Rothrock D (1975) The mechanical behavior of pack ice. *Annual Review of Earth and Planetary Sciences* 3(1):317–342
- Rozman P (2009) The Role of the Fast Ice in an Arctic Sea Ice - Ocean Coupled Model. Master's thesis, Bremen University, Bremen, Germany
- Rozman P, Hölemann J, Krumpfen T, Gerdes R, Köberle C, Lavergne T, Adams S, Girard-Ardhuin F (2011) Validating satellite derived and modelled sea-ice drift in the Laptev sea with in situ measurements from the winter of 2007/08. *Polar Research* 30(0)
- Rudels B, Jones EP, Anderson LG, Kattner G (1994) On the Intermediate Depth Waters of the Arctic Ocean, American Geophysical Union, pp 33–46. DOI 10.1029/GM085p0033
- Rudels B, Anderson L, Jones E (1996) Formation and evolution of the surface mixed layer and halocline of the Arctic Ocean. *Journal of Geophysical Research* 101(C4):8807–8821
- Rudels B, Jones EP, Schauer U, Eriksson P (2004) Atlantic sources of the arctic ocean surface and halocline waters. *Polar Research* 23(2):181–208, DOI 10.1111/j.1751-8369.2004.tb00007.x, URL <http://dx.doi.org/10.1111/j.1751-8369.2004.tb00007.x>
- Saha S, Moorthi S, Pan HL, Wu X, Wang J, Nadiga S, Tripp P, Kistler R, Woollen J, Behringer D, Liu H, Stokes D, Grumbine R, Gayno G, Wang J, Hou YT, Chuang HY, Juang HMH, Sela J, Iredell M, Treadon R, Kleist D, Van Delst P, Keyser D, Derber J, Ek M, Meng J, Wei H, Yang R, Lord S,

- Van den Dool H, Kumar A, Wang W, Long C, Chelliah M, Xue Y, Huang B, Schemm JK, Ebisuzaki W, Lin R, Xie P, Chen M, Zhou S, Higgins W, Zou CZ, Liu Q, Chen Y, Han Y, Cucurull L, Reynolds RW, Rutledge G, Goldberg M (2010) The ncep climate forecast system reanalysis. *BULLETIN OF THE AMERICAN METEOROLOGICAL SOCIETY* 91(8):1015–1057, DOI {10.1175/2010BAMS3001.1}
- Schauer U, Fahrbach E, Osterhus S, Rohardt G (2004) Arctic warming through the Fram Strait: Oceanic heat transport from 3 years of measurements. *Journal of geophysical research* 109(C6):C06,026
- Schauer U, Beszczynska-Möller A, Walczowski W, Fahrbach E, Piechura J, Hansen E (2008) Variation of measured heat flow through the fram strait between 1997 and 2006. In: Dickson RR, Meincke J, Rhines P (eds) *Arctic-Subarctic Ocean Fluxes*, Springer Netherlands, pp 65–85, DOI 10.1007/978-1-4020-6774-7_4
- Schmitz WJ, McCartney MS (1993) On the North Atlantic Circulation. *Reviews of Geophysics* 31(1):29–49, DOI 10.1029/92RG02583
- Schweiger A, Lindsay R, Zhang J, Steele M, Stern H, Kwok R (2011) Uncertainty in modeled arctic sea ice volume. *Journal of Geophysical Research: Oceans* 116(C8), DOI 10.1029/2011JC007084
- Shimada K, Kamoshida T, Itoh M, Nishino S, Carmack E, McLaughlin F, Zimmermann S, Proshutinsky A (2006) Pacific Ocean inflow: Influence on catastrophic reduction of sea ice cover in the Arctic Ocean. *Geophysical Research Letters* 33(8), DOI 10.1029/2005GL025624, URL <http://dx.doi.org/10.1029/2005GL025624>
- Smith JN, Ellis KM, Boyd T (1999) Circulation features in the central Arctic Ocean revealed by nuclear fuel reprocessing tracers from Scientific Ice Expeditions 1995 and 1996. *Journal of Geophysical Research: Oceans* 104(C12):29,663–29,677, DOI 10.1029/1999JC900244, URL <http://dx.doi.org/10.1029/1999JC900244>
- Smolyanitsky V, Borodachev V, Mahoney A, Fetterer F, Barry R (2007) Sea ice charts of the Russian Arctic in gridded format, 1933-2006. Colorado USA: National Snow and Ice Data Center DOI 10.7265/N5D21VHJ
- Spreen G, Kwok R, Menemenlis D (2011) Trends in Arctic sea ice drift and role of wind forcing: 1992-2009. *Geophysical Research Letters* 38(19), DOI 10.1029/2011GL048970, URL <http://dx.doi.org/10.1029/2011GL048970>

- Steele M, Boyd T (1998) Retreat of the cold halocline layer in the Arctic Ocean. *Journal of Geophysical Research* 103(C5):10,419
- Steele M, Morley R, Ermold W (2001) Phc: A global ocean hydrography with a high-quality arctic ocean. *Journal of Climate* 14:2079–2087, DOI 10.1175/1520-0442(2001)014<2079:PAGOHW>2.0.CO;2
- Steele M, Ermold W, Zhang J (2008) Arctic Ocean surface warming trends over the past 100 years. *Geophysical Research Letters* 35(2), DOI 10.1029/2007GL031651, URL <http://dx.doi.org/10.1029/2007GL031651>
- Stevens D (1991) The open boundary condition in the United Kingdom fine-resolution Antarctic model. *Journal of Physical Oceanography* 21(9):1494–1499
- Stevens DP (1990) On open boundary conditions for three dimensional primitive equation ocean circulation models. *Geophysical & Astrophysical Fluid Dynamics* 51(1-4):103–133
- Stroeve JC, Kattsov V, Barrett A, Serreze M, Pavlova T, Holland M, Meier WN (2012) Trends in arctic sea ice extent from cmip5, cmip3 and observations. *Geophysical Research Letters* 39(16), DOI 10.1029/2012GL052676
- Sumata H, Kauker F, Gerdes R, Koeberle C, Karcher M (2013) A comparison between gradient descent and stochastic approaches for parameter optimization of a sea ice model. *Ocean Science* 9(4):609–630, DOI 10.5194/os-9-609-2013
- Swift J, Jones E, Aagaard K, Carmack E, Hingston M, MacDonald R, McLaughlin F, Perkin R (1997) Waters of the makarov and canada basins. *Deep Sea Research Part II: Topical Studies in Oceanography* 44(8):1503 – 1529, DOI 10.1016/S0967-0645(97)00055-6
- Swift JH (1984) The circulation of the Denmark Strait and Iceland-Scotland overflow waters in the North Atlantic. *Deep Sea Research Part A Oceanographic Research Papers* 31(11):1339 – 1355, DOI [http://dx.doi.org/10.1016/0198-0149\(84\)90005-0](http://dx.doi.org/10.1016/0198-0149(84)90005-0), URL <http://www.sciencedirect.com/science/article/pii/0198014984900050>
- Thompson D, Wallace J (1998) The Arctic Oscillation signature in the wintertime geopotential height and temperature fields. *Geophysical Research Letters* 25(9):1297–1300

- Thorndike A, Colony R (1982) Sea ice motion in response to geostrophic winds. *Journal of Geophysical Research* 87(C8):5845–5852
- Timco G, O’Brien S (1994) Flexural strength equation for sea ice. *Cold Regions Science and Technology* 22(3):285–298
- Timco G, Weeks W (2010) A review of the engineering properties of sea ice. *Cold Regions Science and Technology* 60(2):107–129
- Timokhov L, Tanis F (1997) Environmental Working Group Joint US–Russian Atlas of the Arctic Ocean-Winter Period. Environmental Research Institute of Michigan in association with the National Snow and Ice Data Center, Arctic Climatology Project, CD-ROM
- Timokhov L, Tanis F (1998) Environmental Working Group Joint US–Russian Atlas of the Arctic Ocean-Summer Period. Environmental Research Institute of Michigan in association with the National Snow and Ice Data Center, Arctic Climatology Project, CD-ROM
- Tremblay LB, Hakakian M (2006) Estimating the sea ice compressive strength from satellite-derived sea ice drift and ncep reanalysis data. *Journal of Physical Oceanography* 36:2165–2172, DOI 10.1175/JPO2954.1
- Von Storch H, Zwiers FW (2001) *Statistical analysis in climate research*. Cambridge university press
- Weingartner T, Danielson S, Sasaki Y, Pavlov V, Kulakov M (1999) The Siberian Coastal Current: A wind-and buoyancy-forced Arctic coastal current. *Journal of geophysical research* 104(C12):29,697
- Weiss J (2013) Sea ice fracturing. In: *Drift, Deformation, and Fracture of Sea Ice*, Springer Briefs in Earth Sciences, Springer Netherlands, pp 53–72, DOI 10.1007/978-94-007-6202-2-4
- Wilks DS (1995) *Statistical methods in the atmospheric sciences*, vol 100. Academic press
- Willmes S, Adams S, Schroeder D, Heinemann G (2011) Spatio-temporal variability of polynya dynamics and ice production in the Laptev Sea between the winters of 1979/80 and 2007/08. *POLAR RESEARCH* 30, DOI {10.3402/polar.v30i0.5971}
- Winsor P, Björk G (2000) Polynya activity in the Arctic Ocean from 1958 to 1997. *Journal of Geophysical Research-Oceans* 105(C4)

- Wu B, Wang J, Walsh JE (2006) Dipole Anomaly in the Winter Arctic Atmosphere and Its Association with Sea Ice Motion. *Journal of Climate* 19:210–225, DOI doi:10.1175/JCLI3619.1, URL <http://dx.doi.org/10.1175/JCLI3619.1>
- Yang J (2009) Seasonal and interannual variability of downwelling in the Beaufort Sea. *Journal of Geophysical Research: Oceans* 114(C1), DOI 10.1029/2008JC005084, URL <http://dx.doi.org/10.1029/2008JC005084>
- Yu Y, Stern H, Fowler C, Fetterer F, Maslanik J (2014) Interannual variability of Arctic landfast ice between 1976 and 2007. *Journal of Climate* 27:227–243, DOI {10.1175/JCLI-D-13-00178.1}
- Zhang J, Hibler WD (1997) On an efficient numerical method for modeling sea ice dynamics. *Journal of Geophysical Research: Oceans* 102(C4):8691–8702, DOI 10.1029/96JC03744, URL <http://dx.doi.org/10.1029/96JC03744>
- Zhang J, Hibler III W (1997) On an efficient numerical method for modeling sea ice dynamics. *Journal of Geophysical Research C Oceans* 102:8691–8702
- Zhang J, Lindsay R, Schweiger A, Rigor I (2012) Recent changes in the dynamic properties of declining arctic sea ice: A model study. *Geophysical Research Letters* 39(20), DOI 10.1029/2012GL053545
- Zhang X, Sorteberg A, Zhang J, Gerdes R, Comiso J (2008) Recent radical shifts of atmospheric circulations and rapid changes in Arctic climate system. *Geophysical Research Letters* 35(22):L22,701
- Zwally H, Schutz B, Abdalati W, Abshire J, Bentley C, Brenner A, Bufton J, Dezio J, Hancock D, Harding D, Herring T, Minster B, Quinn K, Palm S, Spinhirne J, Thomas R (2002) Icesat’s laser measurements of polar ice, atmosphere, ocean, and land. *Journal of Geodynamics* 34(3-4):405 – 445, DOI [http://dx.doi.org/10.1016/S0264-3707\(02\)00042-X](http://dx.doi.org/10.1016/S0264-3707(02)00042-X)

Acknowledgements

I would like to express my gratitude towards my supervisor Prof. Rüdiger Gerdes, AWI. Ruediger has been a great supervisor. He managed to guide me in my research and yet left me a lot of scientific freedom. His door has always been open and he always had 'a couple of minutes' for me.

I am grateful to Prof. Laurenz Thomsen, Jacobs University who agreed to be my second referee.

Martin Losch, AWI, my referee as an external member has been of a great help to me with the MITgcm. His friendly, detailed and on-spot explanations of the model code and physics have been not only helpful but very inspiring.

Michael Karcher, AWI and O.A.Sys - Ocean Atmosphere Systems, has acted as my advisor during the last year of my graduate studies. His good mood and relaxed communication have encouraged me through the hardest moments.

Cornelia Köberle supervised and supported my first steps into the numerical modeling and coding. She kindly showed me around the NAOSIM code.

Prof. Ursula Schauer, AWI, Jens Hölemann, AWI and IFM-GEOMAR and Frank Kauker, AWI and O.A.Sys - Ocean Atmosphere Systems have together with Ruediger, Martin, Michael and Cornelia attended my regular POLMAR PhD Panel Meetings and guided my scientific work.

I am very grateful to Claudia Hanfland and Claudia Sprengel from the POLMAR graduate school at AWI. Both have not only organized appealing courses, but advised me and helped with many technical and personal issues.

I would like to thank Marcel Nicolaus, AWI and Chris Petrich, Norut Narvik - Nothern Research Institute Narvik, Norway (at that time International Arctic Research Center, Fairbanks, Alaska) who made possible my only hands-on sea ice experience during the SIZONet field campaign in May 2010, Barrow, Alaska.

Furthermore i would like to thank everybody at AWI who is encouraging the life-work balance guideline of the institute. Winfried Hebold-Heitz, Ursula Schauer (also former AWI women's representative), Beate Meinardus and Andrea Bleyer have all been very supportive whenever I encountered difficulties.

I am grateful for the opportunity to work along with Priska Hunkeler, Thomas Krumpfen, Valeria Selyuzhenok, Stefan Hendricks, Lasse Rabenstein, Vera Fononova, Robert Ricker, Giulia Castellani, Karel Castro-Morales, Kathrin Riemann-Campe, Hiroshi Sumata, Frank Kauker, Malte Thoma, Hartmut Hellmer, Verena Haid, Ralph Timmermann, Jürgen Determann, Wee Cheah and many other present and former AWI colleagues from the Sea ice physics group and from the Climate Sciences division who helped to create a relaxed and productive working environment.

My graduate studies have been partially supported by a grant of Municipality of Ljubljana, Slovenia.

Finally, I would like to thank my family for their unfailing love, patience and support.